Charge-Storage Mechanisms in Polymer Electrets

Dissertation

presented by:

FRANCISCO CAMACHO GONZÁLEZ

born on August the 12th 1972 in Mexico City

in partial fulfilment of the
requirements of the degree of

Doctor of Natural Sciences
(Dr. rer. nat.)
in
Physics

Submitted to the

Faculty of Mathematics and Natural Sciences
of the
University of Potsdam

March 2006

Camacho González,
Francisco

student matric. no. 705285

I, **Francisco Camacho González**, formally submit my thesis

"Charge-Storage Mechanisms in Polymer Electrets"

in fulfilment of the requirements set forth by the Regulations for awarding the title "doctor rerum naturalium" (Dr. rer. nat.) and Doctor of Engineering (Dr. Ing.) in the Mathematics-Natural Science Faculty of the University of Potsdam.

I hereby certify that the work presented in this thesis has not been submitted to any other university/higher education institute and is original and has been based on the research I performed during my stance in the University of Potsdam and by using only the means and source material as noted therein.

Signed,

Acknowledgements

Abstract

In view of the importance of charge storage in polymer electrets for electromechanical-transducer applications, the aim of this work is to contribute to the understanding of the charge-retention mechanisms. Furthermore, we will try to explain how the long-term storage of charge carriers in polymeric electrets works and to identify the probable trap sites. Charge trapping and de-trapping processes were investigated in order to obtain evidence of the trap sites in polymeric electrets. The charge de-trapping behavior of two particular polymer electrets was studied by means of thermal and optical techniques. In order to obtain evidence of trapping or de-trapping, charge and dipole profiles in the thickness direction were also monitored.

In this work, the study was performed on polyethylene terephthalate (PETP) and on cyclic olefin copolymers (COCs). PETP is a photo-electret and contains a net dipole moment that is located in the carbonyl group ($>$C $=$ O). The electret behavior of PETP arises from both the dipole orientation and the charge storage. In contrast to PETP, COCs are not photo-electrets and do not exhibit a net dipole moment. The electret behavior of COCs arises from the storage of charges only.

COC samples were doped with dyes in order to probe their internal electric field. COCs show shallow charge traps at 0.6 and 0.11 eV, characteristic for thermally activated processes. In addition, deep charge traps are present at 4 eV, characteristic for optically stimulated processes.

PETP films exhibit a photo-current transient with a maximum that depends on the temperature with an activation energy of 0.106 eV. The pair thermalization length (r_c) calculated from this activation energy for the photo-carrier generation in PETP was estimated to be approx. 4.5 nm. The generated photo-charge carriers can recombine, interact with the trapped charge, escape through the electrodes or occupy an empty trap.

PETP possesses a small quasi-static pyroelectric coefficient (QPC): ~0.6 nC/(m^{2}K) for unpoled samples, ~60 nC/(m^{2}K) for poled samples and ~60 nC/(m^{2}K) for unpoled samples under an electric bias ($E \approx$ 10 V/µm). When stored charges generate an internal electric field of approx. 10 V/µm, they are able to induce a QPC comparable to that of the oriented dipoles. Moreover, we observe charge-dipole interaction. Since the raw data of the QPC-experiments on PETP samples is noisy, a numerical Fourier-filtering procedure was applied. Simulations show that the data analysis is reliable when the noise level is up to 3 times larger than the calculated pyroelectric current for the QPC.

PETP films revealed shallow traps at approx. 0.36 eV during thermally-stimulated current measurements. These energy traps are associated with molecular dipole relaxations ($>$C $=$ O). On the other hand, photo-activated measurements yield deep charge traps at 4.1 and 5.2 eV. The observed wavelengths belong to the transitions in PETP that are analogous to the $\pi - \pi^*$ benzene transitions. The observed charge de-trapping selectivity in the

photocharge decay indicates that the charge detrapping is from a direct photon-charge interaction. Additionally, the charge de-trapping can be facilitated by photo-exciton generation and the interaction of the photo-excitons with trapped charge carriers. These results indicate that the benzene rings ($-C_6H_4-$) and the dipolar groups ($>C = O$) can stabilize and share an extra charge carrier in a chemical resonance. In this way, this charge could be de-trapped in connection with the photo-transitions of the benzene ring and with the dipole relaxations.

The thermally-activated charge release shows a difference in the trap depth to its optical counterpart. This difference indicates that the trap levels depend on the de-trapping process and on the chemical nature of the trap site. That is, the processes of charge de-trapping from shallow traps are related to secondary forces. The processes of charge de-trapping from deep traps are related to primary forces. Furthermore, the presence of deep trap levels causes the stability of the charge for long periods of time.

Kurzfassung

Angesichts der Bedeutung der Ladungsspeicherung in Polymerelektreten für viele Anwendungen, wie z.B. in elektromechanischen Wandler, ist es das Ziel dieser Arbeit, zum Verständnis der zugrundeliegenden Mechanismen der kurz- und langfristigen Ladungsstabilisierung beizutragen sowie mögliche Haftstellen zu identifizieren. Ladungs- und Entladungsprozesse in Elektreten geben Hinweise auf Ladungshaftstellen. Diese Prozesse wurden mit thermischen und optischen Methoden bei gleichzeitiger Messung von Ladungs- und Polarisationprofilen untersucht. Die experimentellen Untersuchungen der vorliegenden Arbeit wurden an Polyethylenterephthalat (PETP) und an Cyclischen Olefin-Copolymeren (COC) durchgeführt.

PETP ist ein Photoelektret und weist in der Carbonylgruppe ($>C = O$) ein Dipolmoment auf. Die Elektreteigenschaften ergeben sich sowohl aus der Orientierungspolarisation als auch aus der Ladungsspeicherung. Im Gegensatz zu PETP ist COC kein Photoelektret und zeigt auch keine Orientierungspolarisation. Deshalb folgen die Elektreteigenschaften des COC ausschließlich aus der Ladungsspeicherung. Die COC-Proben wurden mit Farbstoffen dotiert, um das innere elektrische Feld zu untersuchen. Diese Systeme zeigen flache Ladungshaftstellen bei 0,6 und 0,11 eV, die durch thermisch stimulierte Prozesse entladen werden sowie tiefe Haftstellen bei 4 eV, die optisch stimuliert werden können.

PETP-Filme zeigen einen transienten Photostrom mit einem Maximalwert (j_p), der von der Temperatur mit einer Aktivierungsenergie von 0,106 eV abhängt. Der thermische Paarabstand (r_c) kann für die Photoladungsgeneration in PETP auf ca. 4,5 nm abgeschätzt werden. Die Photoladungsträger können rekombinieren, mit den gespeicherten Ladungen interagieren, über die Elektroden entkommen oder eine leere Haftstelle einnehmen.

PETP zeigt einen kleinen quasi-statischen pyroelektrischen Koeffizienten (QPC) von ca. 0,6 nC/(m^2 K) für nicht polarisierte Proben, ca. 60 nC/(m^2 K) für polarisierte Proben und ca. 60 nC/(m^2 K) für nicht polarisierte Proben mit Vorspannung ($E \approx 10$ V/μm). Wenn die gespeicherten Ladungen ein internes elektrisches Feld von ca. 10 V/μm generieren können, sind sie in der Lage, einen QPC herbeizuführen, der vergleichbar mit

dem von orientierten Dipolen ist. Es ist außerdem möglich, eine Ladungs-Dipol-Wechselwirkung zu beobachten. Da die QPM-Daten von PETP auf Grund des geringen Signals verrauscht sind, wurde ein numerisches Fourier-Filterverfahren angewandt. Simulationen zeigen, dass eine zuverlässige Datenanalyse noch bei einem Signal möglich ist, dessen Rauschen bis zu 3-mal größer ist als der berechnete pyroelektrische Strom.

Messungen der thermisch stimulierten Entladung von PETP-Filmen ergaben flache Haftstellen bei ca. 0,36 eV, welche mit der Dipolrelaxation der Carbonylgruppe ($>C = O$) assoziiert sind. Messungen der photostimulierten Entladung ergaben tiefe Haftstellen bei 4,1 und 5,2 eV. Die beobachteten Wellenlängen entsprechen Übergängen in PETP analog den $\pi - \pi^*$ Übergängen in Benzol. Die beobachtete Selektivität bei der photostimulierten Entladung lässt auf eine direkte Wechselwirkung von Photonen und Ladungen schließen. Einen zusäzlichen Einfluß auf die Entladung hat die Erzeugung von Photo-Exzitonen und deren Wechselwirkung mit den gespeicherten Ladungsträgern. Diese Ergebnisse deuten darauf hin, dass die Phenylringe ($-C_6H_4-$) und die Dipolgruppen ($>C = O$) eine zusätzliche Ladung in einer chemischen Resonanz stabilisieren und miteinander teilen können. Daher kann die gebundene Ladung auch durch einen Photoübergang im Benzolring oder durch eine Dipolrelaxation freigesetzt werden.

Die mittels thermisch stimulierter Entladung bestimmte Tiefe der Haftstellen unterscheidet sich deutlich von den mittels photostimulierter Enladung gemessenen Werten. Flachere Haftstellen werden bei der thermisch stimulierten Entladung gefunden und können sekundären Kräften zugeordnet werden. Die tieferen Haftstellen sind chemischer Natur und können primären Kräften zugeordnet werden. Letztere sind für die Langzeitstabilität der Ladung in Polymerelektreten veranwortlich.

Contents

Chapter 1

Introduction

Dielectric materials can be classified into passive or active dielectrics according to their applications (Williams, 1974). The passive application is the insulation of charges or conductors. In this application the relevant properties are the resistance, electric strength, dielectric losses ($\tan\delta = \varepsilon''/\varepsilon'$) and mechanical properties. Even though charge storage is not a desirable property, insulators are capable to store charges for long periods of time, and this could lead to a failure of the insulator, e.g. polyethylene terephthalate, polytetrafluoroethylene, polypropylene, polyethylene and polyolefines.

The active applications consist of the control of electric charges by storing the charge and releasing them with the appropriate excitation, such as light or electric field. In this way, it is possible to save information with a certain distribution of the charges and read back such information by identifying the spatial distribution of the charges. In order to implement this application, the material must be highly insulating. This allows the storage of charges, along with the desired information.

The dielectric materials which exhibit a "quasi-permanent" charge storage and/or dipole orientation are called *electrets*, after Heaviside (1885)[1]. The term "quasi-permanent" indicates that the time constants characteristic for decay of the charge are much longer than the time periods over which studies are performed on the electret (Sessler, 1999b).

Gray (1732) gave a description of the electret properties by studying the electrostatic attraction of different dielectrics such as waxes, resins, and sulphur. A century later, Faraday (1839) studied and described the electret as a "dielectric which retains an electric moment after the externally applied field has been reduced to zero". The systematic investigation began with Eguchi (1919) using similar materials as employed by Gray (1732). He introduced one important technique to form the electrets: the thermal method, which is described in the charging part of the section on experimental procedures (fig. 3.14). It was found that the charge may have either the same polarity –*homo-charge*– (Gemant, 1935) or opposite polarity –*hetero-charge*– to that of the electrode. In the following decades, electrets from a number of other substances were produced by charging techniques different from Eguchi's thermal method. A detailed historical review of the work performed on electrets is given by Sessler and Gerhard-Multhaupt (1999).

---

[1]Usually it is refered to Heaviside (1892) (Mellinger, 2004a)

Electrets are widely applied in engineering and science (Sessler and Gerhard-Multhaupt, 1999; Kestelman *et al.*, 2000). Due to their applications, electrets can be classified as active dielectrics (Williams, 1974). In polymeric electrets, charge storage and dipole orientation depend on many characteristics, such as chemical impurities, chemical constitution and conformation of the polymers, macro-molecular arrangements, degree of crystallinity, metal-insulator interfaces, interfaces at amorphous-crystalline regions in the material and mechanical stresses.

In the quest to describe the dielectric behavior of the electrets, several experimental techniques have been employed (Sessler and Gerhard-Multhaupt, 1999). In general, the electret polarization may consist of "real" charges at the surface and/or in the volume (bulk charges) of the polymer, "true" and/or "induced" polarization, and/or a combination of these.

Though chemical and physical characteristics of the polymeric systems have been identified to affect the dielectric properties of the electrets, microscopic mechanisms of charge retention are still poorly understood. One problem is the fact that the charges are well diluted in the material. Charged samples present a charge density of about 150 C/m^3 (sec. 4.1.7) for polyethylene terephthalate (*PETP*), which means that a charge carrier would be surrounded by a volume included in a cube with an approx. 0.1 μm edge. In the best of the cases, Mellinger (2004a) indicated that a charge is enclosed in a volume included in a cube with 40 nm edge for polytetrafluoroethylene (*PTFE*).

Forces present in polymeric systems are divided into primary and secondary with intra- and inter-chain interactions, respectively. These forces are able to stabilize the polymeric system (Billmeyer, Jr., 1984). Primary forces arise from covalent bonds which can achieve energies between 2 and 8.6 eV. Energy levels due to secondary forces range from 0.02 to 0.87 eV which arise from ionic bonding, dipolar interaction, hydrogen bonding and van der Waals interactions (Das–Gupta, 2001). If charge traps are associated to the secondary forces, the thermal excitation provides enough energy to perform changes in the polymeric system associated to the secondary forces and therefore to the carrier traps. However, von Seggern (1981) showed that it is possible to obtain information about traps up to 1.8 eV (in the bulk for *polyfluoroethylenepropylene*).

On the other hand, when charge traps are associated with the primary forces, trap energy levels are larger than 2 eV. In some cases, these can be affected by the thermal energy with a probable change of the conformation given by a rotation of a $\sigma-$bond. This assumption is usually used to explain the change of the polarization by the orientation of molecular dipoles which are present in the polymeric chain. Also, the effect of the primary forces on the charge retention could give a reasonable explanation about its long term storage of the charge. An alternative to probe those energy levels is the use of photon irradiation. This technique can easily reach energy levels up to 8 eV. One main difference of the light-irradiation technique to that of thermal-excitation technique is the selectivity of charge-detrapping energy levels. However, there is not an individual technique which can give a complete explanation of the charge trap retention mechanism, but a combination of several techniques.

Models have been proposed to explain the trapping of the charge carriers. A modified band model is normally used to explain the trapping and conduction in dielectrics (Rose,

1955; Bauser, 1972; Seanor, 1982; Sessler, 1999a; Gross, 1999). This model consists of delocalized states at the top of the valence band and at the bottom of the conduction band of the polymer. Additionally, it considers the existence of localized states (charge carrier traps) which are associated to certain molecules or molecular groups and distributed in the polymer. However, polymeric electrets are semi-crystalline and dynamic systems. The stabilization of the charge carriers is achieved by the environment of the so-called charge trap. The environment of the charge trap can be modified with the change of the structure of the material induced by an external aggent, such as temperature. In this sense, the picture of the modified band model can no longer be hold. Additionally, the charge conduction or detrapping is not considered to happen in the electret, unless the electret is appropriately excited.

At the interface of metal and polymer, Ieda *et al.* (1977) and Takai *et al.* (1977b) explained the trapping of charge carriers using the concept of barrier height and surface states. They explained that the polymer has trapping centers at the surface. Before contact, the surface states are filled. After contact, the charges stored in the surface states alter the potential barrier at the polymer surface, and the potential difference between the electrode and the polymer drops.

Meunier and Quirke (2000) and Meunier *et al.* (2001) performed molecular simulations of electron traps in polymer insulators considering physical (conformational) and chemical defects and chemical impurities. It was found that some of these defects are responsible for deep trapping of electrons and for the large trapping times. In some cases, charge trapping is not desirable due to the aging effect. The stored charge generates an electrical stress responsible for the failure of the dielectrics, when they are employed as electrical insulators (passive application). From this point of view, Dissado and Fothergill (1992) and Dissado *et al.* (1997) associated the aging and breakdown of the insulators to the charge accumulation in physical and chemical defects or additives.

In view of the importance that the trapped charge carriers in the polymeric electrets have to their applications, the aim of this work is to contribute to the understanding of the charge-retention mechanisms. In the same way, to explain how the long term storage mechanisms of charge carriers in polymeric electrets happen, and to identify which are the most probable hosts of the charge traps. The attempt to describe the dielectric behavior of a polymeric electret was pursued by means of a combination of different techniques.

In this work, the study was performed on polyethylene terephthalate films (PETP) and cyclic olefin copolymers (COC). PETP has been extensively used in applications, and therefore intensively studied. One of the early studies was performed by Creswell and Perlman (1970). They investigated thermally stimulated currents from corona charged PETP films and found the presence of electronic traps at 0.55, 0.85, 1.4, and 2.2 eV. Research on PETP using the thermally stimulated current technique identified several processes: molecular processes associated with the trapping sites (Frübing *et al.*, 1980), charge injection of the electrodes into the polymer film (Kojima *et al.*, 1978), discernment between bulk and surface traps (von Seggern, 1981), space charge formation and metal-PETP interface effects (Ieda *et al.*, 1977; Thielen *et al.*, 1996a,b, 1997). Also, the thermally stimulated current technique has been employed to describe the physical mechanisms of the electret behavior of PETP. Schneider *et al.* (1983) developed a qualitative

model. They employed the concept of *charge-dipole interaction* to describe the charging and discharging behavior of PETP. Additionally, Thielen *et al.* (1994) investigated the effect of the thermal treatment. They observed an increase of the charging current due to the increase of the degree of crystallinity and degradation caused by the thermal treatment.

Padhye and Tamhane (1978), Takai *et al.* (1978b), Takai *et al.* (1978c) and Ito and Nakakita (1980) applied the thermoluminescence (TL) technique to PETP films. Below the glass transition temperature, Padhye and Tamhane (1978) and Takai *et al.* (1978c) associated the TL glow-curves to the self-trapping mechanisms involved during irradiation of the sample. Takai *et al.* (1978c) estimated shallow charge trap depths to be approx. $0.23 - 0.5$ eV. On the other hand, Ito and Nakakita (1980) correlated a molecular process to the detrapping centers. This process was identified as the motion of the carbonyl group $\diagup C = O$ (β_1-relaxation) in the main chains.

Molecular relaxations can ease the charge detrapping of PETP. A change in the temperature generates a change in the trap environment due to the molecular movements. The dielectric spectroscopy can provide information about the molecular relaxations. Reddish (1950) performed the first detailed study on dielectric spectroscopy for this material. On a later work (Reddish, 1962), he related the chemical structure to the dielectric properties of PETP and other high polymers. Additional analysis performed by Sachez (1968) yielded the enthalpy of activation for the β-relaxation. Moreover, Ishida *et al.* (1962) and Coburn and Boyd (1986) analyzed the effect of the degree of crystallinity on the dielectric spectrum. They found that the frequency-temperature position and shape of β-relaxation loss-peak is independent of the degree of crystallinity, but not the magnitude of the peak. In contrast, the α-relaxation shifts to higher temperatures when the degree of crystallinity increases. A complete reference of the dielectric spectroscopy on PETP is given by McCrum *et al.* (1991).

The discharging of the electret implicates the presence of a certain carrier transport. The electric conductivity of PETP has been studied since the early 1960s (Amborski, 1962; Lilly, Jr and McDowell, 1968). Martin and Hirsch (1972) determined the negative charge carrier mobility as 1.5×10^{-6} cm^2/V·s. They found that the positive carriers were strongly localized. Later, Hayashi *et al.* (1973) showed that the mobility of both charge carriers depends on the temperature. They also showed that the hole mobilities are larger than those from the electrons.

Photo-charge detrapping is another way to probe the trap depths in the polymeric electrets. To apply this technique, it is necessary to identify the possible processes which can happen during light irradiation. Comins and Wintle (1972) studied the photoelectric effects on PETP films coated with aluminum electrodes. They concluded that the photo-current in the UV-region is due to hole injection of the electrodes into the sample. Sapieha and Wintle (1977) calculated a threshold energy of 2.85 eV, using the Fowler plot. Additionally, Takai *et al.* (1975) showed that the injection processes are controlled mainly by the work function of the electrode materials. Another process was observed by Takai *et al.* (1976, 1977c,b). They showed that the photo-current is also due to the photo-carrier generation in the benzene rings in PETP films.

Wintle and Sapieha (1977), Ieda *et al.* (1977) and Takai *et al.* (1977a) employed light irradiation to detrap charge carriers. Wintle and Sapieha (1977) observed photocurrent

peaks at 320 and 305 nm (3.88 and 4.07 eV, respectively) due to photo charge-detrapping. On the other hand, Ieda *et al.* (1977) reported photo charge detrapping and identified a trap level at 2.3 eV. Takai *et al.* (1977a) performed a combination of the thermally stimulated and photo-stimulated currents. These experiments yielded trap depths of 0.23 and 2.3 eV, respectively. It was observed that the traps were affected with the onset of the of molecular motions (Takai *et al.*, 1977a).

The knowledge provided by other techniques contributes with more elements to identify the trap-sites. Photo-luminescence (Takai *et al.*, 1978a; Ouchi *et al.*, 1999; Teyssedre *et al.*, 2001) and light-absorption (Ouchi, 1983) are also necessary to obtain more information from the material. Menczel *et al.* (1997) gave a survey on thermal characterization on PEPT films.

The analyis of the charge storage in cyclic olefin copolymers becomes less complex than for the PETP. This is due to the lack of molecular dipoles in their structure. Sessler *et al.* (1997) concluded that the electret properties of this saturated polymer arise from the storage of real charges. Mellinger *et al.* (2004b) reported the same behavior and the presence of trap depths at approx. 4 eV. However, the charge trap sites are not easy to be determined. These polymeric systems present photocurrents at high energy levels ($\sim$200 nm, 6.2 eV). Also, other polymeric electrets which are saturated polymers present a photocurrent at 200 nm. Ieda *et al.* (1977) reported photocurrents from polyethylene and polypropylene films in the UV-region. In this region, polypropylene cyclic olefin copolymers (fig. 3.11) and polyethylene (Partridge, 1966) present a strong light-absorption. The $\sigma-$bonds are the main reason for the light absorption at the UV-region ($\lambda \lesssim 220$ nm) in these saturated polymers.

Each one of the mentioned techniques provides a piece of the puzzle to describe the charge storage mechanism and the trap site in a polymeric electret. As it can be seen, a single technique is not enough to give a complete description of such a complex phenomenon: the charge storage. Nevertheless, a combination of these techniques results in a more complete description of the charge storage mechanisms in polymer electrets.

This work is divided into five chapters. The first one gives an introduction and a brief historical review of studies performed up to now on PETP and COC. The second chapter gives a conceptual background on photo-charge detrapping, photo-charge generation, photo-electronic processes, poling and charge storage. Parts of these topics were taken from Camacho González (2002). The third chapter explains the experimental techniques employed and the setup used to perform thermally stimulated current and photo-stimulated discharge experiments. The fourth chapter describes the experimental results and includes a discussion of the results and probable trapping mechanisms in a polymeric system. In the fifth chapter, the conclusions and further questions are presented.

Chapter 2

Conceptual background and available models

2.1 Electrical properties of highly insulating polymers

2.1.1 Orientation and relaxation of dipoles

In polar polymers, a polarization P is obtained through alignment of the polar groups by an applied field E at elevated temperatures. The alignment is described by the Debye equation (van Turnhout, 1999):

$$\frac{dP(t)}{dt} + \alpha_T P(t) = \varepsilon_0 (\varepsilon_S - \varepsilon_\infty) \alpha_T E, \tag{2.1}$$

where α_T, ε_S and ε_∞ are the single-dipole relaxation frequency, the static and the optical dielectric constant, respectively. Under isothermal polarizing conditions, and if $P(0) = 0$ is assumed, the time dependence of the polarization is:

$$P(t) = \varepsilon_0 (\varepsilon_S - \varepsilon_\infty) E (1 - e^{-\alpha_T t}) \tag{2.2}$$

which yields a saturation value of

$$P_S(\infty) = \varepsilon_0 (\varepsilon_S - \varepsilon_\infty) E \tag{2.3}$$

The temperature dependence of the relaxation frequency often follows the Arrhenius law:

$$\alpha_T = \alpha_r e^{-U/kT} \tag{2.4}$$

where α_r is the natural relaxation frequency, U the dipolar activation energy, and k is the Boltzmann's constant. Generally, polymers show a distribution of relaxation frequencies that may be discrete or continuous. In the case of discrete distributions, clearly separated

6
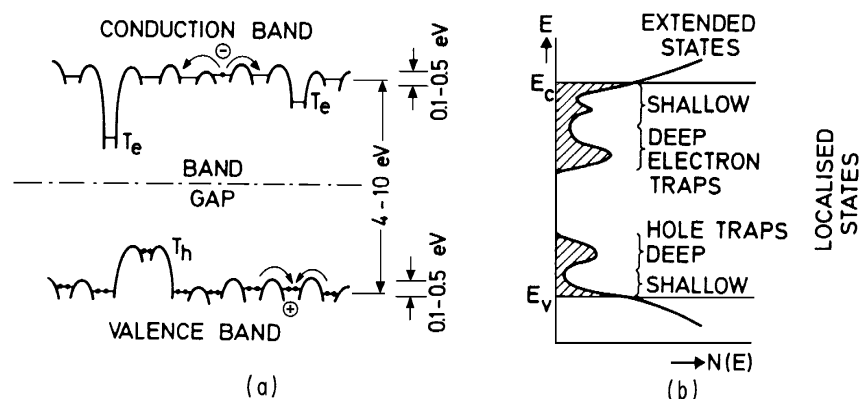
Figure 2.1: (a) Energy diagram for polymer, T_e electron traps; T_h hole traps (Bauser, 1972). (b) Localized states (traps) are shaded; E_c and E_v are mobility edges (Sessler, 1999c).

groups of relaxation frequencies exist, whereas such separations are not possible in the case of continuous distributions (van Turnhout, 1999).

In many polymers, three discrete relaxation frequencies exist, which are directly related to γ-, β- and α-relaxations. While the γ-relaxation is due to motions within side groups of the molecular chain, the β-relaxation originates from motions of the side groups themselves, and the α-relaxation is caused by joint motions of side groups and main chains (Sessler, 1982).

2.1.2   Storage of real charges

The quasi-permanent retention of real charges in polymer electrets is due to the presence of trapping states capable of holding charge carriers for a long period of time. Bauser (1972) suggested a model for charge trapping in polymers based on terms of a modified energy-band model (fig. 2.1). According to this model, traps are localized states belonging to certain molecules or molecular groups. Since polymers are amorphous or/and semi-crystalline, the energy levels, which are affected by their environment, are different in different molecular regions of the material. Thus, the trap depths are distributed in accordance to that.

Apart from these localized states (traps), there are delocalized states, generally refered to as extended states, which are energetically located near the bottom of the conduction band and the top of the valence band (fig. 2.1). They are separated from the localized states by the mobility edge at which the carrier mobility drops by several orders of magnitude. In such states carriers move by quantum-mechanical hopping. Charge trapping in extended states is generally negligible in electret materials. The extended states play a role in charge transport (Seanor, 1982).

Charge storage in polymers may occur in traps distributed on the surface and in the volume of the electret. While it is readily possible to distinguish between these categories, it is difficult to assess the molecular origin of the traps. Surface traps may be due to chemical impurities, specific surface defects, broken chains, adsorbed molecules, or differences in the short range order of surface and bulk. On the other hand, volume traps present three structural trapping levels (Sessler, 1982). The primary levels are atomic sites on the molecular chains, the secondary levels are between groups of atoms in neighboring molecules, and the tertiary levels are the crystalline regions or at crystalline-amorphous interfaces.

2.1.3 Effect of material parameters on polarization and charge trapping

The storage of electric charges in polymer electrets depends on a number of material parameters such as crystallinity, stereoregularity, additives and water absorption.

Physical nature and electronic properties of crystal defects (Pope and Swenberg, 1999). Crystal defects can be caused by the presence of chemical or physical impurities. They may either be located at specific lattice sites such faults are known as point defects, or they possess an extended character. In that case, they may exist as twin planes or coincident boundaries. The terms extended defects and extended faults refer to both linear and planar faults. Both the method and rate of crystal growth affect the number of inherent extended faults. The most important aspect of crystal defects is that they modify the available energy levels in their vicinity, often leading to the presence of accessible vacant orbitals in the forbidden gap E_g. Therefore, a carrier can become highly localized or trapped.

Traps situated on host molecules adjacent to a chemical impurity (Pope and Swenberg, 1999). It is possible that the chemical impurity is energetically inert as a carrier trap in the sense that its ionization energy is greater and its electron affinity is less than that of the host. Although the impurity does not act as a carrier trapping center, it nevertheless induces a local deformation of the crystal.

Traps situated on chemical impurities (Pope and Swenberg, 1999). An impurity molecule will in general have different energy levels from those of the host. In particular, its ionization energy and electron affinity is different, and these differences form the basis for the formation of carrier traps. As an example, if the ionization energy of the impurity is lower than that of the host, the impurity will behave as a hole trap. If the electron affinity of the impurity is greater than that of the host, the impurity will act as an electron trap. An impurity can behave both as electron trap and hole trap, although the trap depth will in general not be the same for each carrier.

In commercial polymers films, chemical impurities can be for instance oligomers, additives, UV-stabilizers and titanium oxide. These materials are meant to improve mechanical, optical, electrical and chemical properties of the polymer films. However, these chemical impurities are able to stabilize the charge carriers.

Electrostatic properties and chemical structure. It has been demonstrated that the chemical nature of the side-groups attached to the carbon-chain backbone of polymers

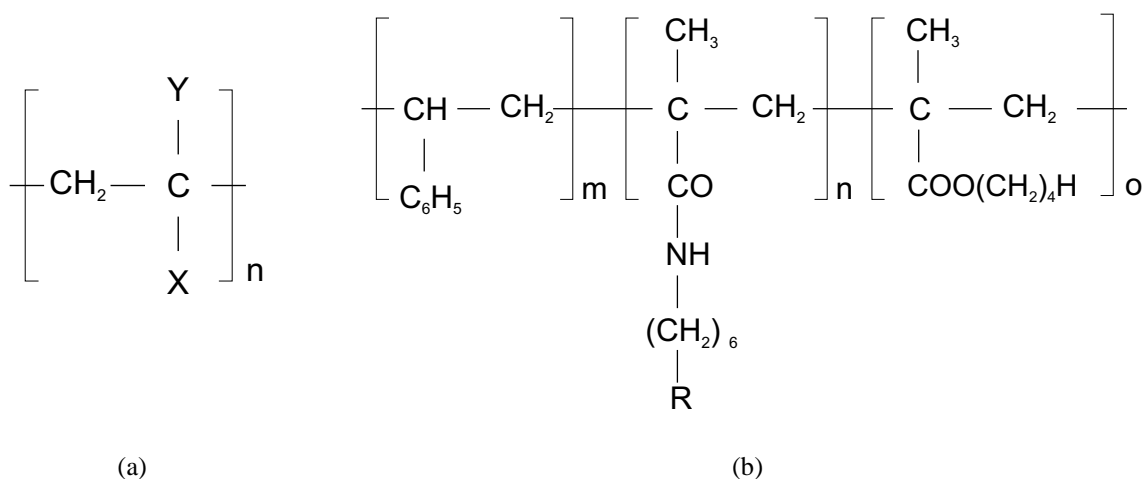(a)   (b)

Figure 2.2: Molecular structure of (a) polyolefins used to prove second-order effects for triboelectrification and (b) copolymer used to manipulate the triboelectrification properties (Gibson *et al.*, 1979).

also plays an important role for carrier traps (Ku and Leipins, 1987). In aromatic systems, for example, the substituents alter the energy levels of the $\pi-$orbital associated with the aromatic nucleus (Gibson, 1975). This in turn affects triboelectric charging.[1]

For a series of polyolefins of the structure shown in figure 2.2(a), a number of correlations were found. Gibson and Bailey (1977) showed a relationship between triboelectric charging and molecular structure by a correlation with gas and solution phase properties. Conformation, tacticity and morphology were found to be second-order effects. The preservation of the ordering of relative energy levels from gas to solution to solid states for organic molecules allows the prediction and control of the molecular level of relative charging based on gas and solution phase properties.

In another study, Gibson *et al.* (1979) performed the manipulation of the triboelectric charging properties of a copolymer with a systematic chemical modification (fig. 2.2(b)). Some of the major conclusions that were drawn from this study were:
1. Conversion of an alkyl ester to an alkyl amide results in an enhanced positive charging capacity.
2. Using R=H as a reference, the presence of amino or hydroxyl groups results in enhanced positive charging ability.
3. The polymers are negatively charged by acylation[2] of amine and hydroxyl groups.
4. Substituents on aromatic rings influence the charging as follows: methoxy deriva-

---

[1]**Triboelectrification (electrification by friction)**. The mechanical separation of electric charges of opposite sign by processes such as 1) the separation (as by sliding) of dissimilar solid objects, 2) interaction at a solid-liquid interface, 3) breaking of a liquid-gas interface (ANSI/IEEE Std. 100-1988, 1988)

[2]**Acylation** is the name of a chemical reaction where an acyl-group (R−CO−) links an organic molecule (Holum, 1996).
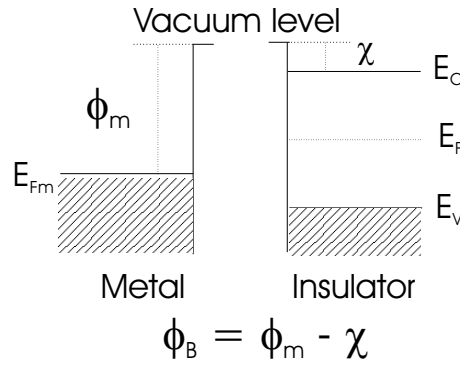
Figure 2.3: Schematic representation of energy levels for carrier injection. ϕ_B is the potential barrier; ϕ_m is the work function of the metal; χ is the electron affinity.

tive charges more positively than nitro derivatives; nitration results in diminished positive charging; and bromation gives similar results as nitration, but less pronounced.

2.2 Photoemission

Photoemission is generally referred to as emission of electrons into vacuum from a solid or as injection of electrons or holes from a solid into another solid. The photoemission of carriers from a solid into vacuum is referred to as external photoemission. While photoemission from a solid into another solid, such as from a contact electrode to a semiconductor, is called internal photoemission (Kao and Hwang, 1981).

Metallic contacts can be roughly classified into two groups, namely ohmic contacts and blocking contacts. An ohmic contact can be considered as a reservoir of carriers which is always ready to supply as many carriers as needed. Usually, at a given field, the ohmic contact can supply more carriers than the bulk material can carry. Thus the current is bulk limited. Further increase in current injection by photoexcitation does not affect the current, and therefore no photoemission current can be observed (Williams, 1974; Kao and Hwang, 1981).

A blocking contact can inject only very few carriers which are much less than what the bulk material can carry. Thus the current is contact limited. If light of energy $h\nu \geq \phi_B$ (where ϕ_B is the potential barrier height as shown in figure 2.3) is used to illuminate the metal contact, photoinjection from the contact will take place. The photoemission current (J_{ph}), without taking into account the effects of scattering and relaxation, can be written, according to the Fowler theory (Fowler, 1931), as:

$$J_{ph} = C(h\nu - \phi_B)^2 \quad \text{for } h\nu \geq \phi_B \tag{2.5}$$

This equation is valid only for $\phi_B \geq 0.5$ eV, if $h\nu \geq \phi_B$ is greater than some multiple of kT ($\geq 6k$T) and $h\nu \leq 1.5\phi_B$. Most metals, inorganic semiconductors and insulators satisfy these conditions (Kao and Hwang, 1981).
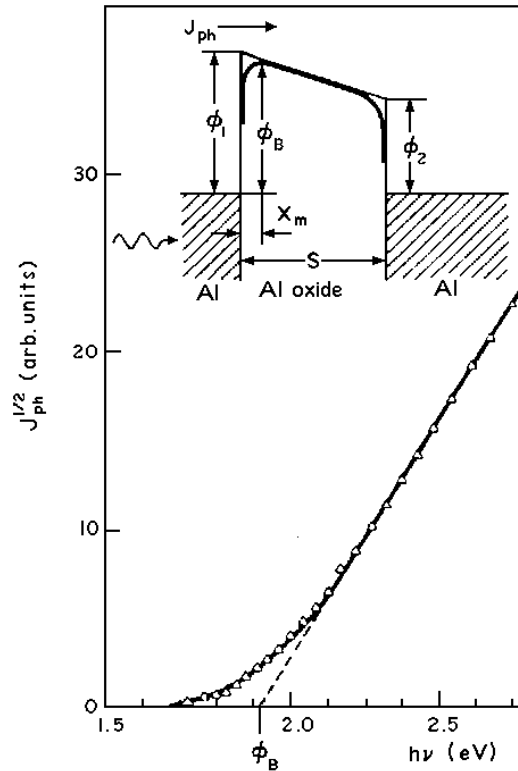
Figure 2.4: Square root of the photocurrent density ($J_{ph}^{1/2}$) as a function of incident photon quantum energy for an Al(100 nm)-Al$_2$O$_3$(3 nm)-Al(20 nm) structure with the 20 nm thick top electrode illuminated. The edges of the barriers are rounded off due to the image force as shown in the inset (from Kao and Hwang (1981)).

2.2.1 Photoinjection from a metal into wide-band semiconductors

In this case, the photoemission measurements would directly yield the barrier height of the blocking contact ϕ_B. By measuring the threshold energy $h\nu = \phi_B$ for electron emission and that for hole emission, the sum of these two threshold energies give the energy band gap of the material. For example, the threshold energy for electron emission from gold into n-GaP is 1.30 eV and that for hole emission from gold into p-GaP is 0.72 eV. The sum of these is 2.02 eV, which is about the energy gap of GaP, which is 2.18 eV. It should be noted that the barrier heights determined by means of photoemission measurements depend on the specimen surface conditions (Kao and Hwang, 1981).

For large band gap materials, the Fowler plot, in which the photocurrent density is plotted as a function of incident photon energy, at $h\nu$ close to $h\nu_0$ is usually not linear. Figure 2.4 shows a typical J_{ph}-versus-$h\nu$ curve for a MIM (metal-insulator-metal) structure. The asymmetry of the Al-Al$_2$O$_3$-Al ($\phi_1 > \phi_2$), shown in the inset of figure 2.4, is probably due to the different histories of the two interfaces. This deviation could be attributed to several factors (Kao and Hwang, 1981):

(i) The scattering of electrons in the conduction band may play a role, but it is likely that it is important for thick specimens and not for films thinner than 5 nm.

(ii) The quantum-mechanical transmission coefficient $T(E_x)$, which affects the photocurrent, is not equal to zero for $E_x < \phi_B$ because some of the electrons can tunnel through the potential barrier. $T(E_x)$ is not equal to 1 for $E_x > \phi_B$ because some of the electrons are reflected. This results in a smearing of the step-like form $T(E_x)$ and causes the deviation of the $J_{ph}^{1/2}$-versus-$h\nu$ curve. Here $E_x = mv_x^2/2$, and v_x is the normal component of the electron velocity.

(iii) It is possible that the barrier height is not uniform over the whole area of the interface.

2.3 Photocarrier generation

The process of photocarrier generation resulting from the dissociation of excitons, generally referred to as charge transfer process, is explained by Kao and Hwang (1981). Since in organic crystals molecules are held together by weak van der Waals forces, the properties of individual molecules are preserved despite the fact that they are bound into a lattice. Unlike inorganic crystals, the photogeneration of charge carriers in organic materials is mainly due to the dissociation of excitons. When an organic specimen is excited by light in the absorption region, Frenkel-type singlet and triplet excitons will be generated. The created geminate electron-hole pair has two possibilities of evolution. One possibility is that the pair may recombine and result in fluorescence or an increase of the thermal energy of the medium.

The other possibility is that the pair move and collide with the amorphous-crystal or electrode-insulator interfaces, impurities, or structural crystal defects, causing dissociation of the exciton. This process normally creates one type of carriers and capture of the other type of carriers at electrode surfaces, at impurities or structural defect sites.

The dissociation of the ion-pairs by Brownian motion subjected to a combination of Coulombic and applied electrical field, into free carriers, is described in terms of the Onsager theory of geminate recombination (Onsager, 1938). This model gives the probability $f(r, \theta)$ that a charge pair will escape geminate recombination and dissociate under the influence of an electric field in an isotropic system:

$$f(r, \theta) = \exp(-A)\exp(-B) \sum_{m=0}^{\infty} \sum_{n=0}^{\infty} \frac{A^m}{m!} \frac{B^{m+n}}{(m+n)!} , \qquad (2.6)$$

with $A = 2q/r$, $B = \beta r(1 + \cos\theta)$, $q \equiv e^2/8\pi\varepsilon\varepsilon_0 k_B T$, $\beta \equiv eE/2k_B T$. e is the electron charge. E is the electric field. ε and ε_0 are the relative and vacuum permittivities, respectively. θ and r are the relative coordinates of the charge carriers. k_B is the Boltzmann constant. T is the temperature.

Given the initial spatial distribution of thermalized pair configurations $g(r, \theta)$ in an isotropic medium, the overall carrier quantum yield ϕ may be written as:

$$\phi = \phi_0 \int g(r,\theta)f(r,\theta)dr, \tag{2.7}$$

where ϕ_0 is the ionization quantum yield.

A complete understanding of ϕ versus temperature requires the specification of the function $g(r)$. However, an informative analysis is obtained by approximating $g(r)$ with a delta function: $g(r) = (4\pi r_0^2)^{-1}\delta(r-r_0)$. After Batt *et al.* (1968), the quantum yield may be written as:

$$B(E,T) = \exp\left(-\frac{e^2}{4\pi\varepsilon\varepsilon_0 r_0 kT}\right), \tag{2.8}$$

where r_0 is known as Onsager radius or coulombic radius, and is the pair averaged thermalization-length (for more details refer to appendix A).

With this analysis Batt *et al.* (1968) demonstrated that, for intrinsic photogeneration of free carriers, an experimentally detectable activation energy of $E_A = e^2/4\pi\varepsilon\varepsilon_0 r_0$ is needed. This last assumption indicates that r_0 is independent of the electric field and the temperature, but is a characteristic which arises from the material parameters.

2.3.1 Exciton dissociation at electrode-semiconductor interfaces

Excitons produced in the crystal due to the light absorption will diffuse towards the electrodes. If the electrodes act as deep electron traps, then excitons approaching the electrode surface will be dissociated, resulting in subsequent trapping of the electrons and the freeing of the holes. It is obvious that the closer to the interface the excitons originate, the better the chance they have of reaching the interface and the more the charge carriers are created by exciton dissociation.

The exciton−surface dissociation process can be summarized by the following reaction equations:

$$S_1 + \text{surface} \quad \rightarrow \quad e(\text{or } h) \tag{2.9}$$
$$T_1 + \text{surface} \quad \rightarrow \quad e(\text{or } h) \tag{2.10}$$

where e and h denote the free electron and free hole, respectively; S_1 and T_1 are singlet and triplet excitons, respectively. The surface could be either a metal, an electrolyte electrode surface, or a dye-layer surface.

It should be noted that the non-radiative decay of a Frenkel exciton striking the interface not only results in exciton dissociation to produce a free carrier (charge-transfer process). It may also result in non-radiative energy transfer to cause a hot electron or hole injection from the metal in analogy to the photoemission process (energy transfer process). In fact, these two processes compete with each other. The potential barrier at the interface and the surface conditions determine which process is dominant.

2.3.2   Exciton dissociation due to interaction of excitons and trapped carriers

A trapped carrier may directly absorb a photon and thereby undergo a transition from the trapping level to delocalized states. There is an indirect detrapping process in which an exciton is first produced by the absorption of a photon, and then it transfers its energy to a trapped charge carrier. The efficiency of these detrapping processes for photogeneration of carriers is dependent on the concentration and the energy distribution of the traps in the material, and the intensity and wavelength of the exciting light.

Direct photon detrapping should be dependent on the wavelength of the exciting light. The excellent correspondence of the spectral response between the triplet absorption and the photogeneration of carriers supports the hypothesis that the excess photocarriers are generated by the interaction of triplet excitons and trapped carriers following the process (Kao and Hwang, 1981)
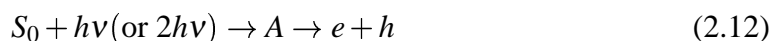
$$S_1 + e_t(\text{or } h_t) \xrightarrow{K_{Tct}} S_0 + e(\text{or } h). \tag{2.11}$$
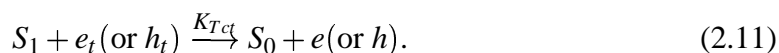
Where e_{ct} and h_t are the trapped electron and trapped hole, respectively, K_{Tct} is the rate constant for the triplet exciton detrapping, and S_0 is the ground state.

2.3.3   Auto-ionization (AI) processes

Auto-ionization processes are generally referred to as the processes in which excitons are produced by the absorption of one or more photons, which then either spontaneously dissociate into free carriers or decay to low-lying non-ionizing states. Several mechanisms are responsible for electron−hole pair generation through light absorption in organic materials. Bergman and Jortner (1974) identified three AI-processes in antrancene. Fig. 2.5 shows an schematic diagram of the auto-ionization processes.

(i) Exciton auto-ionization. For direct excitation from a ground state S_0 to a metastable state A, which is above the direct threshold to the conduction band (E_c), the decay of the metastable state A will yield free charge carriers. This process may involve one or two photons.
$$S_0 + h\nu(\text{or } 2h\nu) \rightarrow A \rightarrow e + h \tag{2.12}$$
This process competes with the internal conversion back to S_1,

$$S_0 + h\nu(\text{or } 2h\nu) \rightarrow A \rightarrow S_1 + \text{phonons} \tag{2.13}$$

with the involvement of excited states located below the direct threshold to the conduction band.

(ii) Exciton photoionization. The excited states are located below E_c. The decay of the metastable state A will yield charge carriers via AI. For the singlet exciton photoionization, the process is
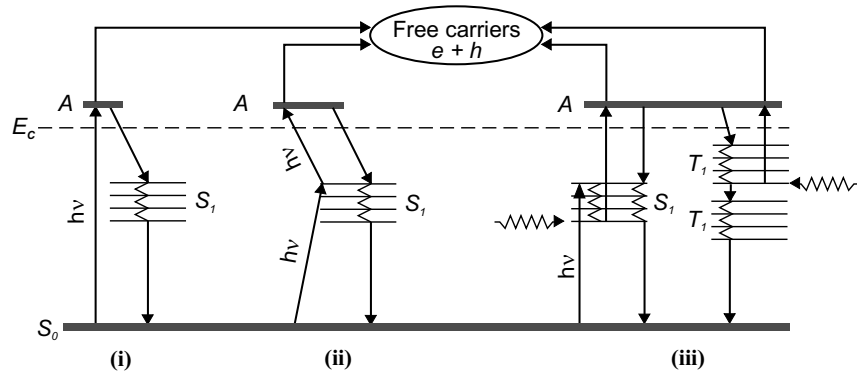$$S_0 + h\nu(\text{or } 2h\nu) \rightarrow S_1 \tag{2.14}$$

Figure 2.5: Auto-ionization processes. Exciton auto-ionization (i), exciton photoioniza-tion (ii) and exciton collision ionization (iii). A, metastable state; E_c, direct threshold to the conduction band; S_0, ground state; S_1, singlet state; T_1, triplet state; hν, photon energy; $\leadsto$, phonon.

$$S_1 + h\nu \rightarrow A \rightarrow e + h \tag{2.15}$$

This process competes with the internal conversion back to S_1

$$S_1 + h\nu \rightarrow A \rightarrow S_1 + \text{phonons}. \tag{2.16}$$
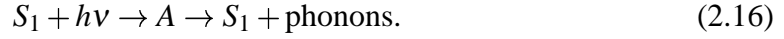
It should be noted that the process given in eqn. (2.14) is not limited to the involvement of singlet excitons only. It can be a three-phonon process involving also triplet states.

(iii) Exciton collision ionization. Two vibrationally relaxed singlet excitons collide and then yield a metastable state A. The decay produces charge carriers via AI following the process:

$$S_0 + h\nu(\text{or } 2h\nu) \rightarrow S_1 \tag{2.17}$$
$$2S_1 \rightarrow A \rightarrow e + h \tag{2.18}$$

This process can also include triplet states, and is competing with the internal conversion process

$$2S_1 \rightarrow A \rightarrow S_1 + \text{phonons}, \tag{2.19}$$

or

$$2S_1 \rightarrow A \rightarrow T_1^* + T_1^* + \text{phonons}. \tag{2.20}$$
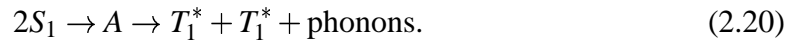
It has been reported that singlet-triplet collision can also lead to AI following the process (Fourny *et al.*, 1968)

$$S_1 + T_1 \rightarrow A \rightarrow e + h. \tag{2.21}$$

2.4   Photoconduction process

Photogeneration of charge carriers always results in free electrons and holes in the bulk of the material. Both species migrate, become trapped or recombine in the material. If diffusion is neglected the current j is given by

$$j = \sigma E = e(\rho_e \mu_e + \rho_h \mu_h)E, \tag{2.22}$$

where e is the unit charge, σ the conductivity, E the electric field, ρ_e and ρ_h are the densities of the electrons and holes, respectively, and μ_e and μ_h are the electron and the hole mobilities. Photoconductivity is observed when the charge carrier densities increase upon illumination, raising with this the current. The difference of the current with and without illumination is known as photocurrent j_{photo},

$$
\begin{align}
j_{photo} &= j_{light} - j_{dark} \tag{2.23} \\
&= e((\rho_{e0} + \Delta\rho_e)\mu_e + (\rho_{h0} + \Delta\rho_h)\mu_e)E - e(\rho_{e0}\mu_e + \rho_{h0}\mu_h)E \tag{2.24} \\
&= e(\Delta\rho_e \mu_e + \Delta\rho_h \mu_h)E, \tag{2.25}
\end{align}
$$

where ρ_{i0} is the dark and $\Delta\rho_i$ the photogenerated charge density (i denoting electrons or holes). The latter can be expressed in terms of lifetimes τ_i of the photoexcited charge carriers.

If the photoconductor is homogeneously illuminated the generation rate f is given by

$$f = \phi \frac{\alpha I}{\hbar \omega} = \frac{\Delta\rho_i}{\tau_i}, \tag{2.26}$$

where I is the light intensity, α the absorption coefficient and ϕ the dimensionless charge carrier photogeneration efficiency. j_{photo} can be rewritten using the eqns. 2.26 and 2.25:

$$j_{photo} = \Delta\sigma E = fe(\tau_e \mu_e + \tau_h \mu_h)E \tag{2.27}$$

In general, the photocarriers in molecular solids result from one or more of the following processes:

1. Processes involving the dissociation of excitation:

    (a) exciton dissociation at the electrode/insulator interface;

    (b) exciton dissociation due to the interaction of excitons and trapped carriers

    (c) auto-ionization process;

    (d) exciton dissociation due to the interaction of excitons and impurities.

2. Processes not involving excitons:

    (e) direct excitation of trapped carriers into the conduction or valence bands;

    (f) direct band-to-band transitions.

Processes (a), (b), (d) and (e) are characteristic of an extrinsic photoconduction and usually occur at lower excitation energies (longer wavelengths), whereas an intrinsic photoconductivity is mainly due to processes (c) and (f) (Nespurek *et al.*, 1996).
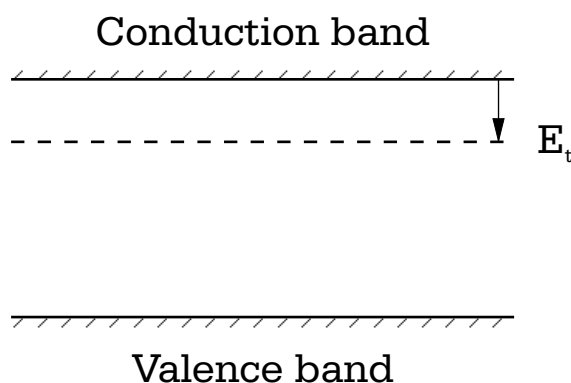
Conduction band

Valence band

Figure 2.6: Band model for photoconductor with single level of traps (E_t) .

2.5 Photo-stimulated discharge (PSD) spectroscopy

During light irradiation of polymeric films with stored charges several processes can happen which could affect the stored charge distribution. These processes could be

- direct photon-charge interaction generating charge detrapping,
- photo-exciton generation which can interact with the stored charges,
- light generation by radiative recombination of free carriers which is absorbed and builds charge up or has direct photon-charge interaction,
- photoemission,
- retrapping of the free carriers.

Brodribb *et al.* (1975) described the photon-stimulated current technique for the examination of defect levels in insulators and semiconductors and presented a quantitative analysis. This method involves a sample already charged at constant temperature (normally low temperature) which inhibits thermal release of charge or change of the charge environment. In this state, the sample is irradiated with nearly monochromatic light whilst the sample current is monitored as a function of the wavelength which is scanned from the far-infrared up to the band-gap energy of the particular sample.

In general, for wide-band materials the trap depth corresponds to the long wavelength cut-off of the peak, whereas in narrow-band materials, the peak of the spectrum corresponds closely to the trap depth.

For the analysis of PSD, an approximation of the model proposed by Bauser (1972) is considered (fig. 2.6), with a single level of trapping centers (in this case electron traps) at E_t below the conduction band. The density of these traps is N_t, their capture cross section is S_t, and n_t represents the density of occupied traps. The analysis of the energy of the traps is straightforward and can be obtained directly from the spectrum. However, in order to evaluate the density of the traps and their capture cross section, an auxiliary experiment is required. This consists of irradiating the charged sample with photons whose energy is just sufficient to excite the trapped charge into the conduction band,

while the photocurrent is monitored as function of time during irradiation. This yields a transient current behavior.

As it can be observed, Brodribb *et al.* (1975) delimited his analysis to the direct photo-charge detrapping, but not indirect photo-detrapping. After the charge has been photo-released from the traps, it may stay in the conduction band until

- · it recombines with a carrier of opposite sign,
- · it is removed at one of the electrodes, or
- · it is retrapped.

The complete equations for the rates of change of the free-carrier density and the trapped charge density are:

$$\frac{dn_c}{dt} = -\frac{dn_t}{dt} - \frac{n_c}{\tau} \tag{2.28}$$

$$\frac{dn_t}{dt} = -gn_t + (N_t - n_t)n_c v_{th}S_t - n_t \nu \exp\left(-\frac{E_t}{kT}\right) \tag{2.29}$$

where N_t is the trap density, n_t is the density of occupied traps, n_c is the free carrier density, v_{th} is the thermal velocity, ν is the 'attempt-to-escape frequency' of carriers in the traps, S_t is the capture cross section, g is the product of the density of photons irradiating the sample (photons cm^{-2} s^{-1}) and the effective interaction cross section of the photons and the carriers in the traps, and τ is the effective lifetime of the carriers in the conduction band. The exact nature of this life time is dependent on the type of material under investigation. For a semiconductor, it is related to the density of recombination states, whereas for an insulator containing a space charge it will be a complex function of the mobility of charge in the material, the applied voltage and the electrode spacing. Normally, the sample is held at such a temperature that virtually no thermal release of charge takes place during the time taken for the experiment. Thus, the last term in equation (2.29) can be neglected.

In the following subsections, the analysis where no retrapping occurs is described. Then, the generalization to the retrapping case is presented.

2.5.1 Non-retrapping case

When the retrapping process is neglected, equation (2.29) simplifies to

$$\frac{dn_t}{dt} = -gn_t. \tag{2.30}$$

The approximation is justified if the traps are nearly full ($n_t \approx N_t$) or if the capture cross section S_t is very small. The substitution of the solution of equation (2.30) into equation (2.28) yields an expression for n_c:

$$n_c = \frac{gn_{t_0}}{\tau^{-1} - g}(e^{-gt} - e^{-t/\tau}), \tag{2.31}$$

where n_{t_0} is the initial concentration of charge in the traps.

In practice, due to the poor efficiency of the trap-emptying process $g \ll \tau^{-1}$, the rise-time of the transient is much shorter than the time decay. Therefore, the decaying portion of the transient curve can be described by the following expression:

$$n_c = g\tau n_{t_0} e^{-gt} \tag{2.32}$$

To obtain the initial concentration of the trapped charge, it is necessary to evaluate τ. This can be done by differentiating equation (2.32), equating to zero and solving for t. An expression for the time taken to the peak t_p of a transient curve of the charge decay can be obtained:

$$t_p = \tau e^{-g\tau} \tag{2.33}$$

2.5.2 Retrapping case

The equations for the retrapping case are:

$$\frac{dn_c}{dt} = -\frac{dn_t}{dt} - \frac{n_c}{\tau}$$
$$\frac{dn_t}{dt} = (N_t - n_t)n_c v_{th} S_t - gn_t \tag{2.34}$$

with the thermal-release term neglected as before.

To solve this case, the situation at times beyond the peak of the current transient, i.e. the decay portion, is considered. In this region, $dn_c/dt \ll dn_t/dt$ and n_c/τ, and consequently the following approximation can be made:

$$n_c = -\tau \frac{dn_t}{dt}. \tag{2.35}$$

Solving equation (2.35) with $n_t(t=0) = n_{t_0}$, and substituting first in the second equation of the set (2.34) and then in equation (2.35) yields:

$$n_c \left(-\frac{1}{\tau} + (n_{t_0} - N_t)v_{th}S_t \right) = \left(\frac{g + n_c v_{th} S_t}{\tau} \right) \int n_c dt - gn_{t_0}. \tag{2.36}$$

Considering the system at different times t_1 and t_2 with the corresponding values of the integrals $\int n_{c1} dt$ and $\int n_{c2} dt$ represented as A_1 and A_2 respectively, assuming that all the traps are full at $t=0$ ($n_{t_0} = N_t$), and multiplying throughout by $\tau/g(n_{c2} - n_{c1})$ yield:

$$-\frac{1}{g} = \left(\frac{A_2 - A_1}{n_{c2} - n_{c1}} \right) + \frac{v_{th}S_t}{g} \left(\frac{A_2 n_{c2} - A_1 n_{c1}}{n_{c2} - n_{c1}} \right). \tag{2.37}$$

Thus, varying t_2 and plotting $(A_2 - A_1)/(n_{c2} - n_{c1})$ versus $(A_2 n_{c2} - A_1 n_{c1})/(n_{c2} - n_{c1})$ gives a straight line, $-v_{th}S_t/g$ is given by the slope, and $-1/g$ is given by the ordinate intersection, which gives $v_{th}S_t$, and hence the capture cross section of the trap.

Chapter 3

Experimental techniques

3.1 Methods of charging and poling

Electrets formed by thermal methods are referred to thermoelectrets and those formed with light irradiation are called photoelectrets. Sessler (1999c) summarizes the different methods employed for the orientation of dipoles and/or building up of real charges in an electret. Basically all them apply an electric field to the sample under certain conditions. The name of the method depends on the way of applying the electric field. Corona discharge and contacting electrodes methods are two of the charging techniques which were employed in this work to orient dipoles and/or build up real charge. These two methods are described in the following subsections.

3.1.1 Corona discharge method

The corona discharge method has been fully investigated by different authors (Nasser, 1971; Gallo, 1975; Giacometti and de Oliveira Jr., 1992). The sample is exposed to a high voltage in a point–plate arrangement (fig. 3.1). Sometimes a control grid is used. The back electrode which holds the sample is solid grounded [1] and connected to a temperature control to vary the temperature of the sample. The charge generated by this method can be either a surface or volume charge. This depends on the temperature of the sample during charging. At high temperatures, just below the glass transition temperature (70 and 120 °C for TOPAS® 8007 and 6013, respectively), both volume and surface charges are present. On the other hand, at room temperature, the mean charge is at the surface. The effect of a corona discharge is produced only in a gaseous atmosphere. Due to thermal degradation, not all materials can be volume charged with this method in presence of oxygen. Other gases, such as nitrogen, can be used to charge at high temperatures.

If a high electric field is applied to a needle or a sharp blade, the air at the tip or edge gets ionized. The ionized particles, charged at the same polarity as the tip, are driven towards

---

[1]**Solid grounded**. Grounded through an adequate ground connection in which no impedance has been inserted intentionally. Note: adequate as used herein means suitable for the purpose intended (ANSI/IEEE Std. 100-1988, 1988)
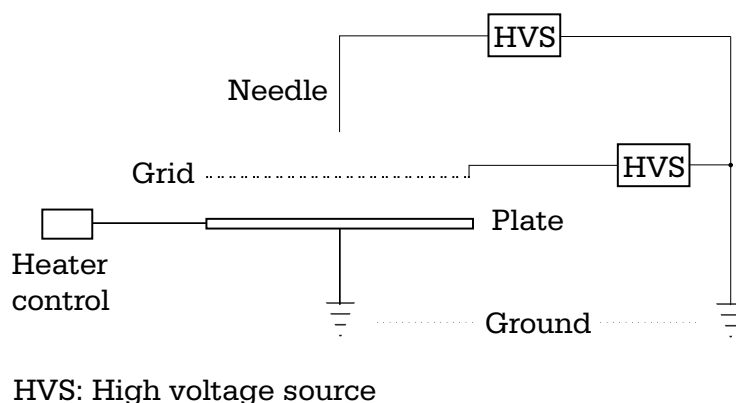
Figure 3.1: Schematic corona poling setup.

ground by the electric field. This effect can be exploited to charge a sample. When the corona discharge starts, the ions are deposited on the sample surface. If the sample is electrically insulating, the charges remain on its surface and build up an electric field between the surface and the grounded plate. Thus, a charging field is applied. Otherwise, the ions will penetrate the sample. Inside the sample they are neutralized by opposite charges coming from the grounded surface. Thus, no charging field will be present inside the sample.

During charging, the surface potential can be regulated with a metallic grid between corona source and sample (figure 3.1). The maximum surface potential roughly equals the potential of the grid. If the surface potential rises to the grid potential the field between grid and sample vanishes. Then, all charges from the corona discharge are captured by the grid. Thus, a higher surface potential cannot be achieved.

Breakdowns between the surface charge and the ground can result in small pinholes. If the surface is not conductive the defect does not have a strong effect on the poling procedure because the charges cannot move towards the hole, and therefore the poling field is still present.

The advantages of this method is the simple setup, and the speed of charging. A drawback in setups without grid electrode is the relatively large lateral non-uniform charge distribution.

3.1.2 Contacting electrodes method

The application of the electric field at an elevated temperature and subsequent cooling while the field is still applied give rise to orientation of dipoles and trapping of charge carriers in the bulk. For polymer films, high temperatures are around glass transition temperature. The electric field can be applied through evaporated electrodes or pressed-on electrodes.

The photoelectret process and the thermal charging and poling methods are variants of the contacting electrodes method. In the photoelectret process, the sample is coated with
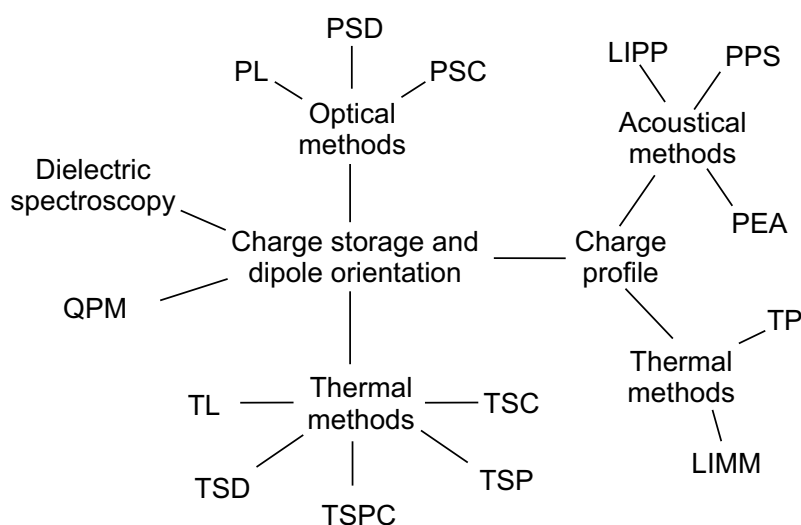
Figure 3.2: Techniques employed to characterize the charge storage and dipole orientation processes. PL: photo-luminescence, PSD: photo-stimulated discharge, PSC: photo-stimulated current, TL: thermo-luminescence, TSD: thermo-stimulated discharge or depolarization, TSP: thermo-stimulated polarization, TSC: thermo-stimulated current, TSPC: thermo-stimulated polarization current, QPM: quasi-static pyroelectric measurement, LIMM: laser intensity modulation method, TP: thermal pulse, PPS: Piezoelectrically generated pressure-step method, PEA: Pulse electro-acoustic method and LIPP: Laser-induced pressure-pulse method.

semi-transparent electrodes and is irradiated with ultraviolet or visible light under an applied electric field (Sessler, 1999c). The generation of charges is attributed to photo-exciton generation, separation and transport of the pair charge-carriers with an eventual trapping of the carriers. The photo-exciton generation is caused by light of the wavelengths at the optical-absorption peaks of the photo-electret. The separation of the pair charge-carriers depends on the applied electric field and temperature, giving a probability of charge separation (Onsager, 1938). The charges can be accumulated at the dielectric-electrode interfaces or in the bulk depending on the mobilities of the charge-carriers and the uniformity of the light irradiation through the thickness of the sample (Sessler, 1999c).

3.2 Characterization of charge storage and dipole orientation

When the material is exposed to an external excitation (like the electric field and temperature), the orientation of permanent dipoles (in polar materials), trapping of charges and their interactions are merged in the overall electrical response. In order to distinguish between these processes, a combination of different techniques is needed. Figure 3.2 shows an schematic diagram of the methods employed to characterize charge storage and dipole orientation.
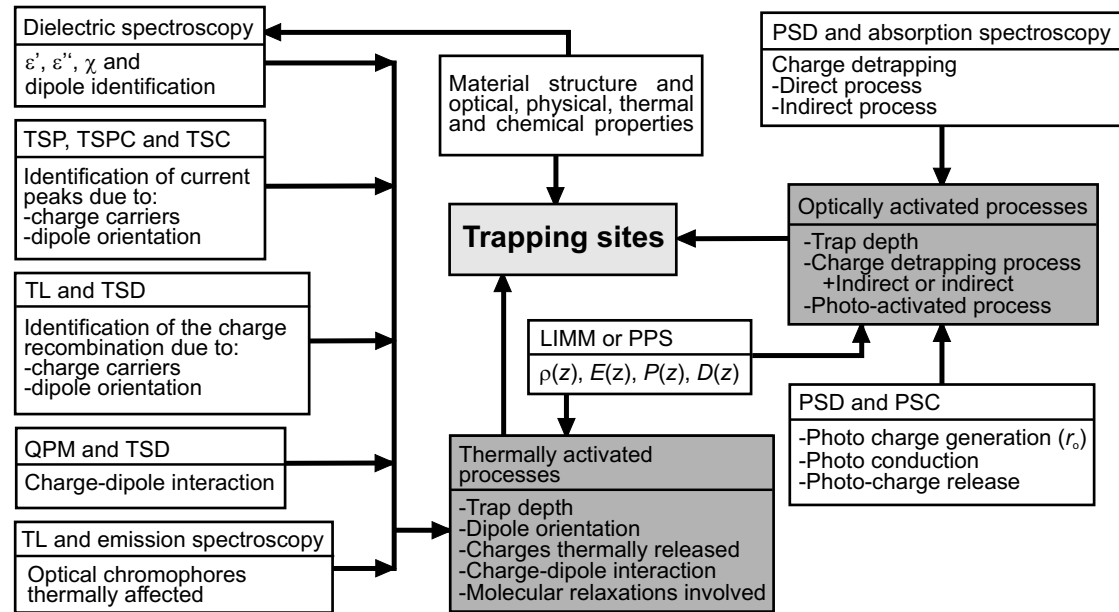
Figure 3.3: Characterization of the trapping sites performed by the combination of the methods shown in fig. 3.2. Gray boxes are processes and white boxes are methods. ε': permittivity, ε'': losses, χ: degree of crystallinity, $\rho(z)$: charge density profile, $E(z)$: internal electric field, $P(z)$: polarization profile and $D(z)$: electric displacement. Acronyms: PL: photo-luminescence, PSD: photo-stimulated discharge, PSC: photo-stimulated current, TL: thermo-luminescence, TSD: thermo-stimulated discharge or depolarization, TSP: thermo-stimulated polarization, TSC: thermo-stimulated current, TSPC: thermo-stimulated polarization current, QPM: quasi-static pyroelectric measurement, LIMM: laser intensity modulation method, TP: thermal pulse and PPS: Piezoelectrically generated pressure-step method.

A short introduction of the techniques applied in this work is given in the following sub-sections. The techniques used to determine the energy-trap levels and dipole orientation activation-energy can be classified into optical and thermal methods. Nevertheless, additional information to determine the nature of the detrapping process is needed. This can be given with the help of dielectric spectroscopy, quasi-static pyroelectric measurement, charge and dipole orientation profiles, and photo-luminescence. The combination of these methods (white blocks in fig. 3.3) can provide the information required to identify the thermally and the optically activated processes (gray blocks in fig. 3.3) responsible for the charge trapping and detrapping. The yielded information give the trace to identify the trap sites in the polymer.

3.2.1 Thermal methods

Thermo-stimulated currents (van Turnhout, 1999). The dipoles and charges regain their freedom of motion when an increase of temperature takes place. In the *thermally-stimulated discharge* or *depolarization* (**TSD**) method, the temperature of a charged or poled sample is linearly increased. This generates a current which is recorded showing a number of peaks as a function of temperature. The shape and location of these peaks show the characteristics of the trapping parameters and dipole orientation mechanisms. In the TSD current-thermograms, the dipole and charge effects are merged in a signal.

The *thermo-stimulated polarization* (**TSP**) is an extended version of the TSD. Contrary to the TSD, TSP measures the currents of charging and poling while the sample is heated lineraly. In addition to the current peaks due to charge storage and dipole orientation, it is possible to observe a steadily increase of the of the conduction currents at high temperature. These currents merge in a single signal.

To discern between the dipole orientation, real charge release processes due to thermal activation and the conduction currents, McKeever and Hughes (1975) proposed the combination of the TSP, *thermally-stimulated current* (**TSC**) and the *thermally-stimulated polarization current* (**TSPC**). Fig. 3.4 depicts the measurement of the charging and poling currents of a sample during a series of thermal charging and/or polarizations. In the TSPC, without the previous photoexcitation, the thermo-current is due to the dipoles alignment. An extra cycle is performed in order to make a "cleaning" (*zero*-cycle in fig. 3.4). This *zero*-cycle is mainly due to the conduction current and the volume effect. After the *zero*-cycle, a TSC measurement is performed. The photoexcitation with UV-light produces electron-hole pairs, which settle down in traps upon thermal release from which they give rise to transient peaks.

Thermo-luminescence (McKeever, 1988). In *thermo-luminescence* (**TL**), the sample is cooled to low temperatures ($\lesssim -180$ °C) and irradiated with a light source at the wavelength of the maximum absorption of the sample. During this irradiation, some free carriers are generated and trapped. Luminescence generated during a subsequent linear increase of the temperature is detected by a photomultiplier. The photon intensity is recorded as function of temperature. In this way, the peaks appearing in the emitted light versus temperature curves are specific for the activator and coactivator of recombi-
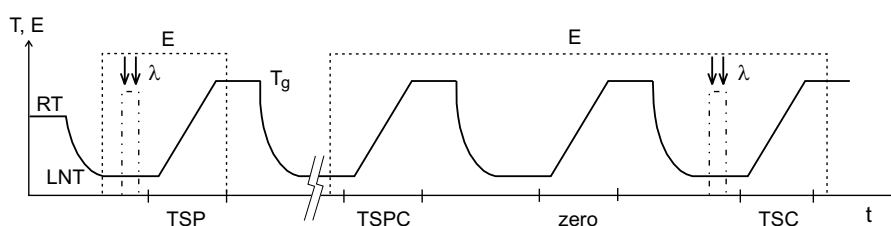
Figure 3.4: Experimental procedure diagram of the thermally-stimulated currents. Identification of polarization and charging processes with the help of thermo-stimulated polarization current (TSPC) and thermo-stimulated current (TSC) when a thermo-stimulated polarization (TSP) takes place. E: electric field, T: temperature, T_g: glass transition temperature, RT: room temperature, and LNT: liquid nitrogen temperature.

nation centers. It is also important to remember, that the charge-carriers recombination is activated by thermal processes.

3.2.2   Optical methods

Photo-stimulated currents (van Turnhout, 1999; Mellinger *et al.*, 2004a). Deep charge-trap levels (≥ 3 eV) can be investigated with the help of photo-stimulated currents. Unlike the thermal methods, the sample is kept at constant temperature during the experiment. The *photo-stimulated current* (**PSC**) and *photo-stimulated discharge* (**PSD**) are variants of the photo-stimulated currents.

In the PSC method, an uncharged sample is exposed to an electric field while the photocurrent is recordered. In constrast, in the PSD technique a sample is previously charged and the photocurrent is registered. Monochromatic light is generated by a light source and a monochromator and is directed onto the sample. The light wavelength is scanned while the photocurrent is recorded. This shows a number of peaks as a function of the wavelength. The location of these peaks gives information about the energy levels of the trapping parameters and centers.

Light-absorption and -emission. Optical detrapping of carriers can be achieved by indirect processes which are optically activated. Whenever light irradiation of a material takes place, the optical properties such as light-absorption and -emission are required.

In the absorption spectrum, the sample is irradiated with monochromatic light. The absorbed light is plotted versus the wavelength. The peaks resulting from the absorbed light are characteristic of the excited states of chemical species, molecules, or aggregates.

Emission or luminescence is referred to as fluorescence or phosphorescence, depending on whether it corresponds to a spin-allowed or forbidden transition, respectively. In a photo-luminescence spectrum, the light emitted is plotted versus the wavelength, giving characteristic peaks which represent the radiative transition states in the molecule. Frequently, it is observed that the fluorescence spectrum is a mirror image of the absorption spectrum.

3.2.3 Quasi-static pyroelectric measurement

The pyroelectric effect is observed when the sample generates a current after been exposed to a change of temperature. Consider a pyroelectric film with its electrodes in short-circuit. If this sample is exposed to a variation of temperature, the zero potential is maintained by the flow of the charge generated when the electrodes come closer due to the sample contraction. This phenomenom is known as the *secondary pyroelectric* effect. Pyroelectricity rises from the change of the dipole density. In the simplest case, in which the short circuit current is measured while the temperature is changed, one obtains:

$$p = \left. \frac{\partial D}{\partial T} \right|_{E=0,P} = \left. \frac{1}{A} \frac{\partial Q}{\partial T} \right|_{E=0,P} \tag{3.1}$$

where the p is the pyroelectric coefficient, D is the electric displacement, Q is the image charge at the electrode, A is the electrode area, and P is the pressure. When the thermal signal is sinusoidal, the current due to the dipoles is determined by the current delayed by 90 ° (appendix B). In small pyroelectric signals, the current can be analyzed using Fourier transform analysis (sec. 4.1.6).

3.2.4 Dielectric spectroscopy

In this technique, the dielectric permittivity ε' as well as the losses ε'' are measured as a function of frequency and temperature (Fröhlich, 1958; McCrum *et al.*, 1991; Kremer, 2002). Dynamic processes from dipoles and charge carriers as kinetics and interactions are merged in a signal plotted against the frequency and temperature. These dynamic processes can be identified by their characteristic frequency of relaxation (Debye, 1945; Havriliak and Negami, 1966).

In isothermal conditions, the α-relaxation is located at low frequencies and related to the glass transition in the amorphous part of the material. At higher frequencies, local intra-molecular movements are present forming the β-relaxation. Sometimes, the β-relaxation is followed by the γ-relaxation where molecular units are present. Finally, the δ-relaxation can be present in the high frequency part of the spectrum. This relaxation is due to isolated molecules of impurities (Strobl, 1997).

3.2.5 Charge and dipole profile determination

The determination of the charge and dipole distribution can be achieved by different techniques (Sessler, 1999c). At present, electro-acoustic techniques have been widely employed. These techniques are the piezoelectrically pressure-step generated method PPS (Gerhard-Multhaupt *et al.*, 1983), pulsed electro-acoustic method PEA (Maeno *et al.*, 1988) and laser-induced pressure-pulse method LIPP (Sessler *et al.*, 1981; West *et al.*, 1982). In this work, thermal techniques (Laser Intensity Modulation Method, LIMM (Lang and Das-Gupta, 1981) and Thermal Pulse Method, TP (Collins, 1976)) were more
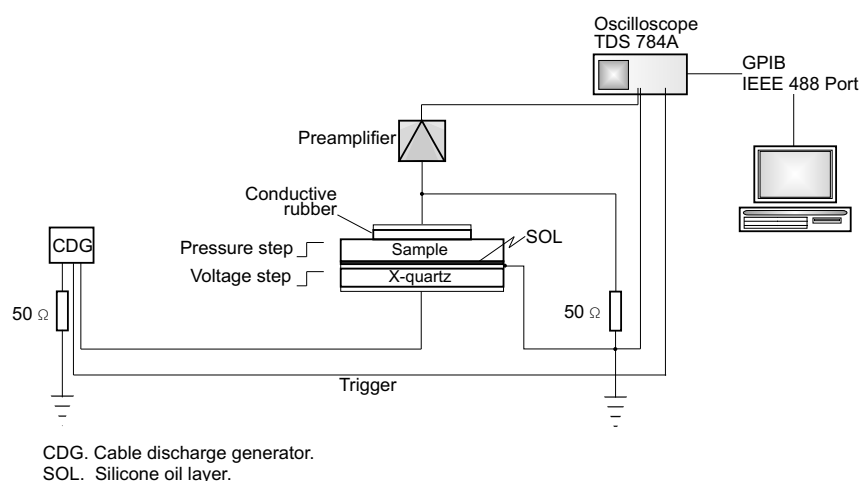
Figure 3.5: Schematic representation of the Piezoelectrically Generated Pressure-Step (PPS) Method (Camacho González, 2002).

employed than the PPS method. As it is shown in section 3.5, thermal techniques can be easily adapted to allow *in-situ* measurements under vacuum (Camacho González *et al.*, 2004; Mellinger *et al.*, 2004b). This way, the sample can remain in the sample holder during the entire experiment.

Acoustical Method

The Piezoelectrically generated Pressure-Step (PPS) method (Gerhard-Multhaupt *et al.*, 1983, 1997). This acoustical method has been used to investigate the space charge and dipole orientation profiles of materials. It gives the possibility to observe the piezoelectric effects caused by dipoles and charges. The sample is compressed by a pressure step and the change in the surface charge density is monitored as a function of time.

To ensure a steep pressure step, a cable discharge generator produces several pulses of 300 V per second, and excites a quartz crystal which generates the pressure steps. These steps are efficiently transmitted to the sample with the help of silicone oil which acoustically couples one side of the sample to the quartz crystal. The variation of volume due to the change of pressure generates a piezoelectric current to make up for the compensation charges in the metallic electrodes. The piezoelectric current is detected and converted into voltage by a 1 GHz preamplifier, which is coupled to the other side of the sample. The signal generated by the preamplifier is monitored by a 1 GHz oscilloscope. A sharp voltage step is used for triggering (fig. 3.5). The resolution of this method ($\approx 2\,\mu m$) depends on the rise times of all participating instruments (voltage step generator, quartz crystal, preamplifier, oscilloscope), the speed of sound inside the sample, and the RC time of the sample circuit.

A schematic representation of a PPS signal is shown in figure 3.6. Whereas a homogeneous dipolar polarization produces a box-shaped signal, stored charges cause different
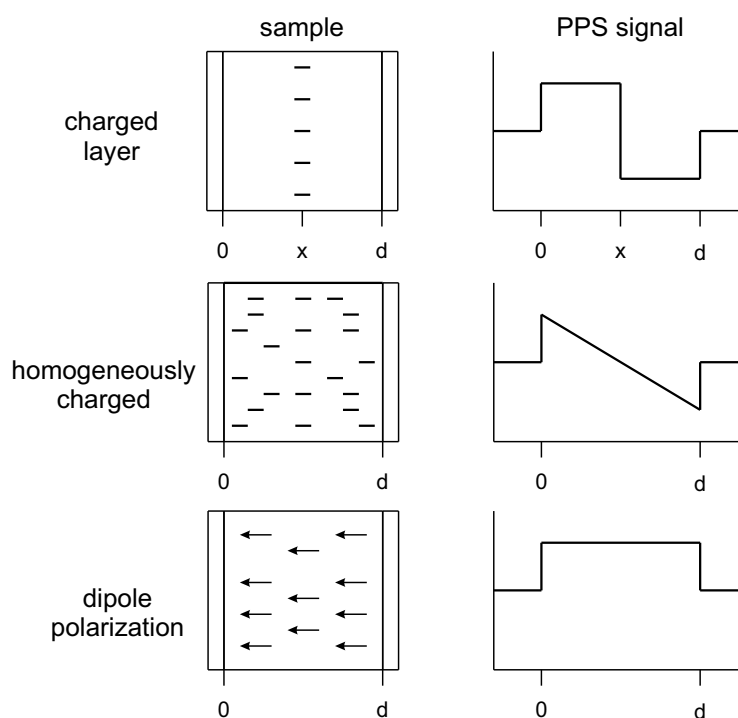
Figure 3.6: Schematic response of a PPS experiment for different charge profiles and dipole polarization.

responses. A charge-layer inside the sample responds with a constant signal until the pressure step has reached it. Then the signal changes the sign and is again constant until the pressure step reaches the rear side of the sample. A homogeneously distributed charge inside the sample generates a step with a subsequent decrease of the signal. In the middle of the sample the signal changes the sign and increases to the start value with opposite sign at the end of the sample, forming a "saw tooth" shape. For both charge effects, the integral of the signal vanishes.

Thermal methods

Thermal techniques can give information about the profiles of stored charge and oriented dipoles. In these techniques, a current which gives information about the trapped charge and the dipole orientation is produced by a thermal stimulus. According to the transient thermal excitation employed, the thermal techniques can be classified into time domain or frequency domain implementations (fig. 3.7). The thermal-pulse and the excitation step methods are classified as time-domain methods, while the thermal-wave method (Laser Intensity Modulation Method) as a frequency-domain method (Bauer and Bauer-Gogonea, 2003).

In this work, the thermal-pulse and the thermal-wave methods were used to determine the charge and dipole profiles. As mentioned before, these methods have the advantage of allowing *in-situ* measurements under vacuum. However, the deconvolution process,
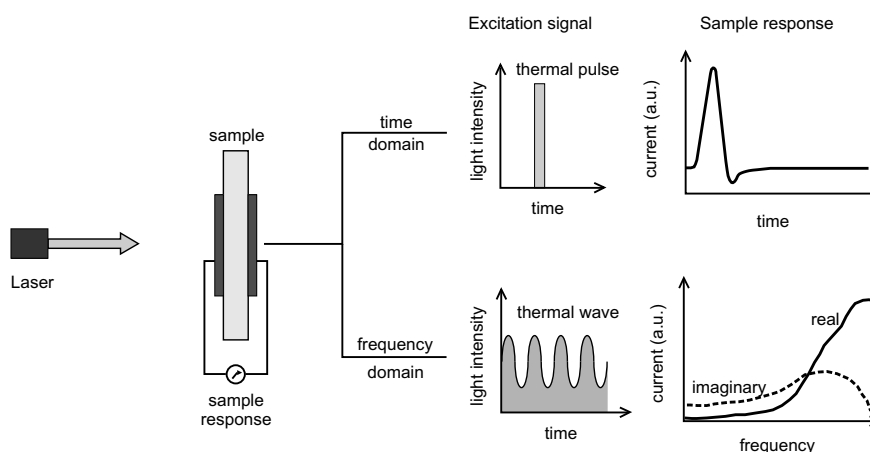
Figure 3.7: Employed thermal depth-profiling methods. Thermal Pulse and thermal wave (Laser Intensity Modulation Method) methods.

which needs a rather careful interpretation of the results, has been a drawback of thermal techniques. Therefore, the data analysis has become an important part to comprehend the space-charge and polarization profiles. Mellinger *et al.* (2005) have shown that a similar amount of information on the space-charge profile can be obtained with both techniques. However, the thermal-pulse technique is preferable to its frequency-domain counterpart in terms of acquisition speed.

Laser Intensity Modulation Method (LIMM) (Lang and Das-Gupta, 1981; Lang, 2004). In LIMM, a thermal wave is generated in the sample when an intensity-modulated laser illuminates an opaque electrode coated on the sample (fig. 3.7). The penetration depth of the thermal wave can be modified with the change of the frequency of the outside temperature oscillation: the faster the oscillation, the smaller the penetration depth. In that way, it is possible to scan along the thickness of the sample. When the polarized polymer is exposed to heat, the sample expands, causing a variation of the charge and dipole density. This leads to a change in the image charge on the electrode which can be measured. The dipole and charge-density profile of the polymer is given by the analysis of the current as a function of frequency (Tikhonov *et al.*, 1987; Lang, 1991; Ploss *et al.*, 1992; Weese, 1992; Bloss *et al.*, 1997; Lang, 2004; Mellinger, 2004b).

Thermal Pulse Method (TP) (Collins, 1976, 1980). In the Thermal Pulse method, a thermal excitation is achieved through the absorption of a short intense light pulse by an opaque electrode coated on the sample (fig. 3.7). The thermal pulse diffuses inside the sample generating a local variation of the charge and dipole density. This leads to a change in the image charge on the electrode which can be measured. The dipole and charge-density profile of the polymer is given by the analysis of the current as a function of time. Alternatively, the current is transformed from the time domain into the frequency domain using the *Fast Fourier Transformation* (FFT). In this way, the analysis can be performed in the frequency domain.

3.3 Materials

3.3.1 Polyethylene Terephthalate

Polyethylene terephthalate (PETP) can be synthesized by condensation polymerization of terephthalic acid with ethylene glycol. Apart from the carboxylic groups ($>\!C = O$), the main chain is totally symmetric (fig. 3.8). Due to the higher electronegativity of oxygen compared to that of carbon, the electron density is shifted towards the oxygen atom. Consequently, the carbonyl group forms a dipole and causes the polar properties of the material.

A more detailed look at the chemical constitution of the repeat unit (r.u.) of PETP (fig. 3.8(a)) shows that the phenyl rings ($-C_6H_4-$) are linked in the 1,4 position to ester groups ($-COO-$). The molecular groups $-OOC-C_6H_4-COO-$ are independent of neighboring r.u. due to the ethylenic linking groups $-CH_2-CH_2-$. Daubeny *et al.* (1954) performed crystallographic analysis on PETP and established that the chain configuration in its crystalline portion is *trans* (fig. 3.8(b)). However, Loew and Sacher (1978) found from potential energy calculation that the *cis* (fig. 3.8(c)) and *trans* forms equally exist in unoriented PETP. Additionally, Ouchi (1983) suggested the existence of the *cis* form of the carbonyl groups in oriented amorphous phases.

The transmission and photo-luminescence spectra of PETP (Mylar®) films are shown in fig. 3.9. Scanning from long to short wavelengths, PETP films (12 µm) have a transmission over 80% which strongly decreases when the light wavelength approaches to 310 nm. Ouchi (1983) and LaFemina and Arjavalingam (1991) report the presence of three absorption peaks at 200, 240 and 300 nm related to the benzene transitions. The peak at 200 nm (6.2 eV) is due to the dipole-allowed $^1A_{1g} \rightarrow\, ^1E_{1u}$ transition. At 240 nm (5.2 eV), the peak is the result from the $^1A_{1g} \rightarrow\, ^1B_{1u}(^1L_a)$ transition. At 300 nm (4.1 eV), the absorption is due to the $^1A_{1g} \rightarrow\, ^1B_{2u}(^1L_b)$ transition. Even though the carbonyl $n - \pi^*$ transition is expected at 300 nm (Williams and Fleming, 1995), LaFemina and Arjavalingam (1991) provide a complete description of the absorption spectrum without considering this transition. However, Takai *et al.* (1977b) concluded that the red shift of the absorption peak assigned to the $\pi - \pi^*$ transitions of the benzene rings is due to the resonance of the π orbitals in the benzene with that of carbonyl groups adjacent to the benzene ring (fig. 3.8).

The photo-luminescence spectrum exhibits three peaks at 385, 650 and 750 nm. Teyssèdre *et al.* (2001) concluded that the spectrum arises from monomeric and ground state dimers emissions. The fluorescence of monomeric-like emission is observed at 335 nm (3.7 eV). The phosphorescence emission glows in several bands in the region 420–480 nm (2.95–2.6 eV). The fluorescence due to the ground state dimer-like emission appears at 385 nm (3.22 eV), while the phosphorescence emission in the region 480–540 nm (2.58–2.3 eV). Since the presence of the peaks at 650 and 750 nm in PETP films were not found in previous studies of PETP (Ouchi *et al.*, 1999; Teyssèdre *et al.*, 2001; Takai *et al.*, 1978a), it is possible that these peaks are caused by additives in Mylar® films.

(a)

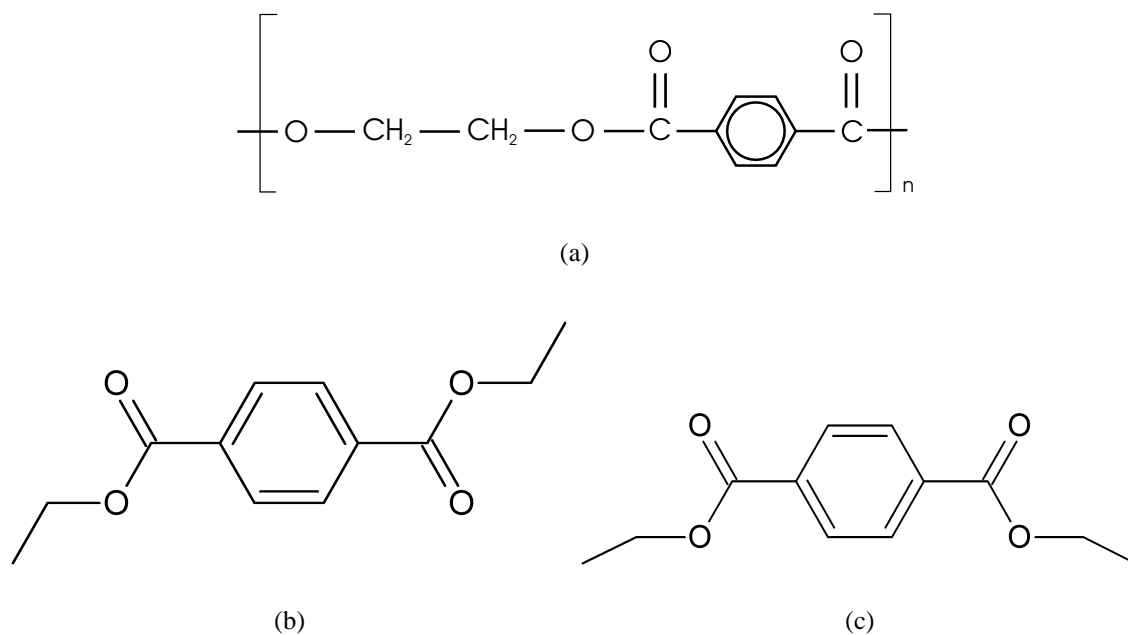(b)   (c)

Figure 3.8: Polyethylene-terephthalate repeat unit (a) and its conformations: *trans* (b) and *cis* (c).
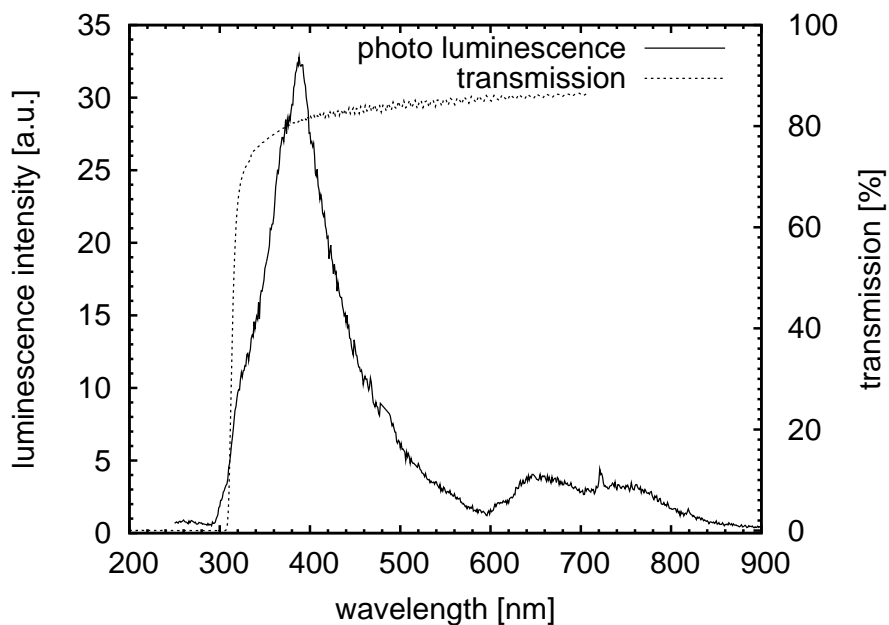

Figure 3.9: Photo-luminescence (excitation at 240 nm) spectrum of a PETP film (23 μm) and transmission spectrum of a PETP film (12 μm).
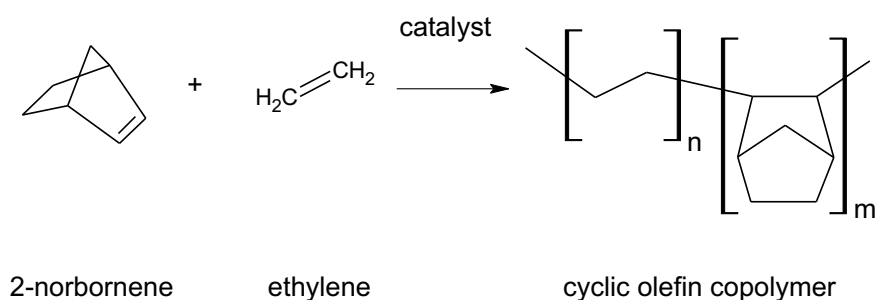
2-norbornene   ethylene   cyclic olefin copolymer

Figure 3.10: Polymerization scheme for cyclic olefin copolymer (COC)

3.3.2   Cyclic Olefin Copolymer

Cyclic olefin copolymers (COC) are synthesized via chain growth polymerization using metallocene catalysts (Kaminsky, 1998). In fig. 3.10, the polymerization scheme of COC shows that 2-norbornene and ethylene are the co-polymerized monomers.

Rische *et al.* (1998) showed the microstructure and the morphology of COC depend upon the content of norbornene in the polymer chain. From these studies, it is possible to infer that the COC employed in this work (TOPAS®8007 and 6013) are copolymers with a norbornene content less than 50 mol %. These kind of COCs consist mainly of both blocks of alternating norbornene/ethylene sequences and polyethylene sequences, with a relatively high stereoregularity.

The absorption spectra of drop-cast COC films from a toluene solution are shown in fig. 3.11. As it can be observed, COC films present absorbance for $\lambda < 230$ nm. From the chemical structure, the chromophores present in this polymer are the $\sigma-$bonded electrons from the C$-$C and C$-$H bonds with a $\sigma - \sigma^*$ transition at $\lambda_{\mathrm{max}} \approx 150$ nm (Williams and Fleming, 1995). Drop-cast COC films were also doped. At larger wavelengths, the absorption is due to the dopants in the COC matrix. A broad absorption peak (350–500 nm) is observed in samples doped with 4-dimethylamino-4'-nitrostilbene DANS (Ehara *et al.*, 2000). Samples doped with Pyrene show the characteristic absorption peaks of this dye (Berlman, 1971).

3.4   Sample preparation

The samples employed were films supplied by a manufacturer or films casted or coated on substrates. The samples were charged by means of *corona discharge* method or *contacting electrodes* method. By varying the charging temperature, it was possible to selectively produce either a surface or a bulk charge (Sessler, 1999c). Evaporated electrodes on the samples are required to avoid gaps between the electrode and the sample surface and to assure a good electrical and thermal contact. The evaporated electrodes are needed for
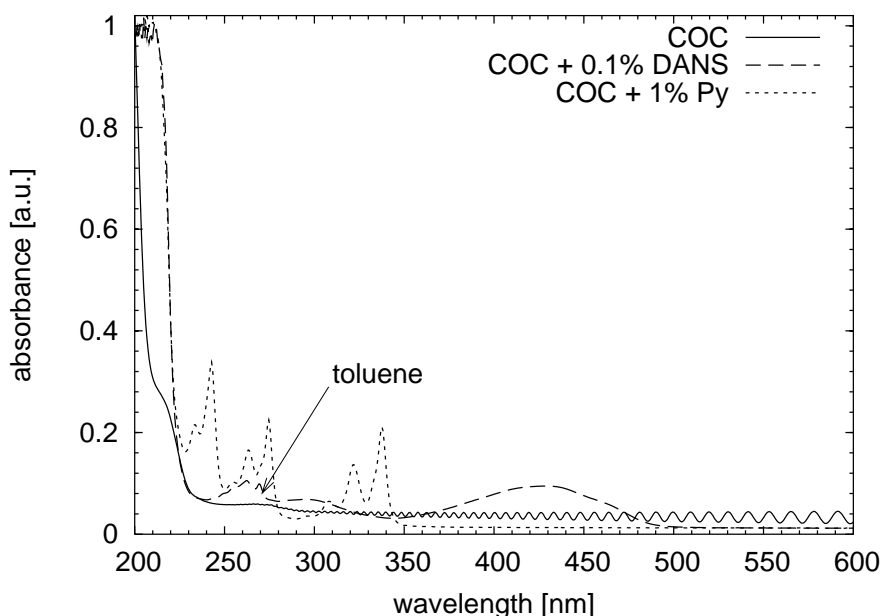
Figure 3.11: Absorption spectrum of drop-cast COC films from toluene solution. Un-doped, and doped with 0.1% DANS or 1% Pyrene (Py) in COC matrix. The characteristic absorption peaks of the dyes can be observed at 240, 270 and 330 nm for Py, and 300 and 430 nm for DANS. COC matrix absorption is present at $\lambda < 230$ nm. The absorption peaks of traces of toluene in poorly annealed samples are marked in the graph.
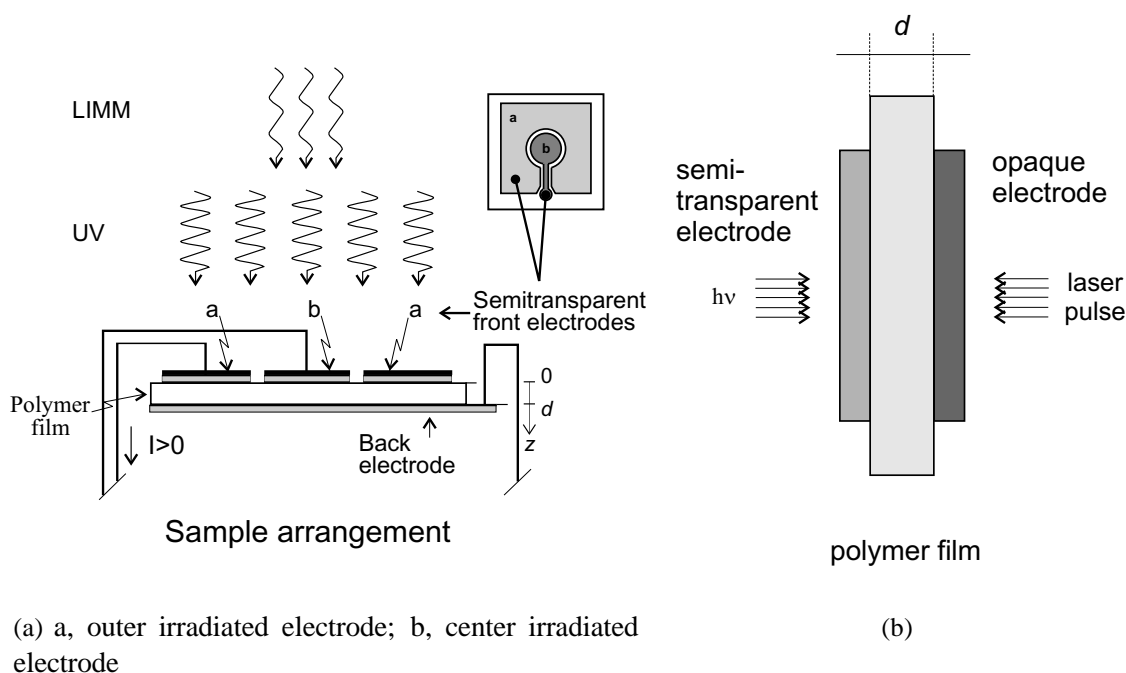

(a) a, outer irradiated electrode; b, center irradiated electrode

(b)

Figure 3.12: Sample arrangement when the charge profile is determined with LIMM **(a)** and with TP method **(b)**. d, thickness of the sample.
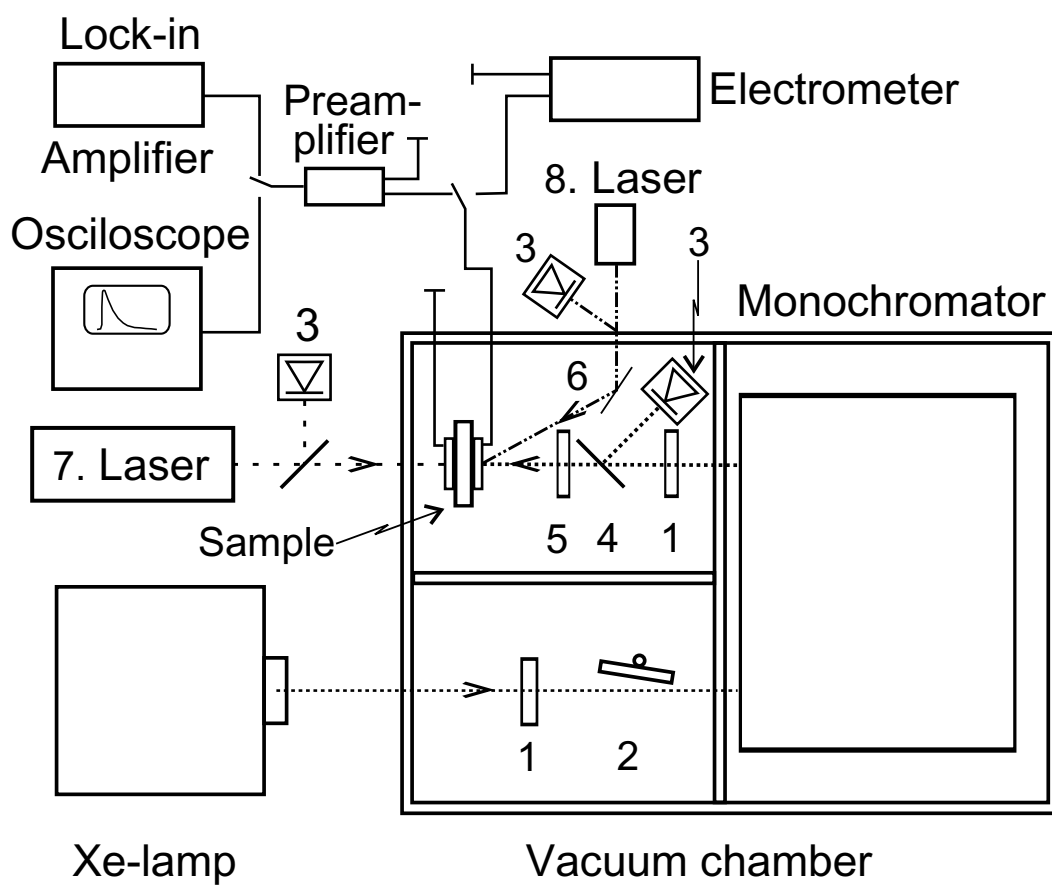
Figure 3.13: Experimental setup for measuring the photo-stimulated discharge and the charge distribution with LIMM and TP. 1. Lens, 2. shutter, 3. photodetector, 4. beam splitter, 5. iris, 6. mirror, 7. laser for TP technique, and 8. laser for LIMM technique.

TSD, LIMM, and PSD. In addition, the electrodes should be semitransparent for PSD. To perform a single TL, only one electrode is required.

Samples of polyethylene terephthalate (Mylar® brand, DuPont Teijin Films, $d = 23$ μm) were rinsed with methanol and coated with semi-transparent Cu or Au electrodes (≈ 12 nm thick). An extra carbon layer (≈ 10 nm thick) was evaporated onto the front electrode. This coating was sufficiently transparent to UV light while at the same time providing the necessary absorption for measuring space charge profiles via LIMM. For current measurements both parts ("a" and "b" in fig. 3.12(a)) were connected to the electrometer. In order to minimize the capacitance, only the central spot ("b", diameter 5 mm) was used in LIMM experiments. The sample was glued to a stainless steel substrate in order to assure a good thermal contact. These samples were charged by contacting electrodes and light irradiation.

COC polymer resin (TOPAS® 6013 and 8007, Ticona GmbH) was dissolved in toluene or chloroform and drop-cast onto either stainless steel (for TSD measurements) or fused silica substrates (for PSD measurements). The concentration of 0.1% weight 4-dimethylamino-4'-nitrostilbene (DANS) or 1% weight pyrene in COC solution was used to produce chromophore-doped films. The samples were dried in a nearly saturated solvent atmosphere and annealed above the glass transition temperature for at least 15 h. The samples were charged in a point-to-plane corona discharge and coated with conductive metal electrodes (Ag, Al or Cu) in high vacuum. The 6013 material was charged under N_2 atmosphere to avoid oxidation. The 8007 material was charged in presence of air. Since COC polymer is transparent to UV light (sec. 3.3.2), the UV light can be directed onto the semitransparent electrode and penetrate the sample up to the opaque electrode, where the laser pulse can be directed on the other side (fig. 3.12(b)).

3.5 Experimental setup

PSD measurements were carried out in vacuum (fig. 3.13). The monochromatic light was generated by a 450 W Xe arc lamp (Oriel) and a monochromator (Photon Technology International) equipped with an UV-enhanced grating (blaze angle for 250 nm) and a variable bandwidth with a smallest range of ± 2 nm. The light intensity was monitored with a UV-sensitive photodiode (Hamamatsu S8551), via a calcium fluoride beam splitter.

The space-charge and dipole orientation profiles of the samples were determined *in situ* with either the LIMM or the TP technique. In the LIMM technique, the light from an intensity-modulated diode laser is used as a thermal source. The current that results in the presence of space charge or oriented dipoles was detected with a current-to-voltage converter (Femto LCA-200K-20M) and a Lock-in Amplifier (Stanford SR850).

Thermal pulse measurements were performed with the second harmonic output (wavelength 532 nm, pulse duration $\tau_L \approx 5$ ns) of a Nd:YAG laser (Polaris III, New Wave Research). The short-circuit pyroelectric current was amplified by a current amplifier (Stanford Research SR 570) and recorded with a digital storage oscilloscope (Agilent 54833A) at a rate of $(\Delta t)^{-1} = 10$ MSamples/s. According to Nyquist's theorem, this

allows frequencies up to 5 MHz to be recorded, so that the bandwidth (and hence the spatial resolution) is limited by the high-frequency cut-off of the current amplifier, rather than the rate of digitization. After averaging between 30 and 256 laser pulses, a total of $N = 512\,000$ data points were stored for further processing.

The distribution function of the LIMM and TP measurements $g(z)$ was reconstructed from the measured current using an iterative approach proposed by Mellinger *et al.* (2003). A brief description of this technique is given in section 4.1.3.

3.6 Procedure of poling and charging

3.6.1 Polyethylene Terephthalate

Figure 3.14 shows the charging, poling and discharging processes for PETP samples. Initially, the sample was heated up to 110 °C in order to drain any charge generated by previous processing steps. To generate mainly charge carriers in the sample (fig. 3.14(a)), the sample was driven to one of several temperatures of charging T_c (-100, -50, -25, 0, and 25 °C). The samples were charged using contacting electrodes. A negative voltage (-600 V) was applied to the back electrode, while the polymer film was simultaneously irradiated with UV-light at $\lambda = 305$ nm during 30 min. The orientation of dipoles was also possible when the charging process was performed at higher temperatures. The electric field was applied when the sample was set at 110 °C. The electric field was kept on until the sample was cooled down to room temperature (fig. 3.14(b)).

The space-charge and dipole profiles of freshly charged films were determined *in situ* by means of the LIMM technique. After determining the charge and dipole profile and recording a PSD spectrum, the sample was irradiated for 30 min with monochromatic light at the wavelengths corresponding to the peaks in the PSD spectrum. During the current decay, the short-circuit discharge current was measured. Finally, the charge and dipole profile was determined to obtain information about the charge detrapping, since the dipole orientation is not affected after light irradiation in PETP.

3.6.2 Cyclic olefin copolymer

The procedure of experiments performed on COC is depicted in fig. 3.15. These samples were charged with a point-to-plane geometry of the corona discharge method at their glass transition temperatures T_g. There was a 4 cm gap between the needle and the plate. The needle voltage applied was about 10 kV for 3 minutes. After charged, the samples were coated with an opaque electrode. The charge profile of a freshly charged sample was monitored every ten minutes during the dark current decay for one hour with the help of the TP method. After performing a PSD-spectrum, the charge profile of the sample was determined. During two hours of PSD-decay with monochromatic light, the charge profile was *in situ* monitored. The wavelengths of the monochromatic light for PSD-decay were selected according to the peaks in the PSD-spectrum. Finally, the charge profile was determined to obtain information of the charge detrapping.
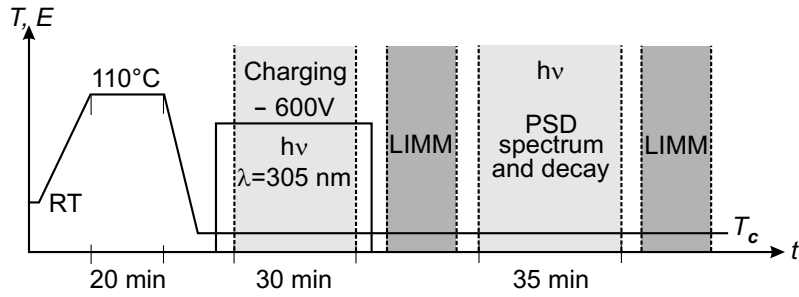
(a)
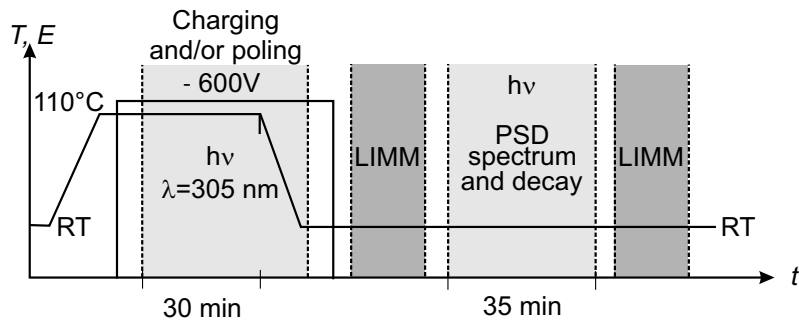
(b)

Figure 3.14: Experimental procedure for (a) charge carrier generation and (b) dipole orientation and charge carrier generation at 110 °C in PETP. T: temperature; E: electric field; RT: room temperature; T_c: charging temperature ($-100, -50, -25, 0, 25$ °C).
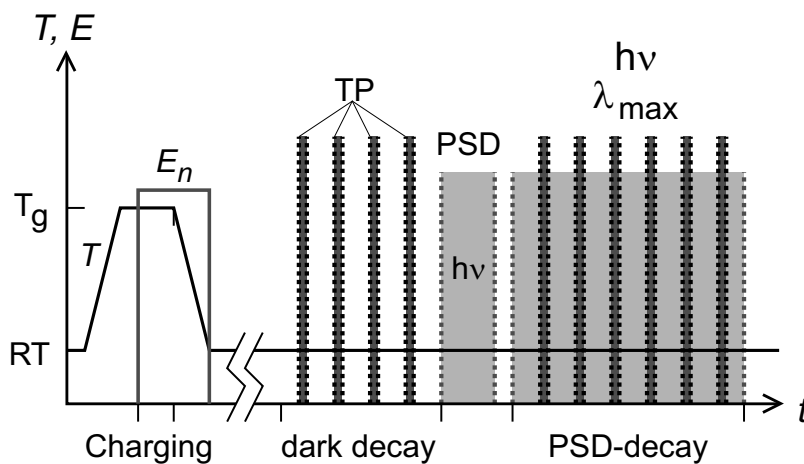

Figure 3.15: Experimental procedure performed on COC. E: electric field, T: temperature, RT: room temperature, T_g: the glass transition temperature. TP: thermal pulse. E_n: electric field applied by the needle of the corona setup.

Chapter 4

Results and discussion

4.1 Polyethylene Terephthalate

4.1.1 Dielectric spectroscopy

Dielectric spectroscopy measurements were performed on PETP films (Mylar®, Dupont Teijin) to estimate the degree of crystallinity (χ). The dielectric spectra are shown in the figures 4.1 and 4.2 for the permittivity (ε') and losses (ε''), respectively. In these spectra the known α- and β-relaxations appear between temperatures from -75 to 20 °C and from 95 to 140 °C, respectively. A slight change of the slope is also present in the ε' between 50 and 95 °C. In fig. 4.3 this region is shown where the sampling rate becomes higher. The fact that PETP with low degree of crystallinity (≈ 0.05) exhibits an α-relaxation between 80 to 100 °C (Coburn and Boyd, 1986; Ishida *et al.*, 1962) and the glass transition temperature of PETP at $T_g = 79$ °C (Menczel *et al.*, 1997; Menard, 1999) indicate that the behavior of the dielectric spectroscopy in this temperature range is due to the amorphous regions of the PETP film.

Dielectric studies performed on PETP (Reddish, 1950; Ishida *et al.*, 1962; Coburn and Boyd, 1986; McCrum *et al.*, 1991) showed differences on the spectra of samples with different degrees of crystallinity. It was found that the frequency-temperature location and shape of β-peak (ε'') relaxations were independent of the degree of crystallinity. However, the magnitude of the β-peak (ε'') decreases as the degree of crystallinity increases.

Contrary to the β-relaxation, not only the magnitude of the α-relaxation peak (ε'') decreases, but also the shape and the frequency-temperature location change. It was found that the α-relaxation at a given frequency shifts to higher temperatures and the magnitude of the peak decreases as the crystallinity increases. Ishida *et al.* (1962) showed that the normalized α-relaxation peak broadens to lower frequencies as the crystallinity increases.

Table 4.1 shows the position and the magnitude of the α- and β-relaxation peaks for different degrees of crystallinity (χ). These values were taken from Ishida *et al.* (1962) and Coburn and Boyd (1986). The values obtained from our samples (Mylar®) are also included in the table. An extrapolation of the data obtained from Ishida *et al.* (1962)

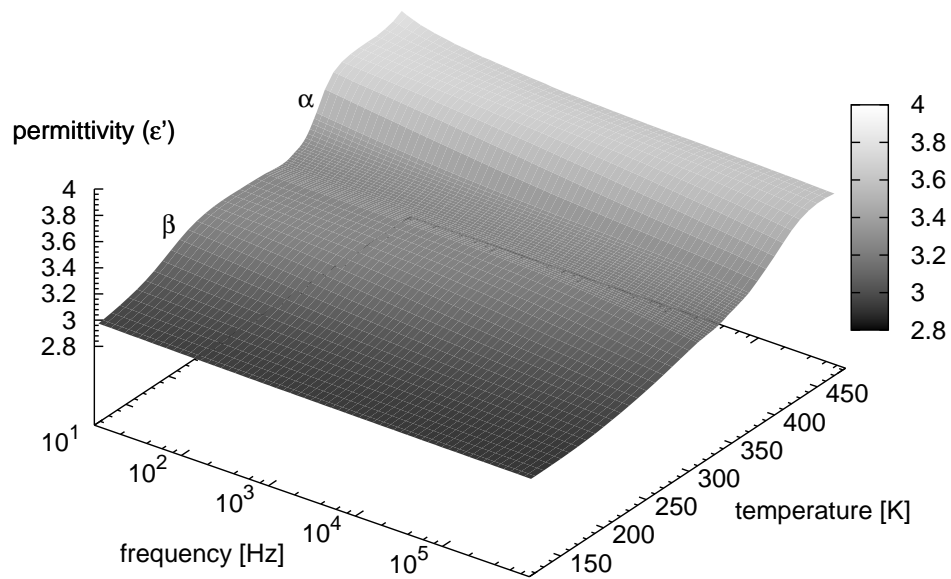Figure 4.1: Dielectric spectrum (ε') of a PETP film. α and β indicate the respective relaxation processes.

Figure 4.2: Dielectric spectrum (ε'') of a PETP film. α and β indicate the respective relaxation processes.
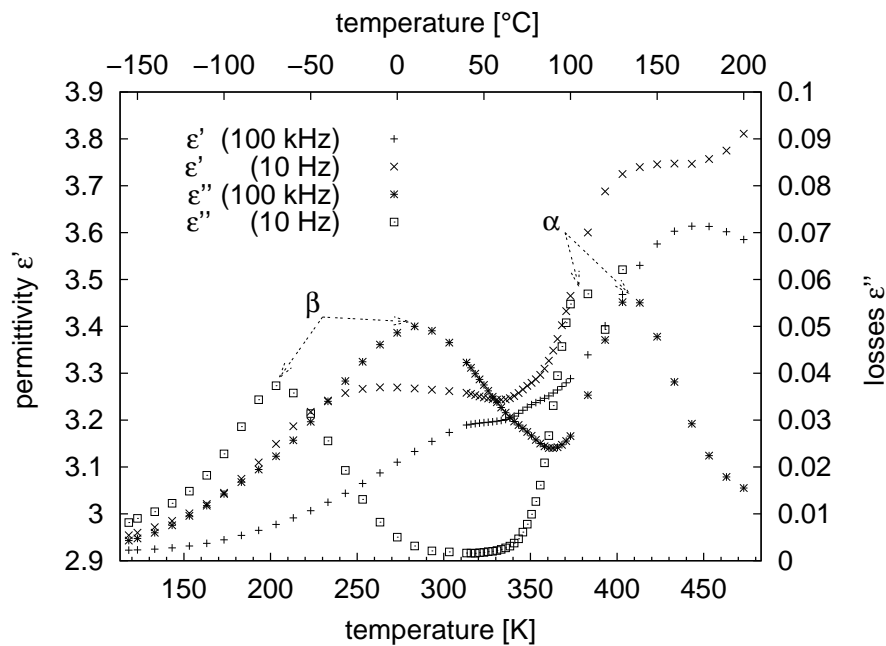
Figure 4.3: Dielectric spectrum of a PETP film for two selected frequencies.

and Coburn and Boyd (1986) indicates that our samples have a degree of crystallinity of approx. 0.55 ± 0.05.

The identification of the chemical groups resposible for the dielectric relaxations in PETP were already identified. Menczel *et al.* (1997) summarize that the α-relaxation of PETP corresponds to its glass transition and the β-relaxation seems to be resolved into three or four subrelaxations. These subrelaxations are related to hindered rotation of the methylene groups, *gauche-trans* configurations of the chains and crystalline relaxations related to crystal imperfections. Reddish (1950) suggested that the β-relaxation was due to the orientation of the hydroxyl-groups (HO–) and Ishida *et al.* (1962) considered that this process is one of local motions of the chain involving the ester-groups (–COO–).

4.1.2 Thermally-stimulated currents and thermoluminescence

Thermally-stimulated current (TSC) experiments were performed on PETP films from -180 to 130 °C with a heating rate of 3 K/min. Figure 4.4 shows thermo-stimulated polarization (TSP) thermograms performed by applying different electric fields; $E = 5$, 10, 15, 20 and 25 V/µm. As expected, the current increases with the increment of the electric field. The thermograms show the presence of three peaks. A broad peak appears from -180 to -25 °C. A second one, overlapped on the first peak, appears from -100 to -50 °C which broadens to lower temperatures and merges with the first peak when the electric field is larger. The third peak appears from -50 to 0 °C, with an electric field threshold of 10 V/µm.

Table 4.1: Dielectric α- and β-relaxation peaks (ε'') of PETP for different degrees of crystallinity (χ).

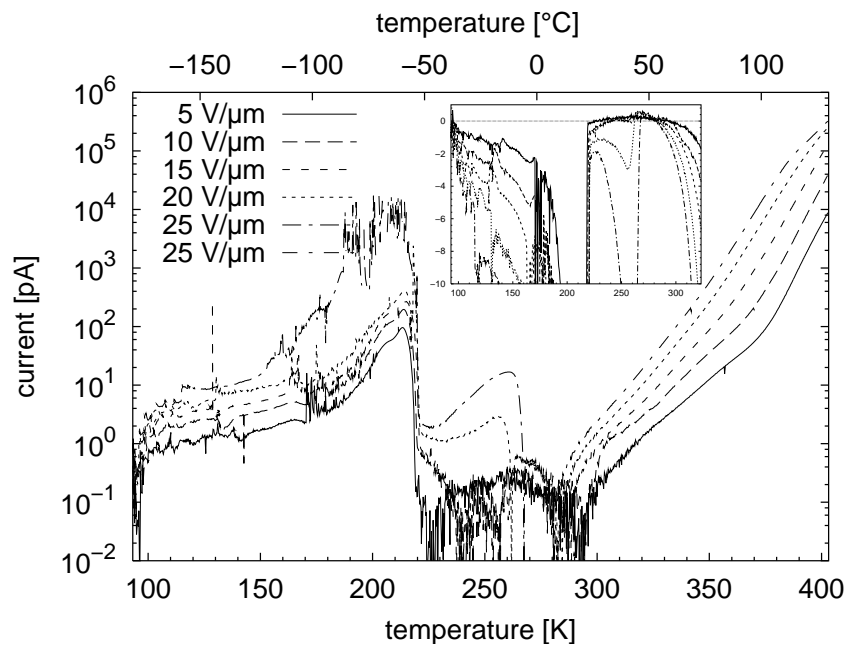| | Relaxation [Hz] | Ishida *et al.* (1962) | | | | Coburn and Boyd (1986) | | | | | | Fig. 4.3 | |
| | | $\chi = 0.05$ | | $\chi = 0.51$ | | $\chi = 0.04$ | | $\chi = 0.38$ | | $\chi = 0.5$ | | | |
		Temp. [°C]	ε''	Temp. [°C]	ε''	Temp. [°C]	ε''	Temp. [°C]	ε''	Temp. [°C]	ε''	Temp. [°C]	ε''
α	10	85	0.4	95	0.07	84	0.45	95	0.087	93	0.07	100	0.058
	10^5	-	-	-	-	100	0.27	122	0.08	122	0.075	135	0.055
β	10	-70	0.053	-	-	-70	0.07	-70	0.039	-70	0.04	-70	0.036
	10^5	-	-	11	0.052	10	0.1	10	0.057	10	0.055	10	0.05

Figure 4.4: TSP-thermograms of a PETP film (23 µm). Heating rate = 3 K/min with E = 5, 10, 20 and 25 V/µm. The inset shows the raw measurement of the current to indicate the polarity of the current peaks.

A monotonic increase of the current appears with a temperature threshold from 10 to 27 °C. As it can be observed, the threshold temperature depends on the electric field; the larger the electric field the lower the temperature threshold.

As explained in section 3.2.1, the dipole and charge effect are merged in the signal. McKeever and Hughes (1975) proposed a method to discern between charge carrier processes and dipole orientation. The experimental sequence is depicted in fig. 3.4. A metal-coated sample was heated up to 130 °C for 2 h and cooled to room temperature (RT) with a cooling rate of 10 K/min in vacuum. The sample was driven to −180 °C with a cooling rate of 10 K/min and irradiated with monochromatic light at 300 nm for 10 min, under applied electric field. After 20 min and the voltage still on, a TSC was performed with an applied electric field of $E = 20$ V/µm and a heating rate of 3 K/min.

The TSPC and TSC thermograms are shown in fig. 4.5. The sample was heated for 2 h at 130 °C and cooled down to −180 °C, at 10 K/min. TSPC was performed from −180 to 130 °C, $E = -460$ V, 3 K/min. The sample was kept at 130 °C for 1 h and cooled down to −180 °C without switching the voltage off. At this point, it is considered that the dipoles were already oriented.

A second TSC was performed with the same heating rate. Since the dipoles were already oriented, this TSC is considered to be the "zero"-TSC. In this thermogram, the effect of thermal expansion of the sample together with the thermally activated d.c. conductivity appear in a single signal.
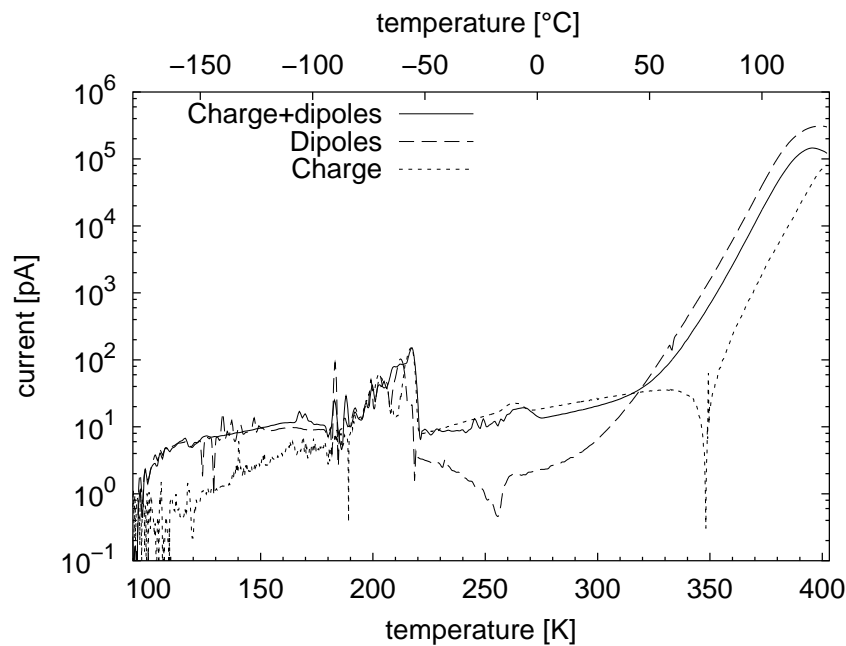
Figure 4.5: TSP, TSPC and TSC-thermograms of a PETP film ($d = 23$ µm). Heating rate = 3 K/min with $E = 20$ V/µm (see sec. 3.2.1).

The sample was kept for 1 h at 130 °C and cooled down to -180 °C with the same cooling rate (10 K/min). At -180 °C, the sample was irradiated with UV light at 300 nm for 10 min. After 20 min, a third TSC (TSC3) was performed. In this case, the effect of charge carriers generated at low temperatures is mainly observed.

In order to remove the thermal expansion effect of the sample, the zero-TSC is subtracted from the TSC1, TSPC and TSC3 thermograms. Fig. 4.5 shows the discrimination of the charge carrier from dipole signals. As it can be observed, the peak from -180 to -25 °C is mainly due to dipole orientation. The peak at 0 °C is related to charge carriers. The peak from -100 to -50 °C is a result of the combined signal of charge carriers and dipole orientation. The monotonic increase of the current at 10 °C is mainly due to the dipole orientation. This increases reaching a maximum at 120 °C.

Former experiments describe the thermal activated processes behind our experimental result shown in fig. 4.5. Takai *et al.* (1978c) and Frübing *et al.* (1980) observed a β-peak around -100 °C and attributed the peak to the ester-groups (–COO–). This peak yielded an activation energy of $0.23-0.5$ eV (Takai *et al.*, 1978c). In samples irradiated with UV-light, a current peak is also observed at 0 °C, which is attributed to charge carriers (Frübing *et al.*, 1980). At higher temperatures ($T \approx 100$ °C), a peak has been observed (Creswell and Perlman, 1970; Frübing *et al.*, 1980; Hesse, 1999) and is related to the movement of the chain segments (Frübing *et al.*, 1980).

It is not possible apply the method proposed by McKeever and Hughes (1975) when the temperature in the TSP increases beyond 150 °C for PETP. Thielen *et al.* (1994, 1997) have shown an increase of the degree of crystallinity due to the heat treatment, leading
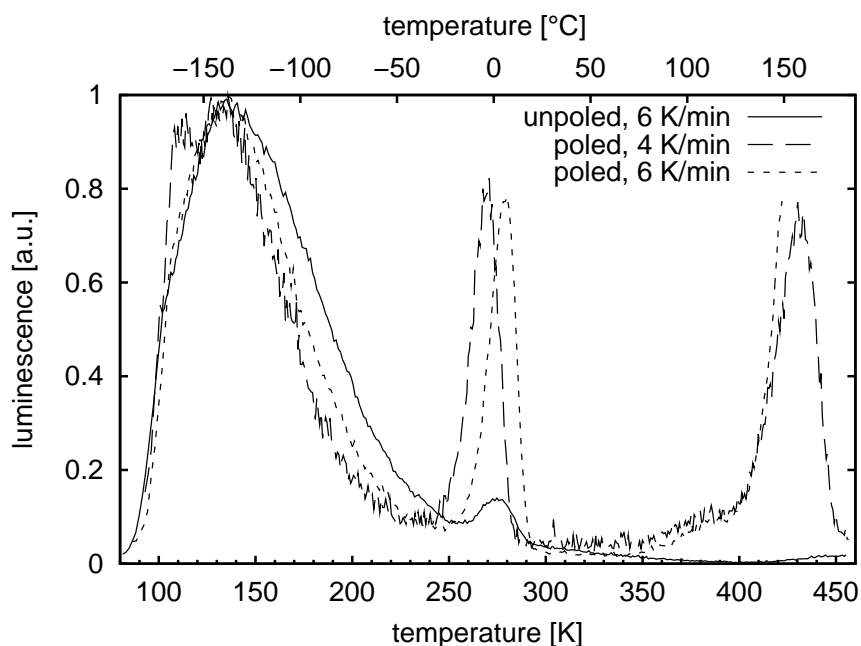
Figure 4.6: TL-thermograms of a PETP film ($d = 23\,\mu m$), normalized at $-135\,°C$ (133 K).

to strong differences in the charging currents and TSD-thermograms. This can be explained by the "cold crystallization" process which appears in PETP with a maximum at 135 °C (Menard, 1999). This process gives a reorganization of the molecular structure of the polymer.

Thermoluminescence (TL) measurements were performed on poled and unpoled PETP films. The samples were uncoated films. The poling process was performed using the contacting electrode method in a N_2 environment, with V=600 V at 110 °C. The samples were cooled to -180 °C and irradiated with broad-band light generated by a 450 W Xe-lamp equipped with a BG 3/2 filter (transmission range: 300-520 nm). The TL-thermograms normalized at -135 °C are shown in fig. 4.6. They show four peaks at -140, 0, 110 and 160 °C for charged samples. Uncharged samples exhibit only the first two peaks, at -140 and 0 °C. The electric field inside the sample is mainly due to dipole orientation (fig. 4.7). Using the PPS-technique, the electric field was calculated to be $E = D/(\varepsilon_0\varepsilon) \approx 4$ V/µm.

The comparison of TL-thermograms from unpoled and poled samples at low temperatures shows a change in the shape of peaks. The FWHM (Full Width Half Maximum) of the peak at -135 °C is 74.6 °C for a charged sample, while the uncharged one shows a FWHM of 87.5 °C. Also, the relative size relation from the second peak to the first one changes. This peak is larger in charged samples than in uncharged samples. The difference of the TL-thermograms at low temperatures from unpoled and poled samples agrees with the results reported by Takai *et al.* (1978b). The authors concluded that an external electric field enhance the charge carrier generation avoiding the exciton recombination. They also gave an estimate of 4 to 5 nm of the charge-pair separation, using Onsager's theory (Onsager, 1938).
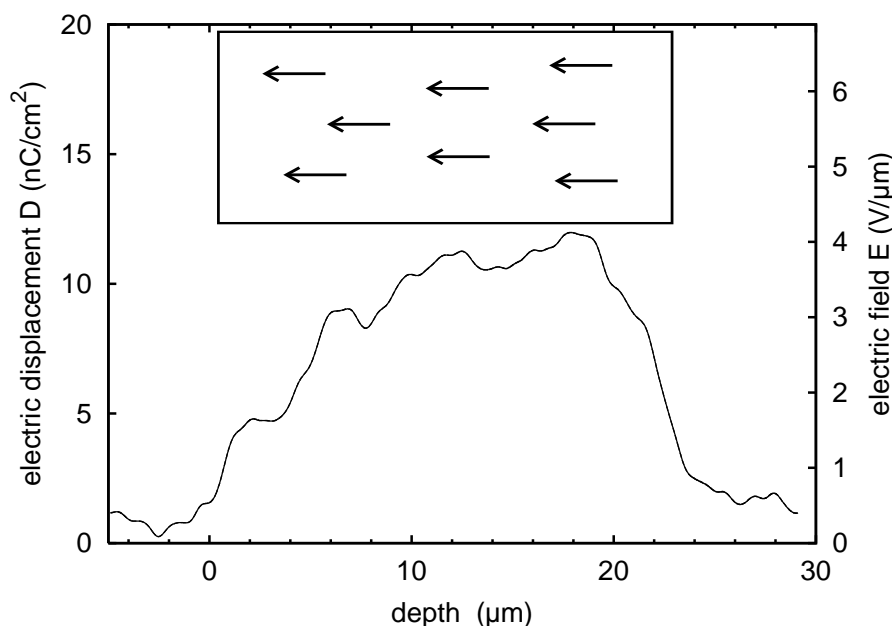
Figure 4.7: PPS measurement and internal electric field of a PETP film ($d = 23$ μm) charged at 110 °C, $V = 600$ V without light irradiation. The inset shows the poling profile.

The spectrum analysis of the light-emitted during the TL at low temperatures ($T < RT$) performed by Padhye and Tamhane (1978) and Takai *et al.* (1978c) showed a broad wavelength band from 300 to 600 nm. According to the photoluminescence spectrum of PETP (fig. 3.9), such a wide spectrum is expected. Part of the emitted light can be re-absorbed by the sample and generate free carriers with the help of the electric field. An estimate of 10 nm for 70% probability charge-pair separation was calculated using eqn. (2.6). This distance was calculated with an electric field of 4 MV/m at 0 °C (Camacho González *et al.*, 2002). These carriers can undergo to radiative recombination when the temperature increase giving rise to a strong difference of the peaks at 0 °C.

During TL-experiment, charge carriers are generated due to the re-absorption of the polymer and the internal electric field. At higher temperatures, these carriers and some others which were generated during the light-irradiation at low temperatures recombine. This recombination is eased by the molecular movements of the polymer. The rise of the TL-signal has a threshold of 77 °C (≈ 350 K) which agrees with the T_g contribution of the amorphous region. The peak at 160 °C (≈ 430 K) coincides with the α-relaxation observed in dielectric spectroscopy (sec. 4.1.1).

4.1.3   Determination of the internal electric field

In situ charge and dipole profile measurements were performed with the photo-stimulated discharge (PSD) method in order to prove the charge detrapping. The internal electric field can be built up from charge storage or dipole orientation. However, the change in

the electric field provoked by a PSD-decay is due to the charge detrapping, rather than to dipole orientation. The electric field in the sample can be calculated using techniques which determine the charge and polarization profile. From the LIMM theory (Lang and Das-Gupta, 1981), the current due to the thermal excitation $T(k,z)$, in the presence of a polarization or space-charge, is expressed by

$$I(\omega) = \frac{i\omega A}{d} \int_0^d g(z)T(k,z)dz, \tag{4.1}$$

where A is the area of the electrode and d is the sample thickness. The distribution function is given by

$$g(z) = (\alpha_\varepsilon - \alpha_z)\varepsilon_0\varepsilon E(z) + p(z), \tag{4.2}$$

where $E(z)$ is the electric field, $p(z)$ is the pyroelectric coefficient, α_ε is the temperature coefficient of the permittivity, α_z is the thermal expansion coefficient.

The electric field in the sample can be determined from the distribution function $g(z)$. Solving for $E(z)$

$$E(z) = \frac{1}{\varepsilon_0\varepsilon(\alpha_\varepsilon - \alpha_z)}(g(z) - p(z)). \tag{4.3}$$

In the following subsections, the calibration of LIMM technique is described and with that the procedure to determine $g(z)$ and $p(z)$. In our study, the pyroelectric coefficient was approximated by the quasi-static pyroelectric coefficient as a first approximation. The quasi-static pyroelectric coefficient is considered as a constant.

4.1.4   Temperature function $T(z,t)$ and calibration procedure

The use of LIMM implies a periodic heating of the sample. The propagation of the thermal wave in the sample is described by the heat conduction equation

$$D\frac{\partial^2 T(z,t)}{\partial z^2} = \frac{\partial T(z,t)}{\partial t}, \tag{4.4}$$

where $T(z,t)$ is the temperature and D is the thermal diffusivity of the material. An analysis of one dimension is usually enough for thin samples (Emmerich *et al.*, 1992; Lang, 2001). Since the evaporated electrodes are three orders of magnitude thinner than the polymer film, just the polymer film itself can be considered in the analysis. The boundary conditions of the heat conduction eqn. (4.4) are given by

$$\eta j_\backsim \exp[i\omega t] - G_0 T = -\kappa \left.\frac{\partial T}{\partial z}\right|_{z=0} \quad \text{and} \quad G_d T = \kappa \left.\frac{\partial T}{\partial z}\right|_{z=d}, \tag{4.5}$$

where G_0 and G_d are the heat loss coefficients at the irradiated and non-irradiated surface, κ is the thermal conductivity of the sample, η is the absorptance of the electrode, and

$j_\backsim \exp[i\omega t]$ is the power per unit area irradiated on the electrode ($z = 0$), with a modulation frequency ω. G_0 and G_d can usually be neglected for a free-standing sample, while a substantial heat loss G_d is present on samples with a good thermal contact with a substrate. Under these conditions, eqn. (4.4) is solved by Ploss *et al.* (1991) and Bloss and Schäfer (1994)

$$T(z,t) = T_\backsim(k,z)\exp[i\omega t] = \frac{\eta j_\backsim}{\kappa k} \frac{\cosh[k(d-z)] + \frac{G_d}{\kappa k}\sinh[k(d-z)]}{(1 + \frac{G_0 G_d}{\kappa^2 k^2})\sinh[kd] + \frac{G_0 + G_d}{\kappa k}\cosh[kd]}, \qquad (4.6)$$

where the complex thermal wave vector is given by

$$k = (1+i)\sqrt{\frac{\omega}{2D}}.$$

Calibration procedure

Laser energy absorbed by the sample (z = 0)

The modulated laser intensity ($\iota = jA$), irradiated onto the electrode of area A, is composed of a constant component ($\iota_0 = j_0 A$) and an oscillating one ($\iota_\backsim \exp[i\omega t] = A j_\backsim \exp[i\omega t]$) with an angular frequency ω

$$\iota = (\iota_0 + \iota_\backsim \exp[i\omega t]) \qquad (4.7)$$

A fraction η of the laser light irradiated onto the sample is absorbed by the electrode and converted into heat. The laser employed in our set-up has an output energy of 50 mW. For our experiments, a modulation depth of 56.6% was employed. In this way, the intensity of the laser is given by $\iota = (25 + 14\exp[i\omega t])$ mW. The pyroelectric response of the sample is generated by the oscillatory part of the laser beam.

An evaporated layer (20 nm) of copper or gold onto the sample and an extra layer (12 nm) of graphite on the top were employed as electrode. It is assumed that the laser is partially absorbed by the carbon layer and the transmitted light is completely reflected at the interface of the carbon and copper (or gold). Also, this reflected light is partially absorbed by the graphite layer. The absorbed light by the graphite layer can be determined using the *absorption law*

$$\frac{\iota}{\iota_0} = \exp[-\alpha(\lambda)z], \qquad (4.8)$$

where $\alpha(\lambda)$ is the absorption coefficient at the wavelength λ, z is the path of the light, ι is the light intensity after crossing the electrode, and ι_0 is the intensity of the incoming light. At the laser wavelength, $\lambda = 785$ nm, carbon has an absorption $\alpha(\lambda)$ of 1.7318×10^7 1/m (Besold *et al.*, 1997). The substitution of these values into eqn. (4.8) yields an average of $\eta \approx 0.34$ of the total incoming light. This part of the laser beam is absorbed by the electrode and converted into heat. This value considers the incident light onto the electrode and the reflected light from the metal-carbon interface. Therefore, the energy of the laser transmitted into the sample as heat is

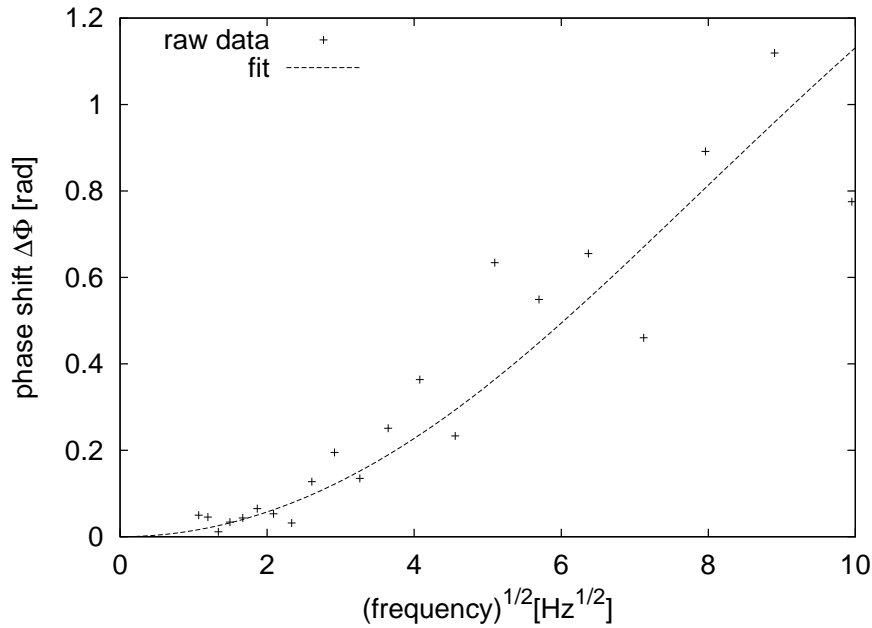$$\eta\iota = (8.5 + 4.8\exp[i\omega t]) \text{ mW}. \qquad (4.9)$$

Figure 4.8: Temperature phase shift between the front and rear surface for PETP films (Mylar®). The diffusivity calculated by fitting the eqn. (4.12) with the *least squares* method is $D = (1.159 \pm 0.092) \times 10^{-7} \mathrm{m}^2/\mathrm{s}$.

Light transmission experiments on PETP show a transmission larger than 80 % for $\lambda > 400$ nm (fig. 3.9). If the laser is transmitted through the front electrode ($z = 0$) and through the sample to the back electrode ($z = d$), the laser intensity would not be strongly affected by the polymer, approx. 3 %, due to the low absorbance. Since the back electrode has a good thermal contact with the substrate, the heat generated by the laser on this electrode sinks into the substrate.

Thermal diffusivity of the PETP film

A technique described by Bauer and Ploss (1990) was employed to determine the thermal diffusivity (D) of PETP films. The sample is prepared evaporating bolometric electrodes on both sides of the film. The absorption of the intensity-modulated laser beam at the electrode causes a temperature oscillation in the free-standing film which is measured with the bolometric electrodes at the front and rear surface. The analysis of the phase shift $\Delta\Phi$ of the temperature oscillations from the front and rear surfaces of the sample can give the thermal diffusivity of the film

$$\Delta\Phi(f) = \frac{\Im[T_\sim(k, z = 0)/T_\sim(k, z = d)]}{\Re[T_\sim(k, z = 0)/T_\sim(k, z = d)]}. \tag{4.10}$$

The solution of the one-dimensional heat conduction equation and the neglect of the losses, eqn. (4.10) yields a frequency-dependent phase shift $\Delta\Phi(f)$ given by (Bauer and Ploss, 1990)

$$\Delta\Phi(f) = \arg[\cosh(kd)], \tag{4.11}$$

with

$$k = (1+i)\sqrt{\frac{\pi f}{D}}.$$

Expanding eqn. (4.11), $\Delta\Phi(f)$ can be also be expressed as (Mellinger *et al.*, 2004b)

$$\tan(\Delta\Phi(f)) = \tanh\left(d\sqrt{\frac{\pi f}{D}}\right)\tan\left(d\sqrt{\frac{\pi f}{D}}\right). \tag{4.12}$$

The fit of the eqn. (4.12) with the *least squares* method to the measured phase shifts yields the diffusivity $D = (1.159 \pm 0.092) \times 10^{-7} m^2/s$, as shown in fig. 4.8.

4.1.5 Distribution function g(z)

The main problem of the LIMM analysis is the reconstruction of the distribution function $g(z)$ from the pyroelectric current spectrum $I(\omega)$ (Lang, 2004). The LIMM equation (4.1) is a Fredholm integral equation of the first kind, and the determination of the solution is an ill-posed problem (Press *et al.*, 1992). Even though a number of techniques have been applied to obtain a unique solution of the LIMM equation (Lang, 2004), two of these methods are widely employed: the scanning-function method (Ploss *et al.*, 1992) and Tikhonov regularization (Tikhonov *et al.*, 1987; Weese, 1992). The scanning-function method proposes a distribution given by

$$g_a(z_r) \approx \frac{\kappa d}{\eta j_{\sim} AD}\left(\Re[I(\omega)] - \Im[I(\omega)]\right), \tag{4.13}$$

where the penetration depth $z_r = \sqrt{2D/\omega}$ should be small compared to the thickness d. That is, the information about the polarization at the near surface region is efficiently calculated with this method. On the other hand, Tikhonov regularization has been employed to provide information about the polarization in the bulk (Lang, 1991; Bloss *et al.*, 1997). The unique solution is obtained when the following expression is minimized:

$$\chi_r^2 = \sum_{\nu}\left|\frac{I(\omega_\nu)_{\exp} - I(\omega_\nu)_{\text{calc}}}{\sigma_\nu}\right|^2 + \lambda\int_0^d\left|\frac{d^2 g(z)}{dz^2}\right|^2 dz, \tag{4.14}$$

where σ_ν is the estimated error of the current at the frequency ω_ν and λ is the regularization parameter. The bias toward smooth solutions is a potential disadvantage of regularization methods, as suggested by the second term in the eqn. (4.14). In the quest for unbiased deconvolution techniques, the unregularized "steepest descent" method (also known as *van Cittert's* method (van Cittert, 1931)) has been used to analyze the LIMM measurements (Mellinger, 2004b).

The closest solution is given with the minimization of the expression

$$\chi^2[g] = (b - Ag)^*(b - Ag) \tag{4.15}$$

where $A_{\nu\mu} = R_{\nu\mu}/\sigma_\nu$ and $b_\nu = I_{\nu,\exp}/\sigma_\nu$. B^* is the complex conjugate of B, and

$$R_{\nu\mu} = i\omega\frac{A}{d}T(k_\nu, z_\mu) \times \begin{cases} (z_{\mu+1} - z_\mu)/2 & ; \mu = 0 \\ (z_{\mu+1} - z_{\mu-1})/2 & ; 1 \le \mu \le m-1 \, , \\ (z_\mu - z_{\mu-1})/2 & ; \mu = m \end{cases}$$

and $k_\nu = (1+i)\sqrt{\frac{\omega_\nu}{2D}}$.

Van Cittert's method is based on doing small steps in g_ν space in the direction opposite to the gradient $\nabla_g\chi^2$. If $g^{(n)}$ is the solution after n iterations, the next step is given by

$$g^{(n+1)} = \Re\left\{g^{(n)} - \frac{\beta^{(n)}}{2}\nabla_g\chi^2[g]\right\} = \Re\left\{g^{(n)} - \beta^{(n)}(A^*Ag^{(n)} - A^*b)\right\}, \qquad (4.16)$$

where $\Re$ denotes the real part. Convergence was ensured by replacing $\beta^{(n)}$ with $\beta^{(n)}/2$ until $\chi^2[g^{(n+1)}] < \chi^2[g^{(n)}]$, while $\beta^{(n+1)} = 2\beta^{(n)}$ after each successful iteration step. The initial distribution $g^{(0)}$ was obtained by interpolating the result of the scanning-function method. The distribution function $g(z)$ was calculated using the unregularized "steepest descent" method proposed by Mellinger (2004b).

4.1.6 Quasi-static pyroelectric coefficient

Dielectric spectroscopy studies have shown the presence of dipole relaxations in PETP (sec. 4.1.1). Even though these relaxations have been identified, this material does not exhibit a considerable pyroelectric coefficient. In materials where the polarization is small, a unique determination of the electric field and the polarization is generally impossible (Bauer and Bauer-Gogonea, 2003). Nevertheless, for the determination of a charge profile in these samples, a first approximation is available with the use of the quasi-static pyroelectric coefficient p_{QPC}:

$$p_{QPC} = \left.\frac{\partial D}{\partial T}\right|_{E=0,P} = \left.\frac{1}{A}\frac{\partial Q}{\partial T}\right|_{E=0,P} \qquad (4.17)$$

where D is the electric displacement, Q is the image charge at the electrode and A is the electrode area. In the case of weak pyroelectric materials, the pyrocurrent is so small that it is covered by noise, as shown in fig. 4.9.

If the temperature is set to have a sinusoidal form, the determination of the current due to the temperature change can be determined with the help of the Fast Fourier Transformation (FFT). Fig. 4.10 shows in a flow diagram how the analysis of the quasi-static pyroelectric coefficient (QPC) was performed. This technique is a numerical equivalent of a *lock-in* amplifier for a single frequency.

In this procedure, the temperature measured is interpolated with a spline function of third order and resampled with a number of $N = 2^n$ data points. The 2^n data points is the
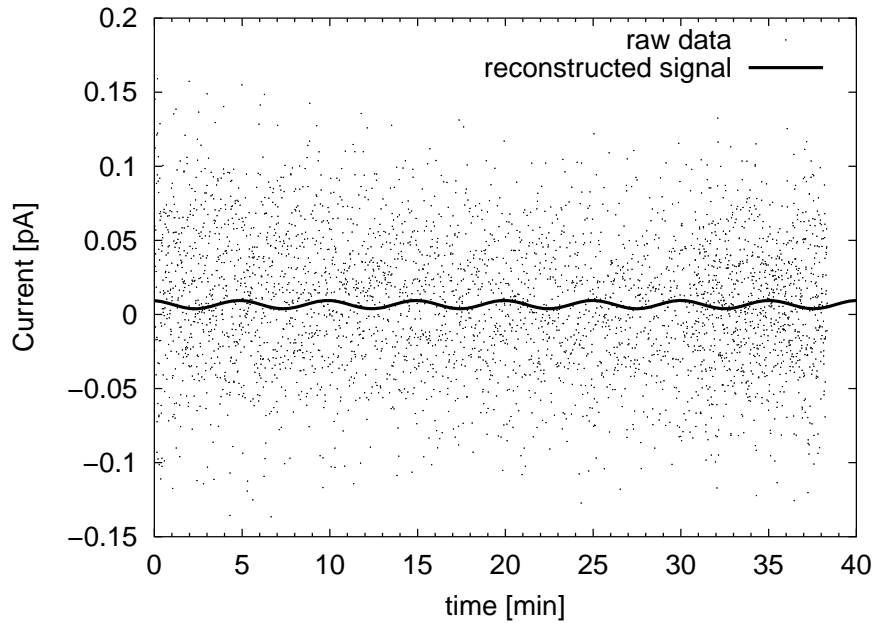
Figure 4.9: Comparison of the reconstructed pyroelectric signal and the raw data of the quasi-static pyroelectric measurement performed with a bias voltage of 23 V (1 V/μm) at −120 °C

necessary condition to apply the FFT. N is similar to the number of data points of the raw data. The Fourier transform of the measured temperature $T(\omega) = \text{FFT}\{T(t)\}$ is calculated. The selection of the frequencies is performed as follows:

The frequency selection is performed on the base that the temperature signal is considered as a sinusoidal function of time. In our case, it is considered two main frequencies of the $T(\omega)$ spectrum to perform the analysis. The first frequency gives information of the temperature at which the experiment was performed (−100, −50, 0, 25 ... °C). This is given by the first element of the $T(\omega)$ spectrum at $\omega = 0$ s^{-1} or $f = 0$ Hz ($\omega = 2\pi f$). The second frequency is the i−th element of the FFT power spectrum (P_i) given by

$$P_i \approx \frac{T_{\text{m,exp}}N^{1/2}}{2} \pm 10\%. \tag{4.18}$$

Where, $T_{\text{m,exp}}$ is the amplitude of the temperature oscillation programmed in the setup. Since the sinusoidal form cannot be completely followed under experimental conditions, the $T_{\text{m,exp}}$ has a deviation from its programmed value. This deviation is considered to be a band of about 10 % (fig. 4.11).

The analysis of the frequency selection is simplified due to the accuracy of the setup to generate a sinusoidal oscillation of the temperature. This is reflected in the P_i spectrum with a sharp band of elements with amplitudes inside the 10% tolerance. Here, these are two elementes from the power spectrum (fig. 4.11). As it can be seen, these elements are two or three orders of magnitude larger than the others.
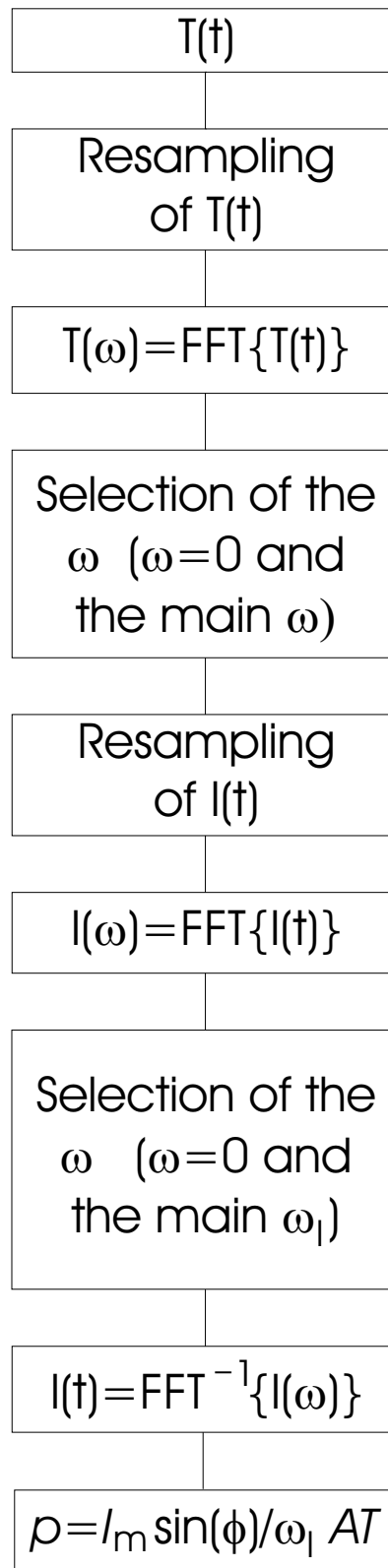
$$T(t)$$

$$\text{Resampling of } T(t)$$

$$T(\omega) = FFT\{T(t)\}$$

$$\text{Selection of the } \omega \ (\omega = 0 \text{ and the main } \omega)$$

$$\text{Resampling of } I(t)$$

$$I(\omega) = FFT\{I(t)\}$$

$$\text{Selection of the } \omega \ (\omega = 0 \text{ and the main } \omega_l)$$

$$I(t) = FFT^{-1}\{I(\omega)\}$$

$$p = I_m \sin(\phi)/\omega_l \, AT$$

Figure 4.10: Flow diagram to analyze the quasi-static pyroelectric measurement. ϕ is the phase shift of the current (I) and the temperature (T). A is the electrode area and p is the quasi-static pyroelectric coefficient.
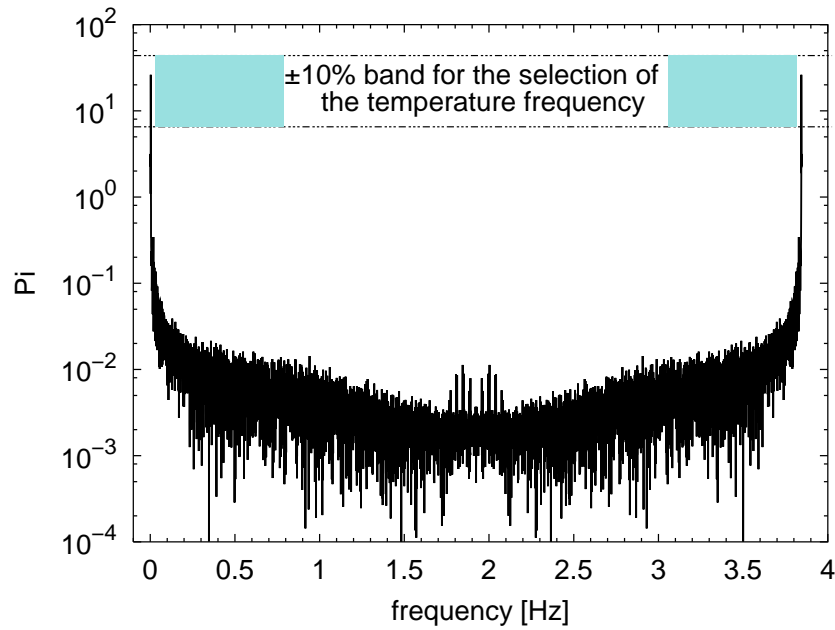
Figure 4.11: Power diagram of the FFT of the temperature and the band selection of the i−th element at frequency ω_1.

A linear interpolation of the raw data (current) is performed with a spline function of first order. The resampling is performed with N number of data points, which must be the same as that one of the resampled temperature. The Fourier transform $I(\omega) = \text{FFT}\{I(t)\}$ is performed. The i-th elements of the $I(\omega)$ spectrum which correspond to those of the $T(\omega)$ spectrum are selected. That is, the selected i-th elements from $I(\omega)$ have the same frequency as their corresponding i-th elements from $T(\omega)$. The other elements of the $I(\omega)$ spectrum are neglected.

The actual frequency f_i (in Hertz) of the temperature and the current is determined from the following expression:

$$f_i = \frac{i}{Nh}, \qquad i = 1, 2, \ldots, N \tag{4.19}$$

where h is the step size from the resampled function. The phase shift ϕ of the current $I(t)$ with respect to the temperature $T(t)$ is given by

$$\phi = \arctan \frac{\Im\{I(\omega)\}}{\Re\{I(\omega)\}} - \arctan \frac{\Im\{T(\omega)\}}{\Re\{T(\omega)\}} , \tag{4.20}$$

where $\Im$ and $\Re$ are the imaginary and the real part of the $I(\omega)$ and $T(\omega)$ spectra, respectively.

The QPC (p_{QPC}) is calculated from the component of the current shifted 90° with respect to the temperature phase (for more details refer to appendix B)

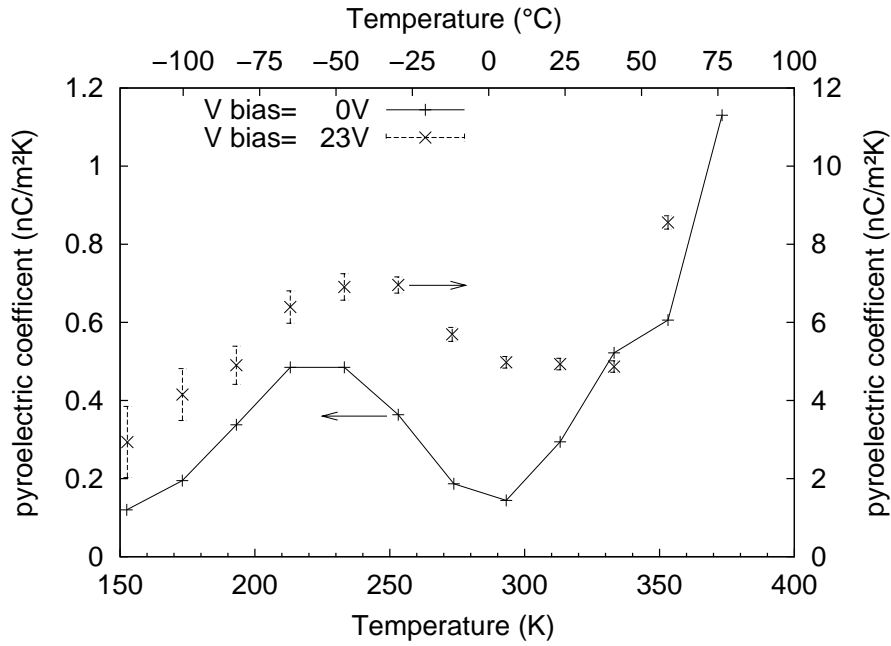$$p_{\text{QPC}} = \frac{I_{\text{m}} \sin \phi}{A \omega T_{\text{m}}} \tag{4.21}$$

Figure 4.12: Measured data of quasi-static pyroelectric coefficient of uncharged PETP films with and without bias voltage ($E_{bias} = 1$ V/μm).

where A is the electrode area, and

$$I_m = 2\frac{|I(\omega_1)|}{N^{1/2}} \text{ and } T_m = 2\frac{|T(\omega_1)|}{N^{1/2}}$$

are the amplitudes of the current and temperature calculated at the selected frequency (ω_1) from the $I(\omega)$ and $T(\omega)$ spectra, respectively.

The main problem of this analysis is the size of the noise compared to the pyroelectric signal. The noise level can be more than 100 times the size of the signal. In these cases, the pyroelectric measurement only delivers the order of magnitude of the QPC. For PETP, the order of magnitude is estimated to be around 10^{-10} C/(m^{2}K). Despite the magnitude of the noise, the field-free quasi-static pyroelectric coefficient calculated using this analysis shows a similar behavior to the field induced coefficient (fig. 4.12).

A statistically significant result can be obtained by performing experiments with a bias voltage. This assumption implies the fact that the amplitude of the calculated error is not larger than the change of the quasi-static pyroelectric coefficient for different temperatures. In the worst case for PETP, a bias voltage of 23 V (1 V/μm) generates a signal with a noise level up to 18 times larger than the current obtained after the FFT analysis. An error of about 31% is obtained from simulations performed with a signal covered by a random noise which is approx. 18 times larger than the signal. As the temperature increases, the pyroelectric signal becomes larger, and the noise level is reduced. This method becomes efficient when the noise level is about 3 times larger than the calculated current for the pyroelectric coefficient. In this case, simulations have shown an error of about 5% .
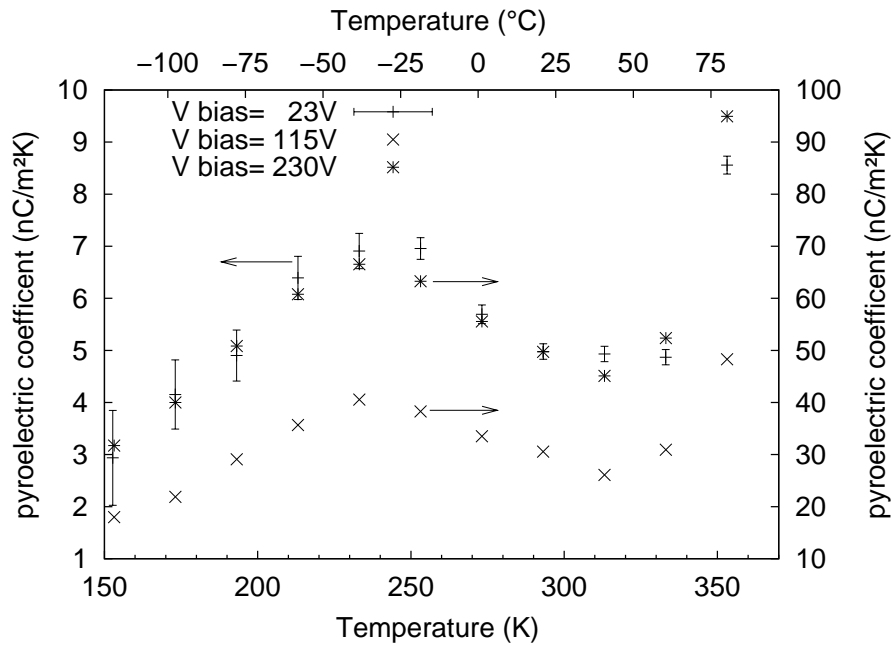
Figure 4.13: Measured data of the induced quasi-static pyroelectric coefficient of uncharged PETP films 23 μm using bias voltage of 23, 115 and 230 V.

The measured data of the quasi-static pyroelectric measurement is shown in fig. 4.13. The error bars are shown in the case of 23 V (1 V/μm). As it can be seen, the change of the pyroelectric coefficient with the temperature is larger than the amplitude of the error bar. The error bars for larger bias voltages are omitted, because the noise level is smaller than the pyroelectric signal. This kind of noise can generate errors less than 5%.

A comparison between the curves in fig. 4.13 shows a similar behavior. From this comparison a guide curve can be drawn to describe the pyroelectric coefficient for low temperatures ($T < T_g$). The raw data is normalized at the peak around -40 °C (fig. 4.14) and a guide curve is obtained from the averaged normalized data. This guide curve is obtained from the interpolation with splines of third order using the average of the normalized data. As it can be seen, the induced-QPC presents a maximum at approx. -40 °C. This behaviour resembles the one of the dielectric losses (ε") of PETP films at low temperatures (fig. 4.2). This result indicates that the induced QPC rises from the same molecular motions that cause the dielectric relaxation. In this case, it is the β-relaxation.

Thermal expansion of the material can be present in these experiments. The volume expansion together with the dielectric response are explained by the molecular movements. Broemme *et al.* (1981) use the concept of free volume to explain the charging and discharging behavior of PETP.

Usually, when a sample is charged at high temperatures not only the permanent dipoles signal is present in the pyroelectric coefficient, but also the effect of the injected charges near to the electrodes. This effect is also present when PSD experiments are performed. When a sample is irradiated with light, the distribution of the trapped charge-carriers is
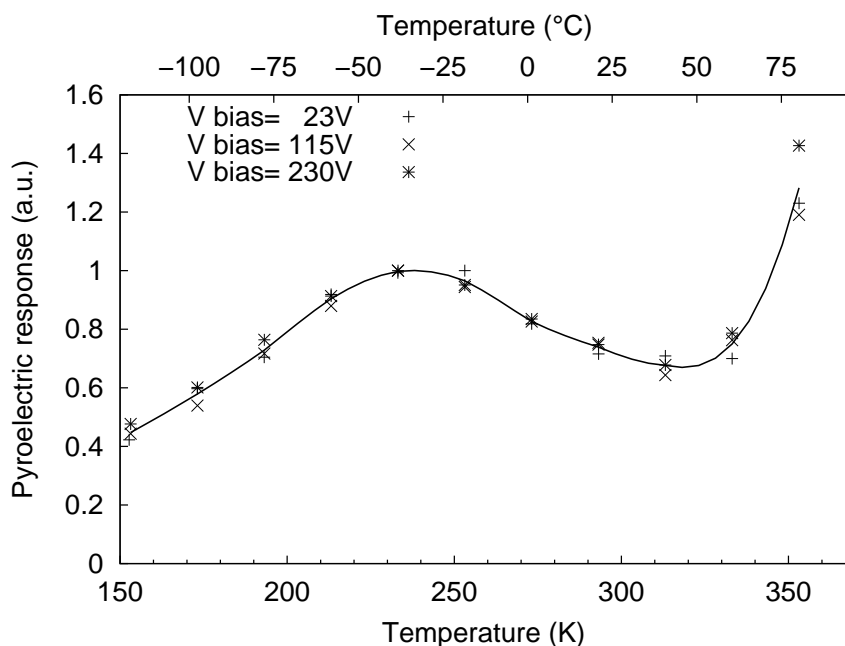
Figure 4.14: Curves of the field-induced quasi-static pyroelectric coefficient of uncharged PETP films normalized at the peak around $-40\,°C$ with a guide curve.
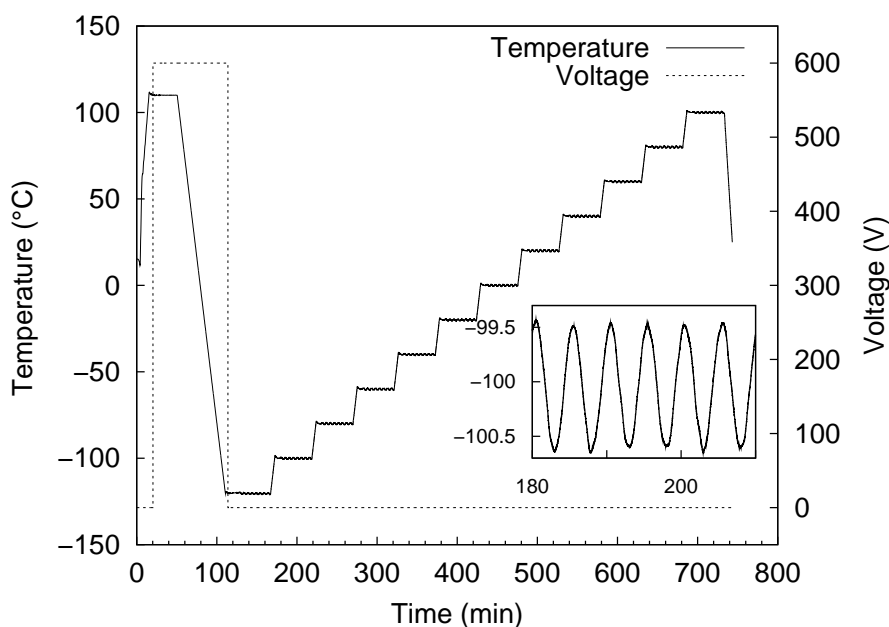

Figure 4.15: Experimental procedure of a simultaneous step-wise TSD and QPM measurements for a charged PETP film using the contacting electrodes method at $110\,°C$ with an electric field about 26 MV/m. The inset shows the sinusoidal oscillation of the temperature which takes place every step of the temperature ramp to determine the quasi-static pyroelectric coefficient.
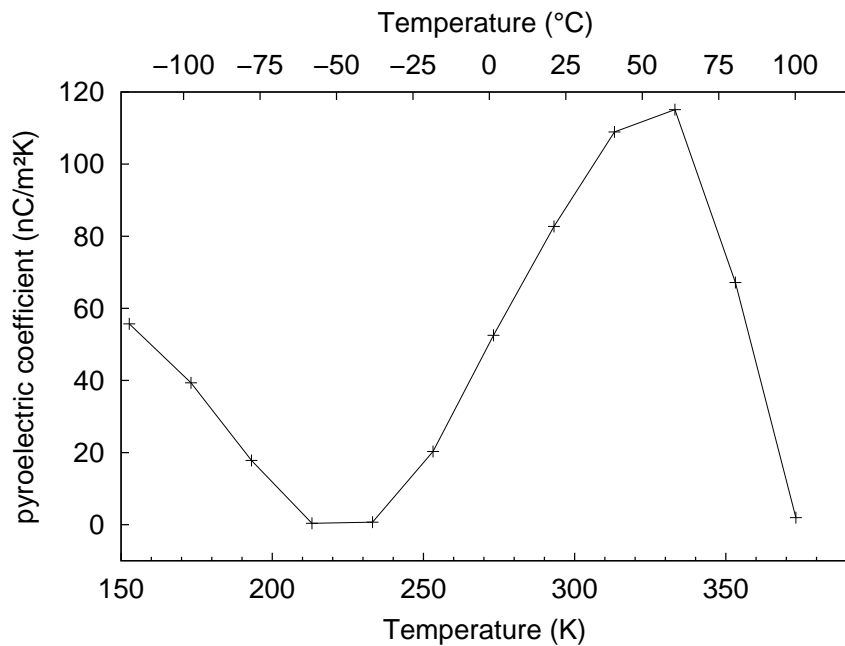
Figure 4.16: Quasi-static pyroelectric measurements during the step-wise TSD for a charged PETP film using the contacting electrodes method at 110 °C with $E = 26$ MV/m.

affected. Under this circumstance, only the signal corresponding to the stored charge is affected, but not the orientation of the permanent dipoles. Schneider *et al.* (1983) explained that the electret behavior of PETP was attributed to the interaction of permanent dipoles, stored charges and dipoles oriented at the glass transition temperature (T_g) due to the electric field generated by the stored charge.

In order to investigate the effect of the stored charges in the pyroelectric coefficient, the quasi-static pyroelectric measurement was performed every 20 °C, while a step-wise TSD was performed (fig. 4.15). In this experiment, a PETP film was charged at high temperature using the contacting electrodes method ($V = 600$ V, $T = 110$ °C) and cooled down to -120 °C. As it can be seen in fig. 4.16, the quasi-static pyroelectric coefficient varies as the temperature rises. At low temperatures the decrease of QPC can be attributed to the release of the charges from the shallow traps. As the temperature increases, the pyroelectric signal increases due to the softening of the sample giving more freedom of orientation to the permanent dipoles. After reaching 60 °C, the pyroelectric signal decreases due to loss of the orientation of the permanent dipoles. In that way, it is possible to observe the influence of the trapped charges in the QPC at low temperatures ($T < T_g$).

When a sample is freshly charged at $T_c = 110$ °C under light irradiation, the internal electric field can be approx. 20 V/μm, resulting in a charge-dipole interaction (Schneider *et al.*, 1983). Due to the light irradiation, more charge carriers are trapped in the samples than in those samples which are not irradiated during charging. A clear difference in the internal electric field profile of samples charged at 110 °C with and without light irradiation is observed (see sec. 4.1.7). When charging is done at high temperatures with light irradiation, the effect of the stored carriers will generate an induced-QPC of about
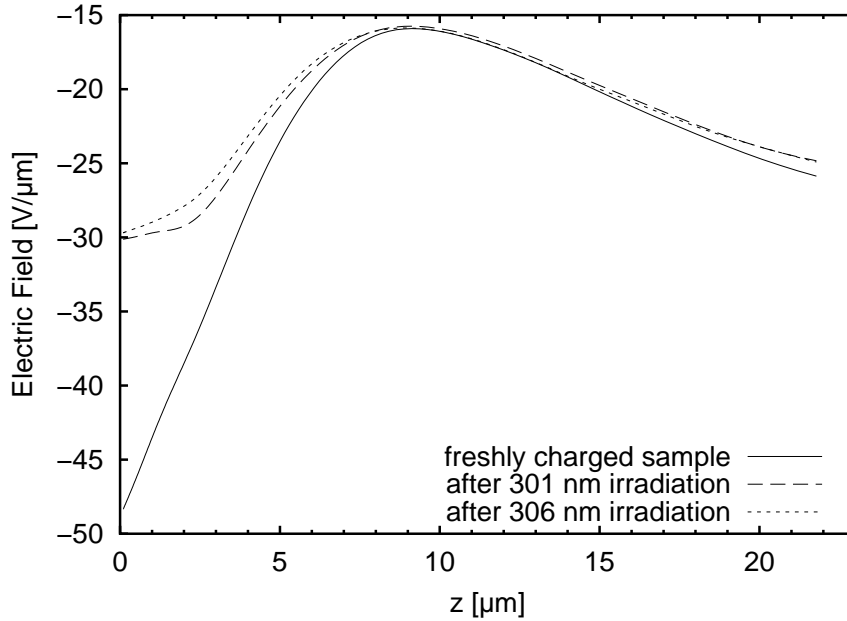
Figure 4.17: Calculated electric field in PETP films ($d = 23$ µm) using the LIMM technique (eqn. (4.3)) and the QPC. After charge decay due to light irradiation, a new QPC was calculated using eqn. (4.23). Charging with the contacting electrodes method, $V = -600$ V, $\lambda = 305$ nm, $T_c = 110\,°C$, 30 min. Irradiated side of the sample at $z = 0$ µm.

50 nC/(m^2 K). After light irradiation in PSD experiments, the charge density and consequently the induced-QPC decay. Due to the reduction of the stored charge, it is necessary to calculate a new induced-QPC. An estimation of this reduction can be achieved with the help of a combination of the parametric curve of the induced QPC (fig. 4.14) and the resulting QPC of the step-wise TSD (fig. 4.16). Hereby, the new quasi-static pyroelectric coefficient can be estimated using the heuristic expression shown in eqn. (4.22). In this expression, it is considered that the stored charge is responsible for one half of the QPC which is affected by either thermal- or photo-stimulated detrapping. The other half of the QPC rises from the oriented dipoles.

$$p_{\text{QPC,new}} = \frac{m}{2m - 1} p_{\text{QPC,fc}}, \tag{4.22}$$

here $m = p_{\text{QPC,calc}}/p_{\text{QPC,tsd}} \gtrsim 1.0$. Where $p_{\text{QPC,new}}$ is the quasi-static pyroelectric coefficient after the PSD, $p_{\text{QPC,fc}}$ is the quasi-static pyroelectric coefficient of a freshly charged sample obtained from the QPM technique, $p_{\text{QPC,tsd}}$ is the quasi-static pyroelectric coefficient obtained from the TSD experiment (fig. 4.16), and $p_{\text{QPC,calc}}$ is the quasi-static pyroelectric coefficient calculated from the master curve (fig. 4.14).

If $m \approx 1$ ($p_{\text{QPC,calc}} \approx p_{\text{QPC,tsd}}$), then $p_{\text{QPC,new}} \approx p_{\text{QPC,fc}}$. That is, the QPC has its origin mainly from the molecular dipoles. On the other hand, if $m \gg 1$ ($p_{\text{QPC,calc}} \gg p_{\text{QPC,tsd}}$), then $p_{\text{QPC,calc}} \approx p_{\text{QPC,tsd}}/2$. This may indicate that the charges are able to generate up to the half of the QPC. Nevertheless, more research should be performed in this direction.

Substituting *m* in eqn. (4.22), it can be presented as

$$p_{QPC,new} = \frac{p_{QPC,fc}}{1 + \frac{p_{QPC,calc} - p_{QPC,tsd}}{p_{QPC,calc}}}. \tag{4.23}$$

The use of eqn. (4.23) to calculate a new QPC after light irradiation is shown in fig. 4.17, where the electric field of a charged sample at 110 °C with an applied voltage of -600 V and UV-irradiated at $\lambda = 305$ nm during 30 min was calculated. The electric field from a freshly charged sample is calculated using eqn. (4.3). The QPC is calculated from the master curve (explained in this section) at 25 °C. The parameters employed to calibrate the LIMM measurements are listed below:

- Thermal conductivity κ: 0.1935 W/(m K) from Du Pont Teijin (2000)

- Thermal expansion coefficient α_z: 17×10^{-6} 1/K from Du Pont Teijin (2000)

- Power of the laser converted into heat $\eta \iota$: 4.8×10^{-3} W from eqn. (4.9)

- Diffusivity D: $(1.16 \pm 0.09) \times 10^{-7}$ m^2/s from the fit of the eqn. (4.12)

- Temperature coefficient of the permittivity α_ε and permittivity ε are obtained from the dielectric spectra presented in sec. 4.1.1

The distribution function $g(z)$ is determined using the unregularized "steepest descent" method proposed by Mellinger (2004b) (see sec: 4.1.5). The pyroelectric coefficient $p(z)$ is approximated to the QPC and considered constant ($p_{QPC,calc}$). After the photo-stimulated discharge the effect of the stored charges decreases. Therefore, a new pyro-electric coefficient is calculated with eqn. (4.23).

4.1.7 Electric field and charge profile inside the PETP films

Using the LIMM technique, it was possible to monitor *in situ* the change of the internal electric field $E(z)$ profile induced by the light irradiation. Then, the charge density $\rho(z)$ profile was calculated from the electric field, which was calculated using two approaches. The *first approach* employs the quasi-static pyroelectric coefficient QPC as the pyroelectric coefficient $p(z)$. The QPC was considered constant throughout the sample. The description is shown at the end of sec. 4.1.6. The charge density $\rho(z)$ was calculated from this electric field profile. In the *second approach*, the $p(z)$ was calculated from LIMM measurements of a sample charged at 110 °C without irradiation. Using this value, the charge profile $\rho(z)$ of the sample charged with light-irradiation is determined. The resulting charge profile and the one determined from measurements at -100 °C are taken as reference to perform an interpolation to determine the charge profile at intermediate temperatures (-50 to 25 °C). The interpolation was carried out by means of the Arrhenius law. Then the electric field due to the stored charge was calculated. The parameters employed to calibrated the LIMM measurements are listed at the end of sec. 4.1.6.
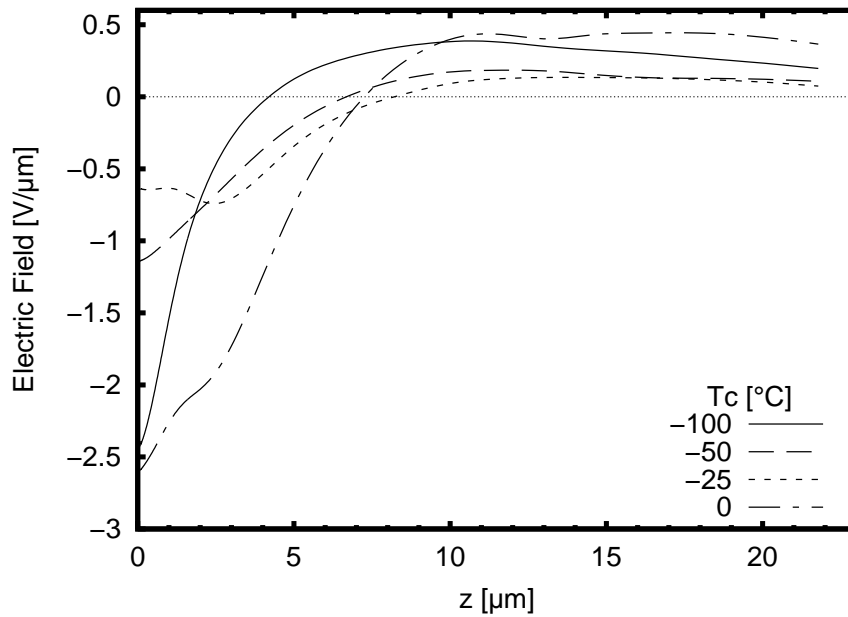
Figure 4.18: Electric field profile in PETP films ($d = 23$ μm) measured by means of the LIMM method and the QPC (first approach). Freshly charged samples ($V = -600$ V, $\lambda = 305$ nm, 30 min), at $T_c = -100, -50, -25$ and 0 °C. Irradiated side of the sample at $z = 0$ μm.
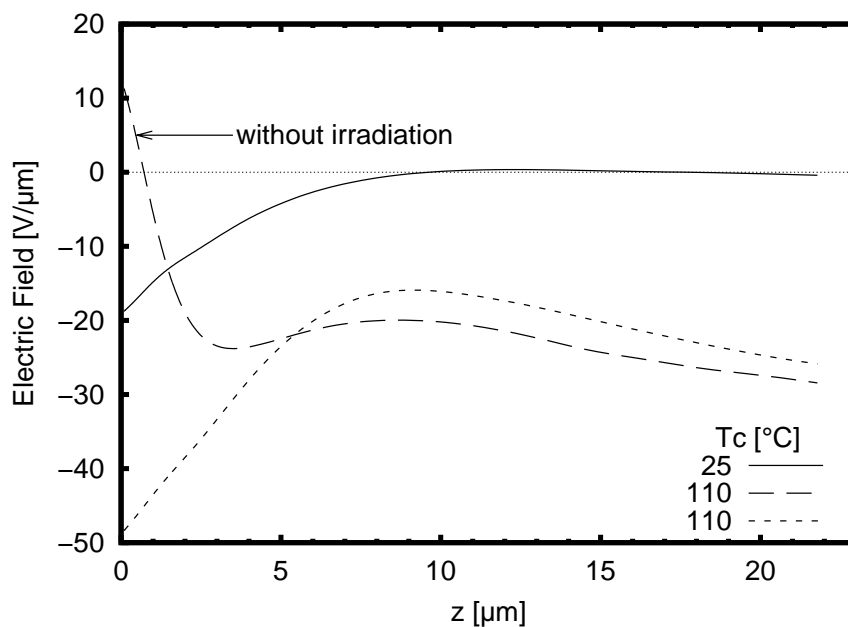

Figure 4.19: Electric field in freshly-charged PETP films ($d = 23$ μm) measured by means of the LIMM method and the QPC (first approach). Charging with $V = -600$ V and $\lambda = 305$ nm at $T_c = 25$ and 110 °C, and charging with $V = -600$ V without irradiation at $T_c = 110$ °C for 30 min. Irradiated side of the sample at $z = 0$ μm.
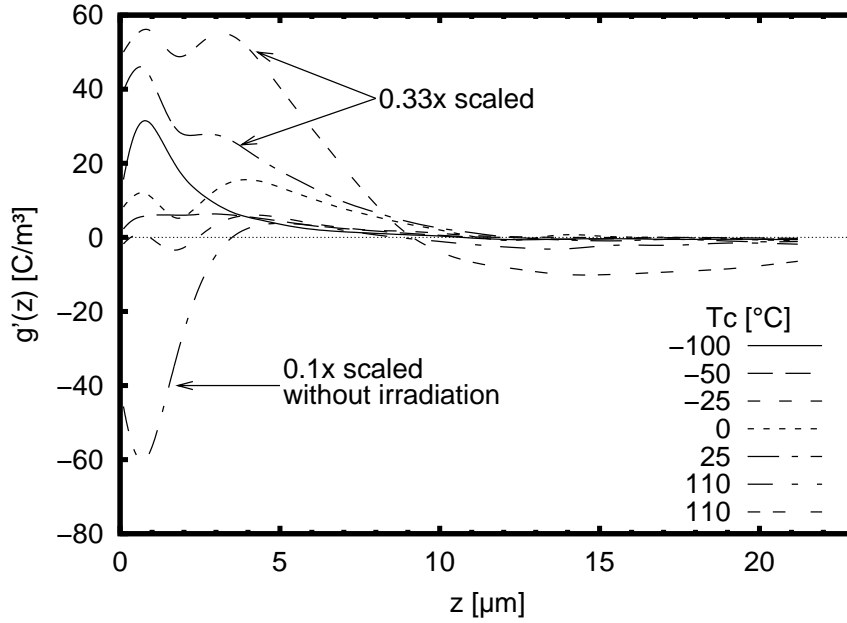
Figure 4.20: Derivative of the distribution function $g'(z) = (dg(z)/dz)/(\alpha_\varepsilon - \alpha_z)$ of freshly-charged PETP films ($d = 23$ μm) measured by means of the LIMM method. Charged with $V = -600$ V, $\lambda = 305$ nm, at $T_c = -100$, -50, -25, 0, 25, and 110 °C and non-irradiated samples at 110 °C. Irradiated side of the sample at $z = 0$ μm.

The first approach: Calculation of the internal electric field $E(z)$ using the QPC

The procedure of charging PETP samples is depicted in figs. 3.14(a) and 3.14(b). The samples were driven to a charging temperature of $T_c = -100$, -50, -25, 0, 25 and 110 °C, and charged with an applied voltage of -600 V and photo-excited with monochromatic light at 305 nm for 30 min. Another sample was also charged at 110 °C, but without photo-excitation. The electric field E calculated with the procedure mentioned earlier in sec. 4.1.3 is shown in figs. 4.18 and 4.19 for freshly charged samples. The irradiated side of the sample is located at depth zero ($z = 0$ μm) in the graphs. If the internal electric field is due to stored charge, the integral of the electric field in short circuited sample must be zero,

$$\int_0^d E \, dz = 0. \tag{4.24}$$

The integration of the electric field (eqn. (4.24)) for samples charged at temperatures $T_c \leqslant 0$ °C give values smaller than 2 V. In the case of $T_c = 25$ °C, the integral given by eqn. (4.24) is approx. 10 V.

On the other hand, the integral of the electric field in samples charged at $T_c = 110$ °C does not approach zero. As it can be observed, the electric field profiles for non-irradiated and irradiated samples are completely different near the electrode ($z = 0$ μm). For samples charged without irradiation, the electric field rises mainly from the oriented dipoles. But for samples, which were light irradiated during charging, the electric field profile de-
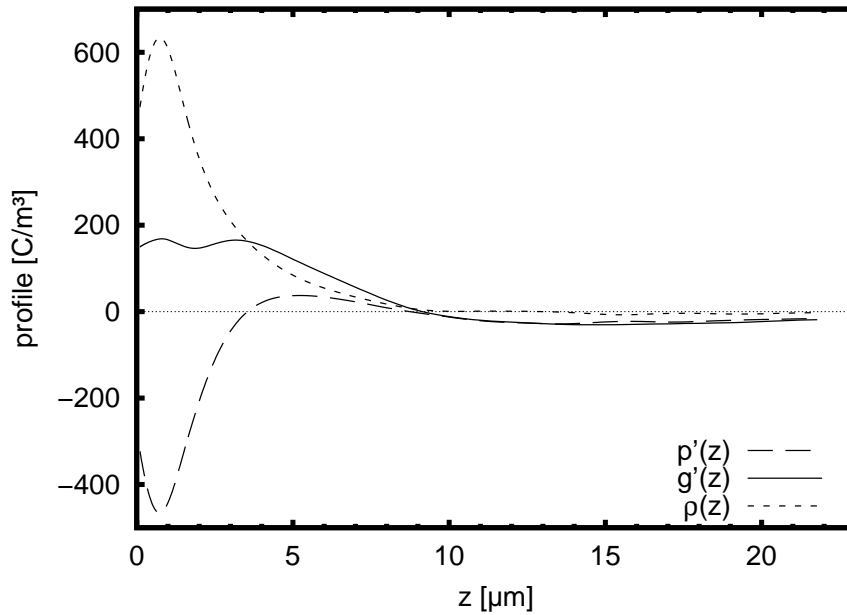
Figure 4.21: Charge profile of a freshly charged sample ($d = 23$ μm) calculated from LIMM measurements, using the second approach. The respective electric field is shown in fig. 4.23. Charging with $V = -600$ V, $\lambda = 305$ nm, at $T_c = 110$ °C. Irradiated side of the sample at $z = 0$ μm. $g'(z) = (dg_{D+C}(z)/dz)/(\alpha_\varepsilon - \alpha_z)$ (irradiated sample). $p'(z) = (dg_D(z)/dz)/(\alpha_\varepsilon - \alpha_z)$ (non-irradiated sample). $\rho(z) = g'(z) - p'(z)$.

scribed by $g(z)$ is the result of a combination of the signals rising from the charges and dipoles.

The second approach: Calculation of the internal electric field $E(z)$ using the pyro-electric coefficient $p(z)$

The charge density $\rho(z)$ profile

In order to determine the charge density profile for samples charged at 110 °C, it is necessary to combine the distributions $g_{D+C}(z)$ and $g_D(z)$ of irradiated and non-irradiated samples during charging, respectively. The derivative of eqn. (4.2) for both samples are

$$\frac{1}{(\alpha_\varepsilon - \alpha_z)}\frac{dg_D(z)}{dz} = \varepsilon\varepsilon_0\frac{dE_D(z)}{dz} + \frac{1}{(\alpha_\varepsilon - \alpha_z)}\frac{dp_D(z)}{dz} \qquad (4.25)$$

and

$$\frac{1}{(\alpha_\varepsilon - \alpha_z)}\frac{dg_{D+C}(z)}{dz} = \varepsilon\varepsilon_0\frac{dE_{D+C}(z)}{dz} + \frac{1}{(\alpha_\varepsilon - \alpha_z)}\frac{dp_{D+C}(z)}{dz}. \qquad (4.26)$$

The profiles ($g(z)$, $E(z)$ or $p(z)$) with subscript D refer to the non-irradiated sample during charging. While the profiles ($g(z)$, $E(z)$ or $p(z)$) with subscript $D+C$ refer to the irradiated sample during charging. Fig. 4.21 shows the derivative of the distribution functions
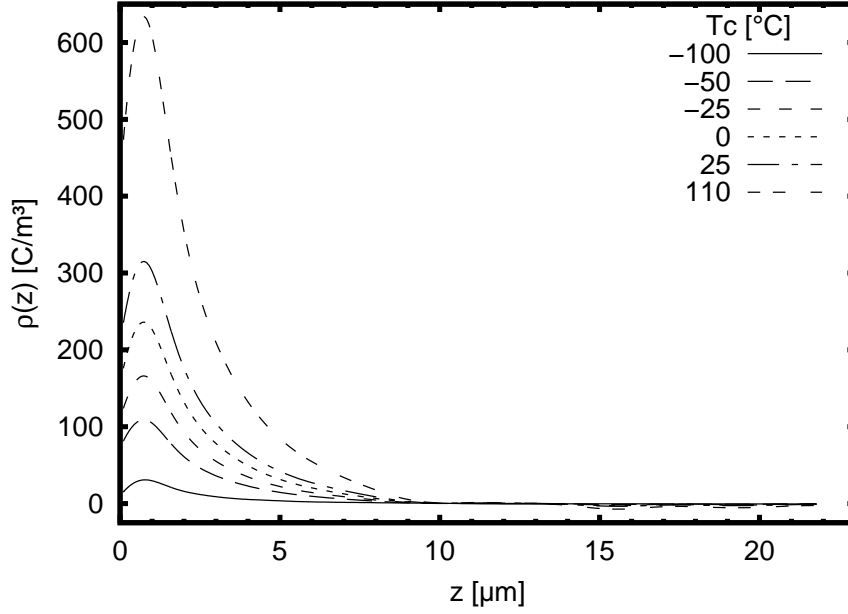
Figure 4.22: Charge profiles $\rho(z)$ of PETP films ($d = 23$ μm) calculated from the interpolation performed from $\rho(z)$ of samples charged at -100 and $110\,°C$. The interpolation using Arrhenius' law with an activation energy of 1.298×10^{-20} J. Charging with $V = -600$ V, $\lambda = 305$ nm, at $T_c = -100, -50, -25, 0, 25$ and $110\,°C$. Irradiated side of the sample at $z = 0$ μm.

of non-irradiated $g_D(z)$ and irradiated $g_{D+C}(z)$. As it can be observed, the derivative of $g_D(z)$ shows a kind of single charge layer near to the electrode. Since the integral of the electric field of this sample does not approach zero (eqn. (4.24)), it can be said that the electric field is due to dipole orientation. This coincides with the PPS-measurements on samples charged under similar conditions, namely $T_c = 110\,°C$ without light-irradiation in nitrogen environment (fig. 4.7).

In order to minimize the effect of the injected charges from the electrodes, the distribution functions of a freshly charged sample and a sample after the first photo-stimulated charge decay ($\lambda = 299$ nm in fig. 4.31(b)) were averaged. Differentiating the resulting function $g_D(z)$ and neglecting the possible effect of the injected charges (i.e. $E_D(z) \approx 0$), the eqn. (4.25) can be simplified

$$\frac{1}{(\alpha_\varepsilon - \alpha_z)} \frac{dg_D(z)}{dz} = \frac{1}{(\alpha_\varepsilon - \alpha_z)} \frac{dp_D(z)}{dz}. \tag{4.27}$$

As it can be observed from eqn. (4.27), the distribution function $g_D(z)$ gives the dipole profile in the sample $p_D(z)$. If $p_D(z) \approx p_{D+C}(z) \approx p(z)$, the subtraction of eqn. (4.27) from eqn. (4.26) yields the charge density profile of the sample charged at $110\,°C$:
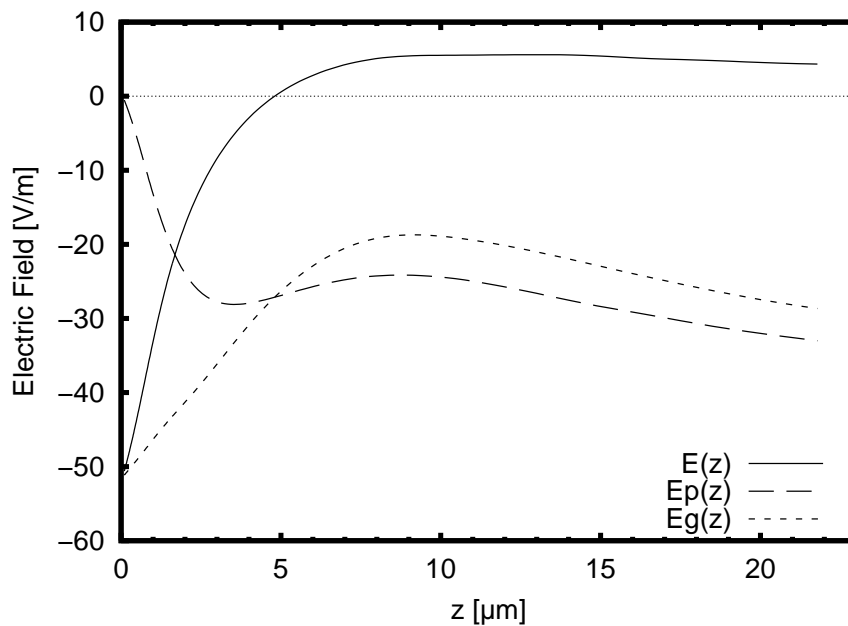
Figure 4.23: Electric field profile of a freshly charged sample ($d = 23$ μm), calculated from LIMM measurements using the second approach. The respective charge profile is shown in fig. 4.21. Charging with $V = -600$ V, $\lambda = 305$ nm, at $T_c = 110$ °C. Irradiated side of the sample at $z = 0$ μm. Electric field due to stored charge $E(z)$, dipoles $E_p(z)$ and distribution function $E_g(z) = E(z) + E_p(z)$.

$$\rho(z) = \frac{1}{(\alpha_\varepsilon - \alpha_z)} \frac{dg_{C+D}(z)}{dz} - \frac{1}{(\alpha_\varepsilon - \alpha_z)} \frac{dg_D(z)}{dz} \qquad (4.28)$$

$$= \frac{1}{(\alpha_\varepsilon - \alpha_z)} \left[\frac{dg_{C+D}(z)}{dz} - \frac{dp(z)}{dz} \right]. \qquad (4.29)$$

The charge profile $\rho(z)$ together with the derivatives of the pyroelectric coefficient $p(z)$ and the distribution profile $g(z)$ is plotted in fig. 4.21. As it can be observed, the charge profile calculated from eqn. (4.29) resembles that one of samples charged at -100 °C (fig. 4.20). This indicates that the double peak of the derivative of $g(z)$ of samples charged at -50, -25, 0, and 25 °C (fig. 4.20) could be a combination of distribution functions of the charge and dipoles. However, it is important to remark that the distribution functions $g(z)$ were calculated using the *unregularized steepest descent* method (sec. 4.1.5, (Mellinger, 2004b)) from noisy data. That means that the double peak could be also an artifact from the mathematical approach. Still, a charge profile can be calculated from these data.

Experimental results (see sec. 4.3.2) indicate that the photocurrent peak depends on the temperature following the Arrhenius' law. In that sense, it is possible to propose a charge distribution $\rho(z)$ calculated from the interpolation of the $\rho(z)$ distributions from samples charged at -100 and 110 °C. The interpolation of both $\rho(z)$ distributions using Arrhe-

Figure 4.24: Electric field profile $E(z)$ due to $\rho(z)$, calculated from LIMM measurements. Charging with $V = -600$ V, $\lambda = 305$ nm, at $T_c = -100$, -50, -25 and 0 °C. Irradiated side of the sample at $z = 0$ μm.

nius' law yields an activation energy of approx. 1.298×10^{-20} J (0.081 eV). The $\rho(z)$ ditributions calculated from this interpolation are shown in fig. 4.22.

The internal electric field $E(z)$

The internal electric field due to charges stored in a sample with short-circuited metal electrodes can be calculated from the following expression (Sessler, 1999c):

$$E(z) = \frac{1}{\varepsilon_0 \varepsilon} \left(\hat{\sigma} - \int_0^z \rho(z')dz' \right), \tag{4.30}$$

with

$$\hat{\sigma} = \frac{1}{d} \int_0^d (d - z)dz.$$

Here, d is the thickness of the sample.

The internal electric field $E(z)$ due to the stored charge $\rho(z)$ in the sample charged at 110 °C with light irradiation was calculated using the eqn. (4.30). The electric field $E_p(z)$ which rises from the dipoles can be obtained by the integration of the eqn. (4.27). The internal electric field $E_g(z)$ which rises from stored charges and oriented dipoles can be calculated from the addition of the electric field distributions generated by the stored charges and the oriented dipoles:

$$E_g(z) = E_p(z) + E(z), \tag{4.31}$$
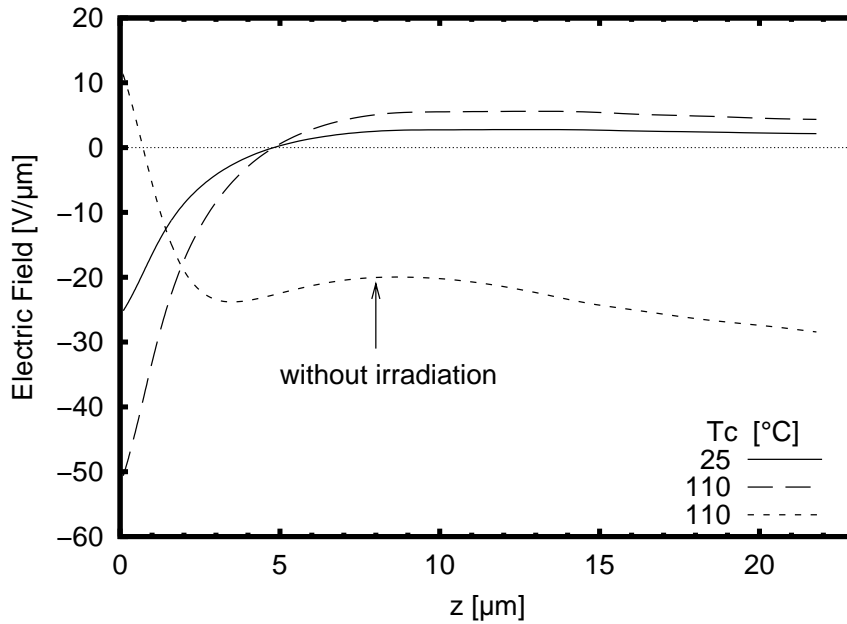
Figure 4.25: Electric field profile $E(z)$ due to $\rho(z)$ and dipole orientation (sample without irradiation), calculated from LIMM measurements. Charging with $V = -600$ V, $\lambda = 305$ nm, at $T_c = 25$, and $110\,°C$ with and without irradiation. Irradiated side of the sample at $z = 0$ µm.
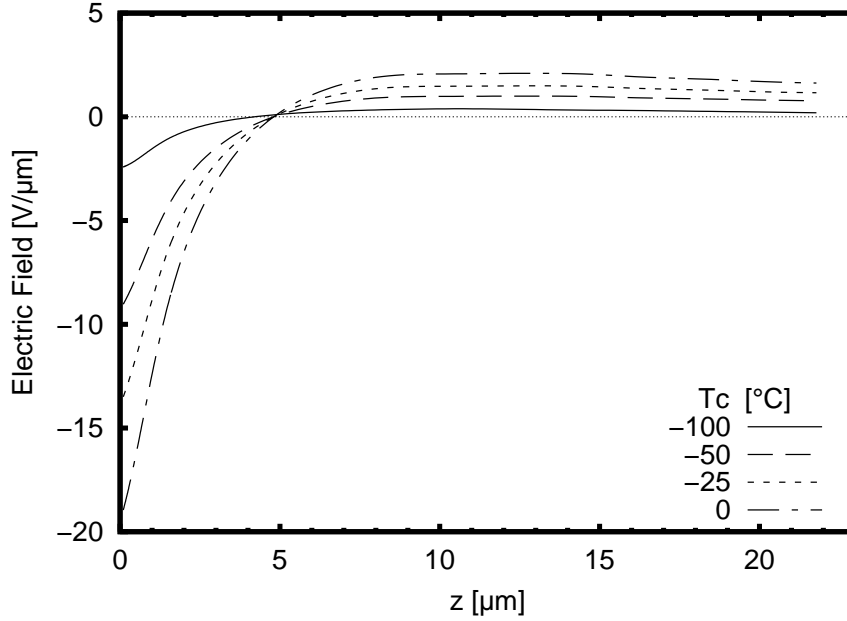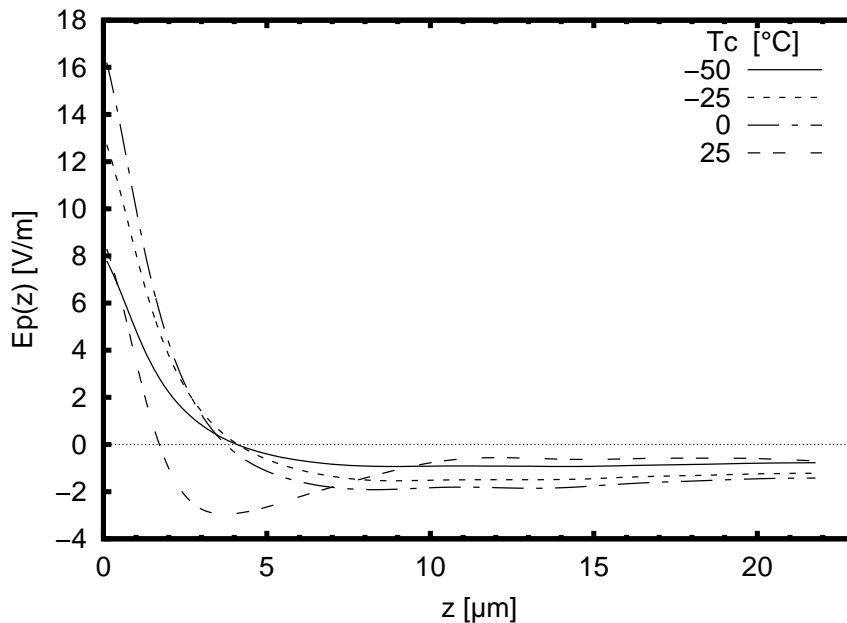

Figure 4.26: Electric field profile of a sample due to dipoles, calculated from LIMM measurements. Charging with $V = -600$ V, $\lambda = 305$ nm, at $T_c = -50, -25, 0$ and $25\,°C$. Irradiated side of the sample at $z = 0$ µm.

with $E_g(z) = g(z)/\varepsilon_0\varepsilon(\alpha_\varepsilon - \alpha_z)$, $E_p(z) = p(z)/\varepsilon_0\varepsilon(\alpha_\varepsilon - \alpha_z)$ and $E(z) = \int \rho(z)dz/\varepsilon_0\varepsilon$. The electric field profiles due to the distribution function $E_g(z)$, dipole distribution $E_p(z)$ and charge distribution $E(z)$ are shown in fig. 4.23. A brief comparison between the electric fields of the freshly-charged sample calculated using the QPM (*first approach* in fig. 4.17) and $E_g(z)$ from fig. 4.23 shows a small difference in the magnitude (3 V/µm).

Figs. 4.24 and 4.25 show the $E(z)$ profiles for freshly charged samples at different temperatures. The $E(z)$ profiles were calculated from the integration (eqn. (4.30)) of the $\rho(z)$ distributions which are shown in fig. 4.22. On the other hand, the electric field due to dipoles distribution (fig. 4.26) is calculated by solving for $E_p(z)$ in eqn. (4.31).

4.1.8 Photo-stimulated discharge (PSD)

Samples were charged and/or poled using the contacting electrodes and corona discharge methods. The aim is to learn more about deep charge traps. This can be achieved using the photo-stimulated discharge (PSD). Experiments on samples charged and/or poled with contaction electrodes were performed under vacuum at different temperatures. The charge and dipole profiles were monitored *in situ* by means of LIMM. Additionally, experiments on samples charged with corona discharge method were performed at room temperature. Here, the PPS method was employed to determine the charge density profile.

Experiments under vacuum

PSD spectroscopy was performed from 400 nm to 200 nm. Since the light intensity of the Xe lamp varies as a function of the wavelength, the photocurrent was divided by the light intensity in order to calibrate the PSD spectra. In the following the results of the photo-stimulated discharge of PETP are shown. Some of the experimental results shown in this subsection are results already reported by Camacho González *et al.* (2004). Since the charge profiles in fig. 4.22 are large compared to some of the changes produced by the photo-stimulated discharge, the derivatives of the distribution functions $g'(z)$ are plotted instead of the charge profile $\rho(z)$. In the case of samples charged at -100 °C, $\rho(z)$ can be directly plotted.

The calibrated PSD spectra of freshly-charged films are shown in fig. 4.27. All of them show the presence of peaks at 300 and 270 nm. A third peak located at 240 nm only appears in samples that were irradiated with light during charging. Fig. 4.29(a) shows the PSD-spectrum of a freshly-charged sample with gold electrodes. These samples show the peaks at 240 and 300 nm, but not at 270 nm.

More in detail, the PSD spectra and the charge profiles of the samples charged at $T_c = -100$ °C, and the derivatives of the distribution functions ($g'(z) = (dg(z)/dz)/(\alpha_\varepsilon - \alpha_z)$) of the samples charged at $T_c = -50$ and 110 °C are shown in figures 4.28, 4.29, and 4.30, respectively. PSD spectra and $g'(z)$ of another sample charged at 110 °C are shown in fig. 4.31. As this sample was charged without irradiation, the main electric signal is due to dipole orientation.
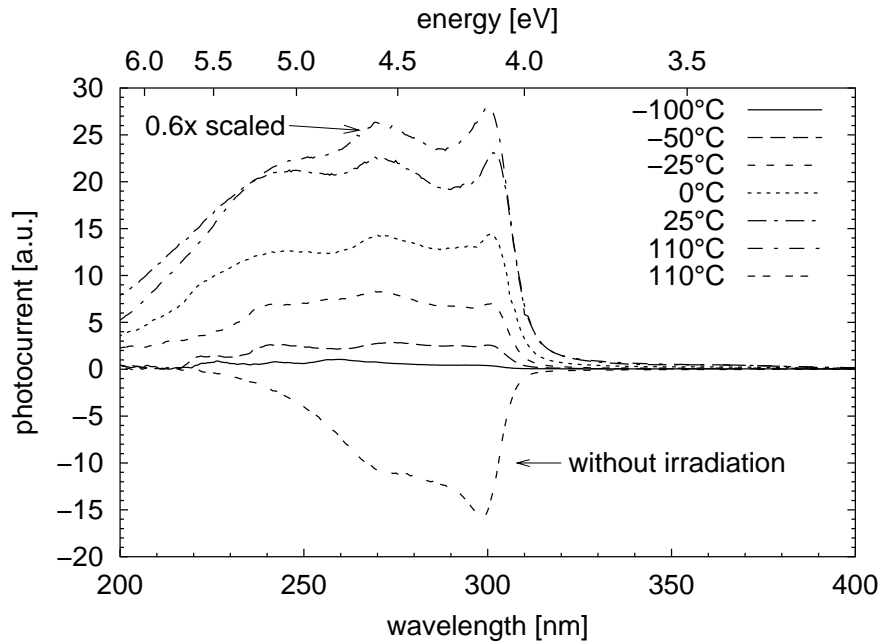
Figure 4.27: Calibrated PSD spectra of freshly charged PETP films (Cu electrodes) at different temperatures. $V = -600$ V, $t = 30$ min. During charging, the samples were irradiated at $\lambda = 305$ nm, except where indicated otherwise.

In general, the proposed charge profile of freshly charged samples exhibit a charge-density peak at approx. 1 μm (fig. 4.22). The bimodal peak observed in the $g'(z)$ distribution of samples irradiated while charging at temperatures $T_c \gtrsim -50\,°$C could be due to the effect of dipoles together with the stored charge, as explained in in the *second approach* of section 4.1.7.

After light irradiation around 300 nm (297 nm at $-100\,°$C, 301 nm at -50 and $110\,°$C) for 30 min, the photocurrent peaks at 300 nm decreases and exhibits a shift to longer wavelengths. The peak at 270 nm decreases strongly at $-100\,°$C (fig. 4.28(a)) and completely disappears in the other samples. The peak at 240 nm decreases, but remains visible in all PSD spectra. On the other hand, samples which were not irradiated while charging (fig. 4.31(a)) exhibit a sign reversal of the photocurrent after irradiation at 299 nm. The sign reversal of the photocurrent is predicted by the electric field in the sample (fig. 4.32). After the first irradiation, the electric field decreases and even changes its polarity, giving rise to a change in the photocurrent direction.

Further irradiation around 305 nm for 30 min (figs. 4.28(a), 4.29(a), 4.30(a), and 4.31(a)) almost completely bleaches the photocurrent peak at that wavelength (302 nm at $-100\,°$C, 304 nm at $-50\,°$C, 306 and 307 nm at $110\,°$C), but changes the peak at 240 nm only slightly.

The changes in the PSD spectra upon irradiation are accompanied by modifications of the density profiles. Near the surface ($z \approx 1$ μm), the peak is reduced in height (figs. 4.28(b), 4.30(b), and 4.31(b)), or even reverses its sign (fig. 4.29(b)). Deeper inside the sample, a smaller, but still significant depletion of the charge density is observed. This sign rever-
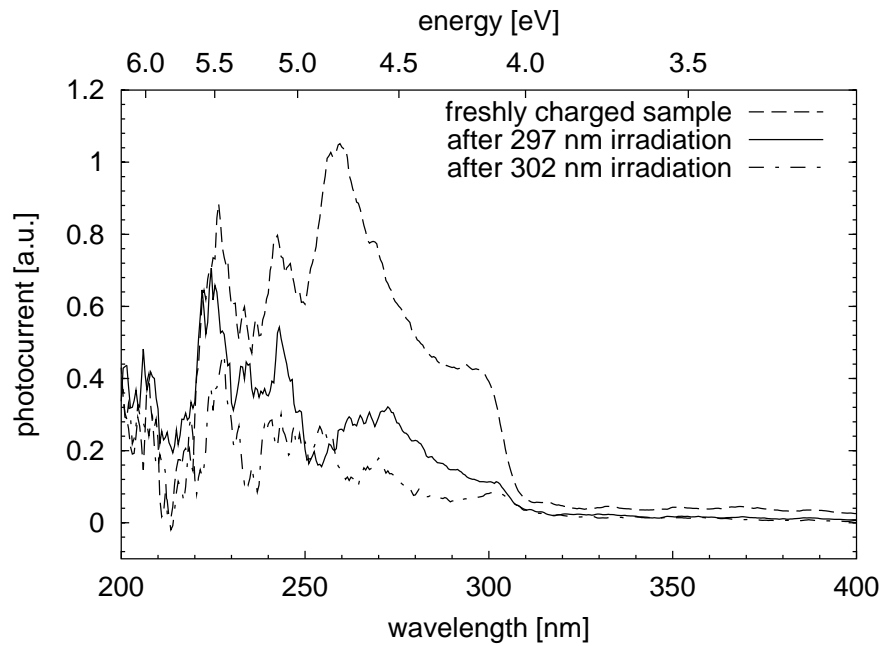
(a) Calibrated PSD spectra
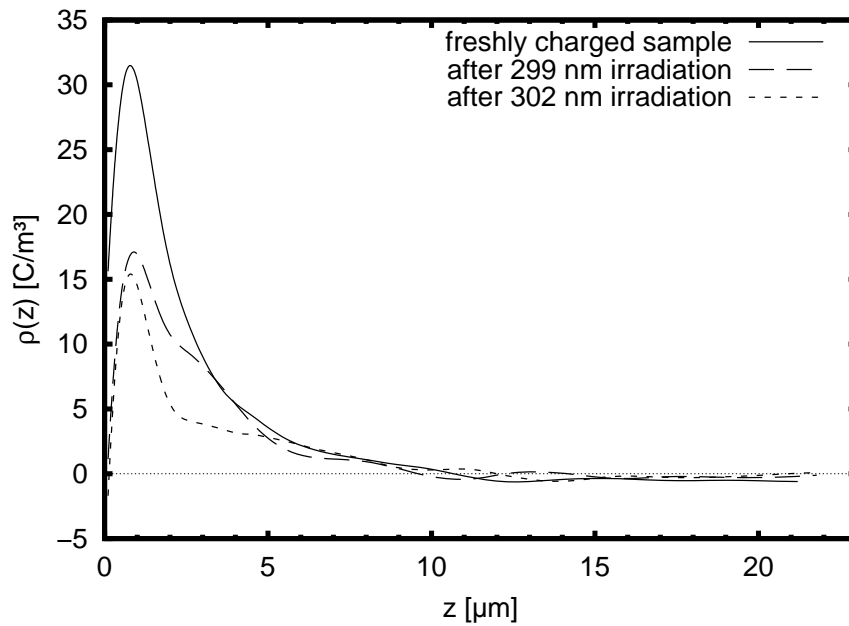
(b) Charge profiles

Figure 4.28: Photocurrent (a) and space charge density (b) in a PETP film ($d = 23$ μm) charged at $T_c = -100$ °C, $V = -600$ V, $t = 30$ min, $\lambda = 305$ nm. Irradiation time for photocurrent decay at (297 and 302)±2 nm was 30 min.
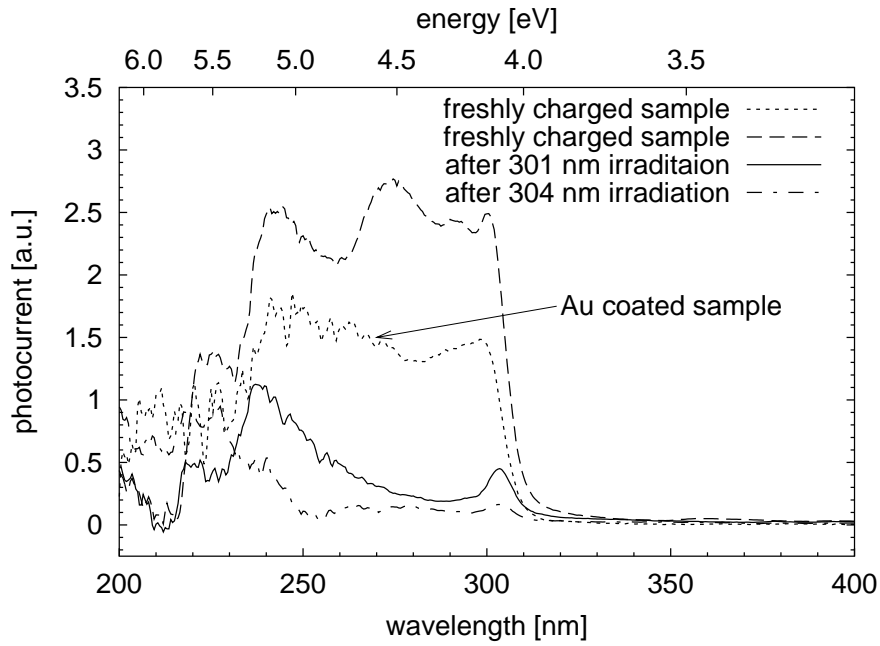
(a) Calibrated PSD spectra of a sample coated with copper electrodes and a calibrated PSD-spectrum of a freshly-charged sample coated with gold electrodes
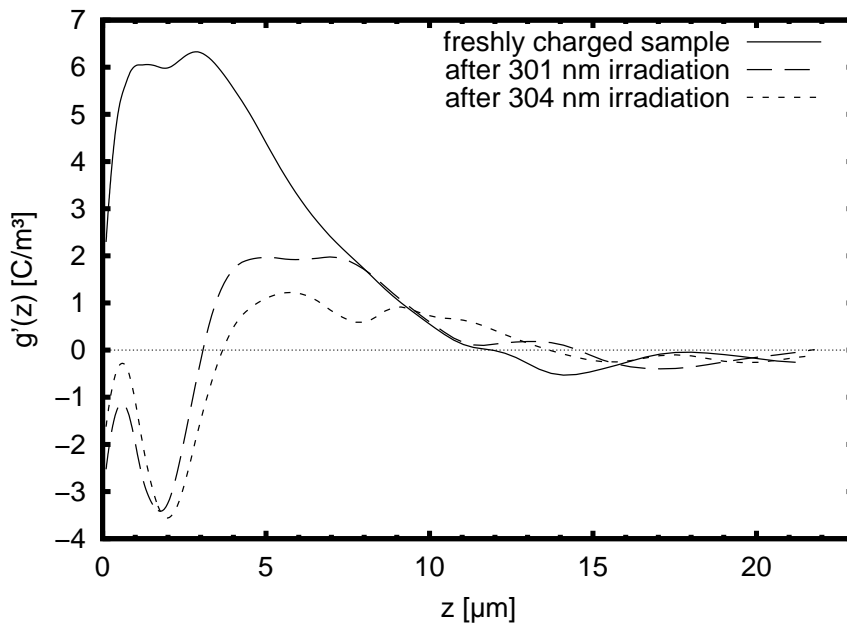
(b) Density profiles (derivatives of the distribution functions $g'(z) = (dg(z)/dz)/(\alpha_\varepsilon - \alpha_z)$)

Figure 4.29: Photocurrent (a) and density profiles $g'(z)$ (b) in a PETP film ($d = 23$ μm) charged at $T = -50$ °C, $V = -600$ V, $t = 30$ min, $\lambda = 305$ nm. Irradiation time for photocurrent decay at $(301$ and $304)\pm 2$ nm was 30 min.
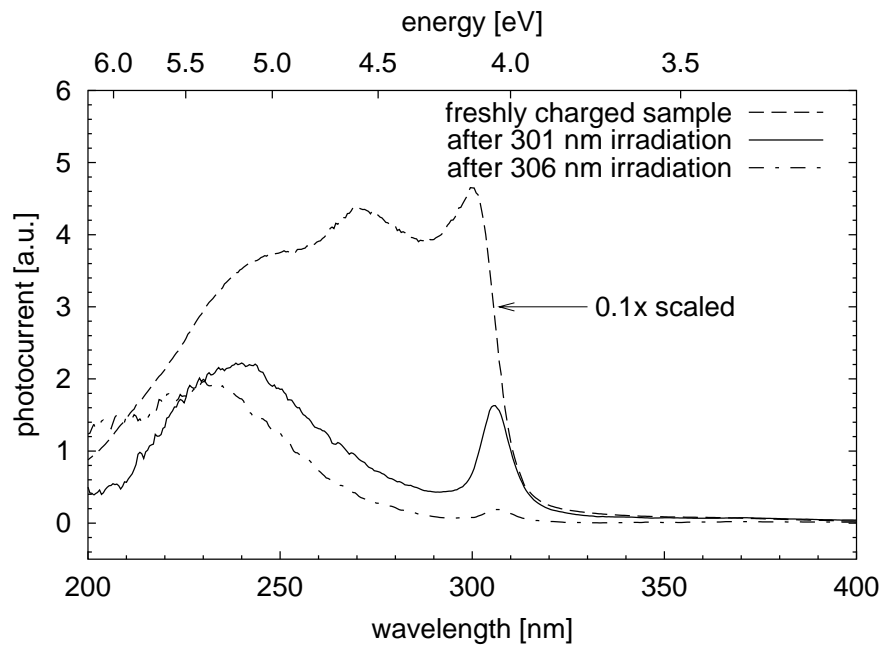
(a) Calibrated PSD spectra
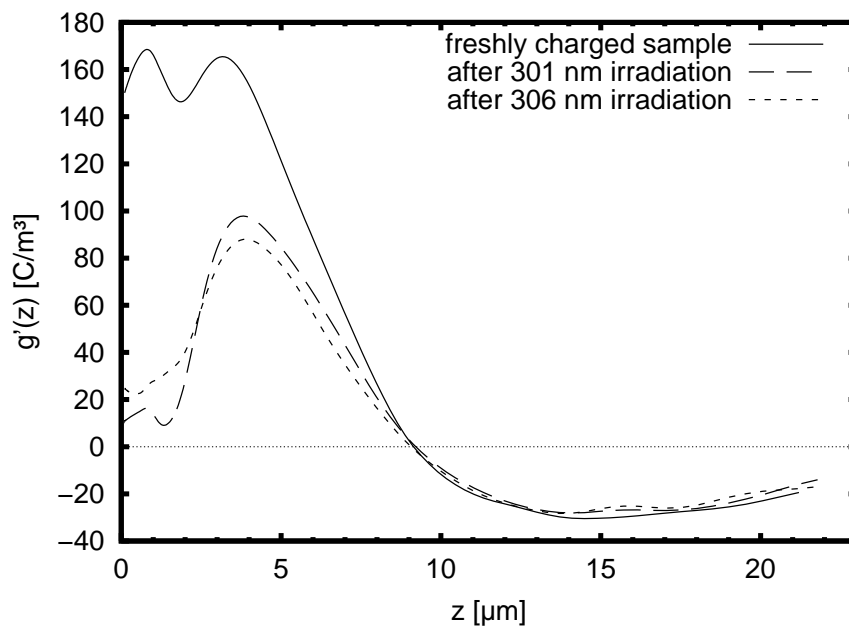
(b) Density profiles (derivatives of the distribution functions $g'(z) = (dg(z)/dz)/(\alpha_\varepsilon - \alpha_z)$)

Figure 4.30: Photocurrent (a) and density profiles $g'(z)$ (b) in a PETP film ($d = 23$ μm) charged and poled at $T = 110\,°C$, $V = -600$ V, $t = 30$ min, $\lambda = 305$ nm. Irradiation time for photocurrent decay at (301 and 306)±2 nm was 30 min.
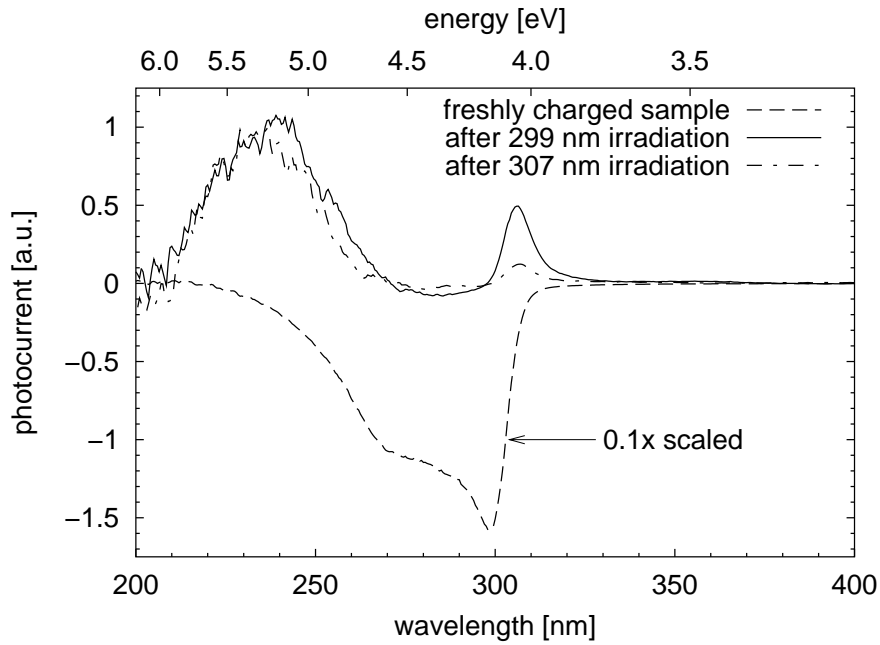
(a) Calibrated PSD spectra
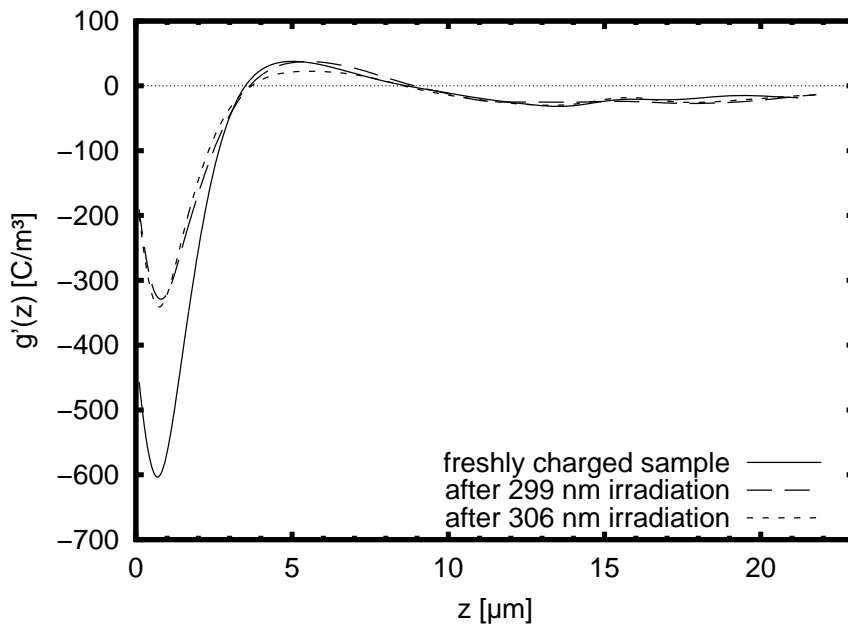
(b) Density profiles (derivatives of the distribution functions $g'(z) = (dg(z)/dz)/(\alpha_\varepsilon - \alpha_z)$)

Figure 4.31: Photocurrent (a) and density profile $g'(z)$ (b) in a PETP film ($d = 23$ μm) poled at $T = 110\,°C$, $V = -600$ V, $t = 30$ min. Irradiation time of the photocurrent decay at (299 and 307)± 2 nm was 30 min.
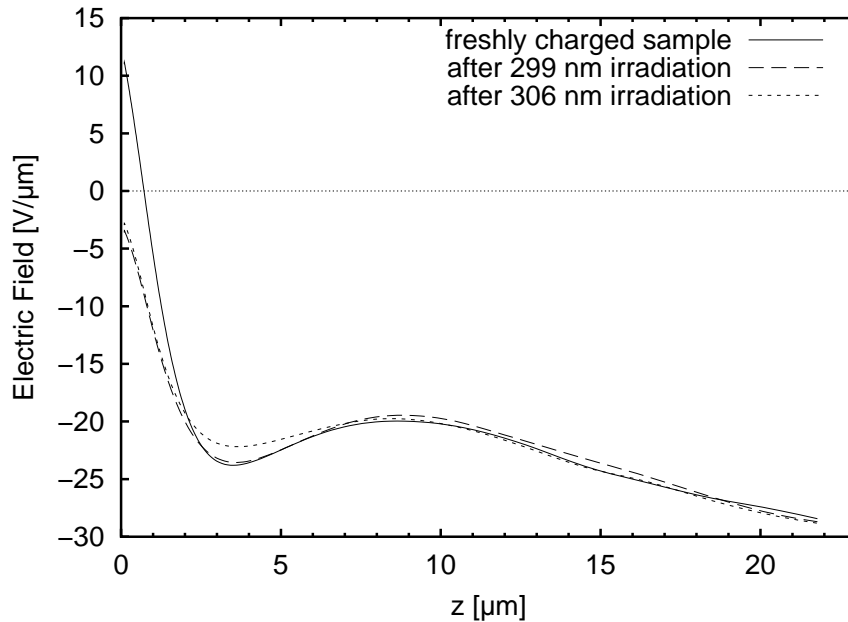
Figure 4.32: Electric field of a PETP sample ($d = 23$ µm) poled at $T = 110$ °C, $V = -600$ V, $t = 30$ min. Irradiation time of the photocurrent decay at (299 and 307)± 2 nm was 30 min.

sal of the $g'(z)$ distributions gives some support to the hypothesis that the bimodal peak density distributions observed in section 4.1.7 are not artifact.

Upon the second irradiation, the charge density profile around $z = 3$ µm in fig. 4.28(b) is reduced significantly, due to the deeper light penetration at 302 nm compared to that one at 297 nm. For samples charged at -50 °C (4.29(b)), the negative peak shifts deeper into the sample and the plateau becomes a broad peak with its maximum at 6 µm. In the case of samples charged at 110 °C (fig. 4.30(b)), the density profile shows a decrease of the excess of charge at 3 µm, but an increase at the irradiated surface of the sample. This change of the density profile indicates that the positive carriers can migrate to the front electrode. In contrast, the density profile of the sample with oriented dipoles (fig. 4.31(b)) shows a slight change after the second irradiation. The slight change could be due to the fact that the charges injected at the near electrodes are removed.

Two of the observed PSD peaks (at 300 and 240 nm) coincide with the optical absorption spectrum of PETP, while the maximum near 270 nm appears to be related to the Cu front electrode, since it does not appear in PSD spectra taken with gold-coated PETP films (fig. 4.29(a)). The photocurrent peak at 300 nm in the PSD-spectra (figs. 4.28(a), 4.29(a) and 4.30(a)) indicates the presence of a trap-charge level at approx. 4.1 eV. This assumption is confirmed by the change in the density profiles observed in figs. 4.28(b), 4.29(b) and 4.30(b) measured with help of LIMM technique.
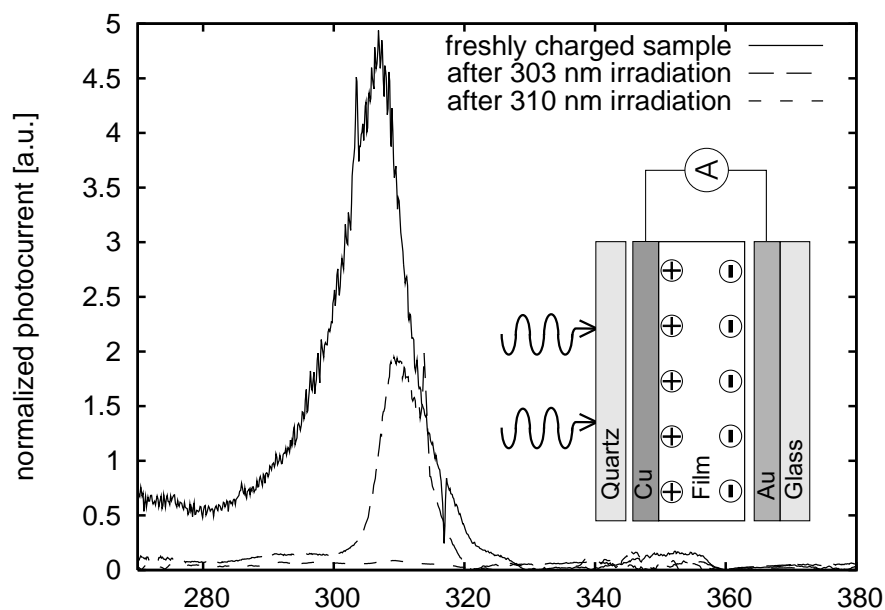
(a) Calibrated PSD spectra of a corona charged sample. *Inset*: Sample arrangement.
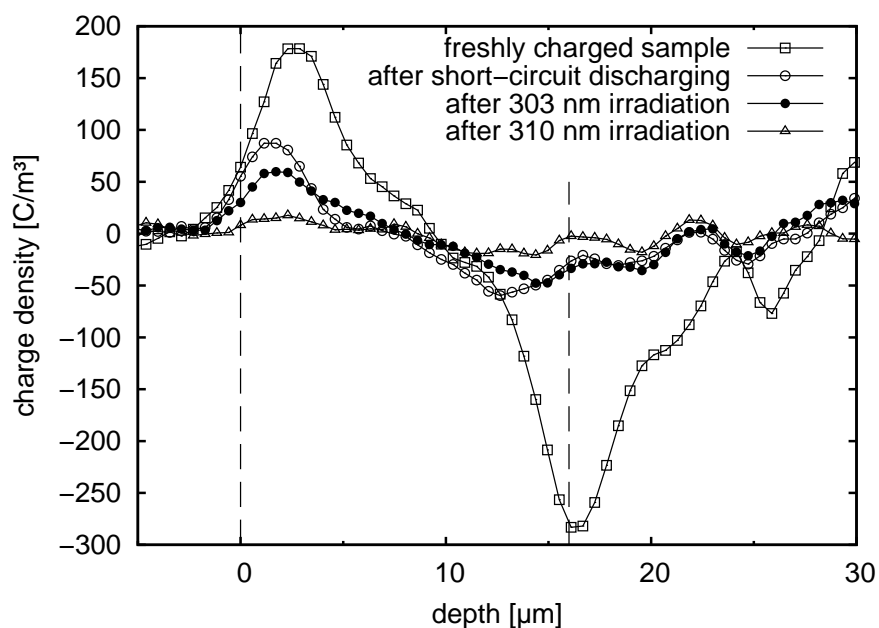
(b) Charge profile measured with PPS-technique from Mellinger *et al.* (2004a).

Figure 4.33: Photocurrent (a) and charge density (b) in a PETP film ($d = 16 \,\mu\mathrm{m}$). Charged with corona discharge: $-12 \,\mathrm{kV}$ needle voltage, 5 min, at room temperature. Irradiation time for the photocurrent decay at (303 and 310)± 4 nm was 15 min (Camacho González *et al.*, 2002; Mellinger *et al.*, 2004a).

Table 4.2: Trap energies (in eV) determined with PSD in comparison to optical absorption spectroscopy. a) Camacho González *et al.* (2004), b) Camacho González *et al.* (2002); Mellinger *et al.* (2004a) c) Ouchi (1983), d) Lazare *et al.* (1987), e) Kaito *et al.* (1988) and f) LaFemina and Arjavalingam (1991)

PSD peaks observed	a)	4.1	5.2
	b)	4.0	–
Optical absorption:			
Absorption spectroscopy	c)	4.1	5.1
	d)	4.2	5.1
	e)	4.3	5.1
Theoretical calculation	f)	4.19	4.88

Experiments on corona-charged samples

Experiments performed on samples charged with corona discharge method show similar results to the experiments performed in vacuum (fig. 4.33). The experimental results presented in this subsection were already reported in Camacho González *et al.* (2002) and Mellinger *et al.* (2002, 2004a). A PETP film (16 μm thickness) was coated with copper on one side of the film. The sample was charged with the corona discharge technique at the non-electroded side, with a needle voltage of -12 kV for 5 min at room temperature. To perform the PSD experiments, the sample was sandwiched between a clear quartz plate and a gold-coated glass plate. The side coated with the copper electrode faced the monochromatic light, as shown in the inset of fig. 4.33(a).

The PSD-spectra show a photocurrent peak at 303 nm. After light-irradiation for 30 min at 303 nm, the photocurrent peak decreases. A further irradiation at 310 nm for 30 min bleaches the photocurrent peak. The charge profiles measured with help of the PPS-technique show that the charge density decreases after each light-irradiation (fig. 4.33(b)). The bleaching of the photocurrent peak at 300 nm accompanied with the decrease of the charge density indicates a probable charge trap level at approx. 4 eV. This agrees with the results observed with the samples charged with contacting electrodes at different temperatures.

The PSD-spectra and the optical absorption spectrum

The trap energy level at 4.1 eV of the PSD spectra coincides with the optical absorption at 300 nm. This absorption peak is derived from the $^1A_{1g} \rightarrow\,^1 B_{2u}(^1L_b)$ benzene transition (LaFemina and Arjavalingam (1991); Ouchi (1983), see sec. 3.3.1). This may indicate that this trap level could be related to the aromatic group of the polymer chain.

On the other hand, the bleaching of the photocurrent peak at 240 nm was not successful. The PETP films present a strong light absorption at this wavelength (see sec. 3.3.1). In
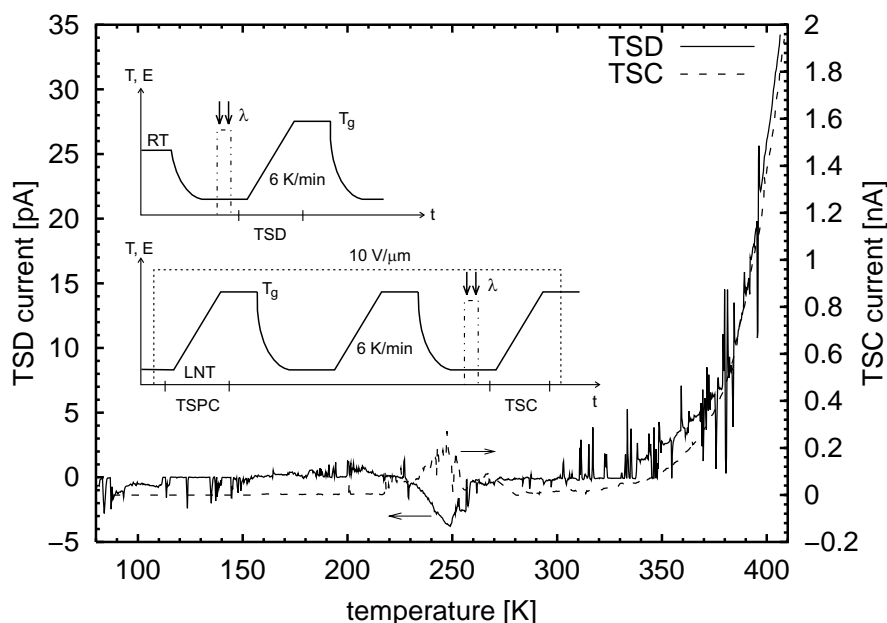
Figure 4.34: Thermally stimulated current (TSC) and discharge (TSD) signal of a DANS-doped TOPAS® 6013 film. The inset shows the charging/discharging procedure. UV-irradiation was performed at 338 nm where indicated. RT: room temperature, LNT: liquid nitrogen temperature (77 K). Prior to the initial TSD scan, the film was corona-charged (Mellinger *et al.*, 2004b).

this case, the charge profile is not appreciably affected in the bulk. Nevertheless, due to its proximity to the optical absorption at 243 nm derived from the $^1A_{1g} \rightarrow {}^1B_{2u}(^1L_a)$ benzene transition (LaFemina and Arjavalingam, 1991; Ouchi, 1983), it seems possible that this trap level (5.2 eV) is also associated with the aromatic groups of PETP. A list of the observed trap energies in comparison to theoretical calculations and optical absorption measurements is shown in table 4.2.

4.2 Cyclic Olefin Copolymers

In contrast to PETP, Cyclic Olefin Copolymers (COC) do not contain molecular dipoles in their chemical structure (fig. 3.10) and exhibit a low permittivity. A plane COC film was drop-casted onto a stainless steel substrate (see sec. 3.4). The film was annealed and separated from the substrate to evaporate electrodes on both sides of the film to perform the dielectric spectroscopy. The measurement shows an even spectrum, with low permittivity ($\varepsilon' \approx 2.57$) and losses ($\varepsilon'' \approx 0.0025$) at 10 Hz and 100 kHz. TSC-thermograms (fig. 4.34) also show the absence of the dipolar phenomena. Sessler *et al.* (1997) concluded that the electret properties are entirely due to real charges. This behavior was also reported by Mellinger *et al.* (2004b).
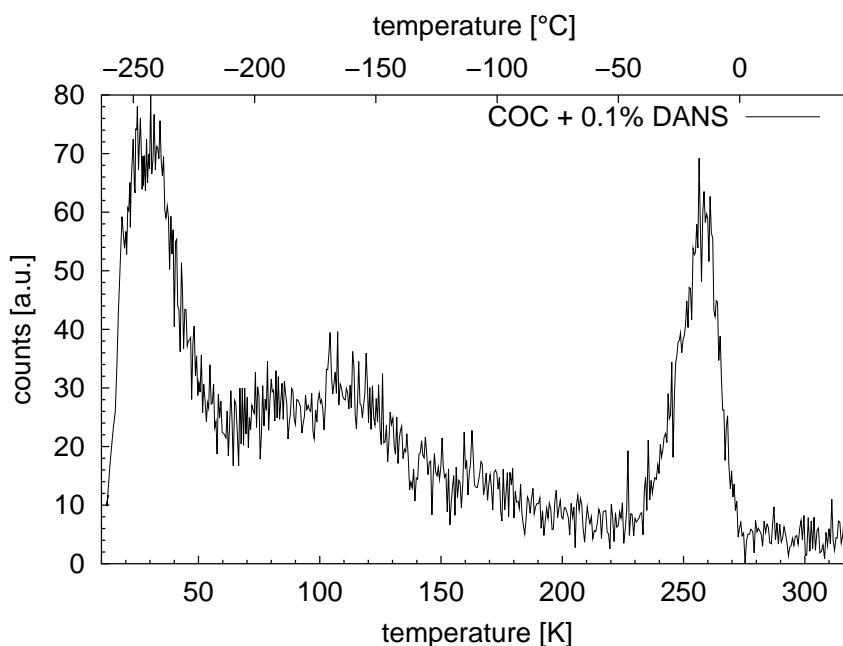
Figure 4.35: Thermoluminescence (TL) of DANS doped COC (TOPAS® 6013) film.

This material is also highly transparent (fig 3.11). Extrinsic photo-electrets can be achieved with the use of COC-based composites. Chromophores such as pyrene and DANS[1] are embedded in the COC polymer matrix to probe changes in the electric field at a molecular level. This gives the possibility to obtain a TL-signal, which the clear COC samples do not produce.

A corona-charged DANS-doped COC (TOPAS® 6013, Ticona) film was irradiated with broad-band light ($334 - 507$ nm) at 77 K for 10 min (see the inset in Fig. 4.34). The thermally stimulated discharge or depolarization (TSD) measurement at 6 K/min shows a peak near 250 K (≈ -23 °C) with an apparent activation energy of approx. 0.6 eV. The method proposed by McKeever and Hughes (1975) was introduced in order to distinguish between dipole and charge-carrier processes (see sec. 3.2.1). The experimental procedure is depicted in the inset of the fig. 4.34. Four thermal cycles were performed. The first cycle was a thermally stimulated discharge (TSD) measurement at 6 K/min. The TSD thermogram shows a peak near 250 K (≈ -23 °C). Then, three more cycles were performed. A thermally stimulated poling current (TSPC) measurement was performed at 6 K/min. The TSPC signal does not show any current peak. After the TSPC, a "zero"- or "cleaning"-cycle was performed. Then, a thermally stimulated current (TSC) measurement was performed at 6 K/min. The TSC shows a peak near 250 K (≈ -23 °C), which is also present in the TSD thermogram.

A thermoluminescence (TL) measurement performed at 6 K/min on a DANS-doped COC (TOPAS® 8007) film is shown in fig. 4.35. This sample was irradiated at 7 K (≈ -266 °C) with a broad-band light ($300 - 520$ nm). The TL-thermogram exhibits three

---

[1]4-dimethylamino-4'-nitrostilbene (sec. 3.4)
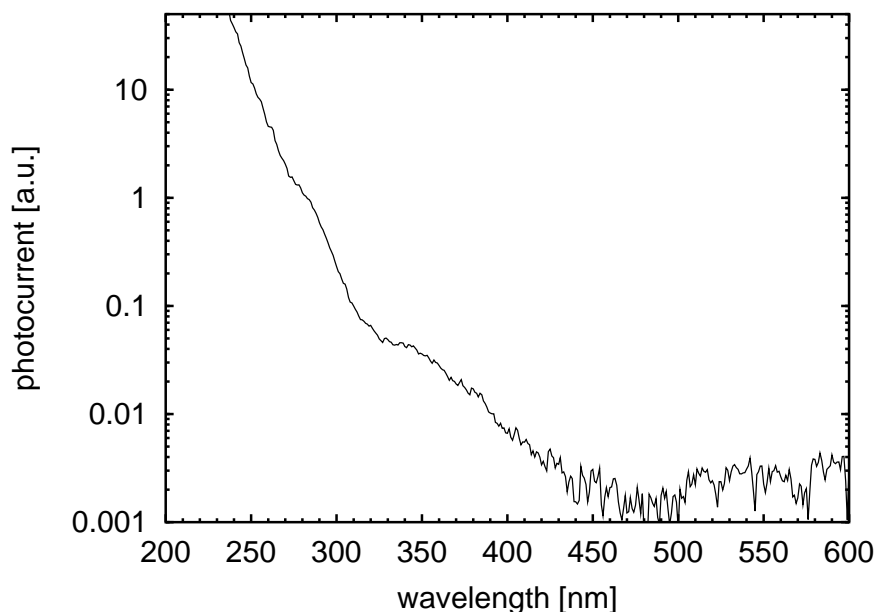
Figure 4.36: Photostimulated discharge spectrum of pyrene-doped TOPAS® 8007. The photocurrent has been normalized with the UV intensity (Mellinger *et al.*, 2004b).

peaks at 20 K (≈ -253 °C), 100 K (≈ -173 °C) and 250 K (≈ -23 °C). From the thermograms in fig. 4.34, it can be concluded that the TL-peaks in the thermograms are due to charge-carriers processes with an apparent activation energy of ≈ 0.11 eV at the peak near 250 K (-23 °C).

For a pyrene doped COC (TOPAS® 8007) sample (Fig. 4.36), the photo-stimulated discharge spectrum shows a plateau near 350 nm and a strong rise towards shorter wavelengths, starting at 310 nm, with a small change in the slope near 270 nm. These wavelengths (350 and 270 nm) coincide with the absorption spectrum of the dye (Pyrene) in the sample, as it can be observed in fig. 3.11. These changes in the slope of the rising current are not present in samples without dyes.

Prolonged light irradiation at 300 nm shows a strong charge decay at the near electrode ($z \leq 1$ µm) as shown in figs. 4.37 and 4.38, while irradiation at shorter wavelengths has little effect on the charge decay (fig. 4.38). Deeper in the sample ($z > 2$µm), the charge profile is unaffected after irradiation as shown in fig. 4.37. Mellinger *et al.* (2004b) concluded that this effect is related to the photo-induced detrapping of charges from traps at 4 eV (300 nm).
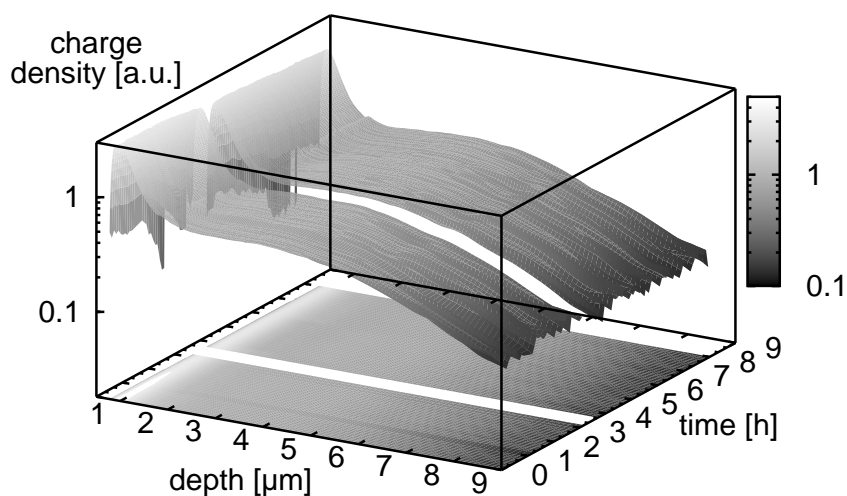
Figure 4.37: Time-evolution of the charge profile of a corona-charged pyrene doped COC (TOPAS® 8007) film during irradiation at 300, 280, and 260 nm. For time decay details see fig. 4.38 (Mellinger *et al.*, 2004b).
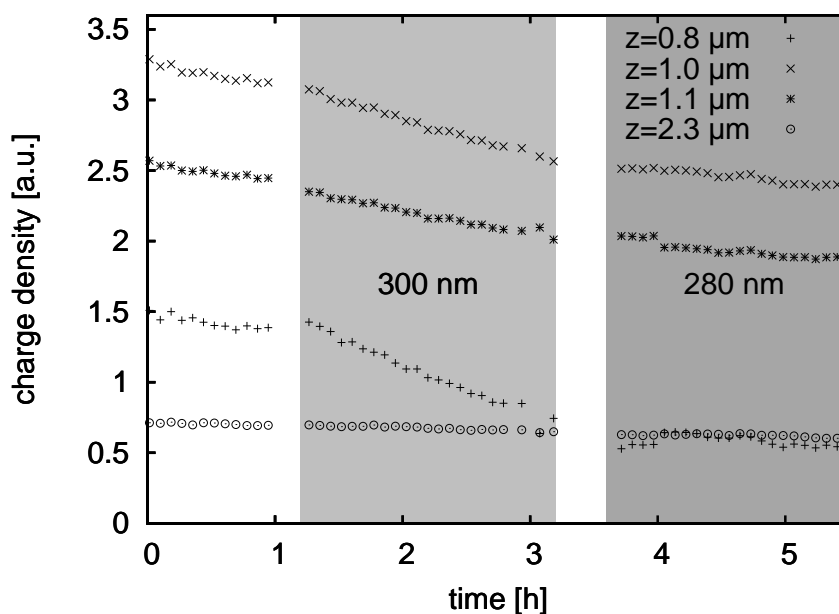
Figure 4.38: Time-evolution of the charge density at several depths (z) in a corona-charged COC (TOPAS® 8007) film during UV irradiation (presented at the *CEIDP* conference on October the 20th, 2004 from Mellinger *et al.* (2004b)).

4.3 Probable mechanisms of charge detrapping

4.3.1 Thermally stimulated process

It is known that the polymer chains are a dynamic system (Doi and Edwards, 1988). The physical properties of the polymeric electrets rise from the molecular motions as chain conformations change, side groups shake, polymer chain reptation and motion of crystallite features (Das–Gupta, 2001). These motions are temperature dependent and influence the dielectric behavior, charge transport and charge storage properties (Das–Gupta, 2001; Dobruchowska *et al.*, 2004). Even though the thermal process is not directly related to the charge traps, this process can ease the detrapping and/or transport of the charge carriers. In this sense, it is possible to say that the molecular relaxation related to the ethylene groups is necessary to activate the thermoluminescence glow and thermally-stimulated current peaks.

As mentioned in section 4.1.1, the β-relaxation is composed of three or maybe four sub-relaxations. Illers and Breuer (1963) associated the β_1-relaxation to the movement of the carboxyl groups ($>C = O$) and the β_2 process to the ethylenic linkage ($-(CH_2)_2-$) of PETP. The activation energies of these two relaxations calculated from Sachez (1968) are about 0.74 ± 0.06 and 0.34 ± 0.06 eV for the β_1- and β_2-relaxations, respectively. It was observed in section 4.1.2 that the thermo-current and the TL-glow peaks at 0 °C (273 K) are due to charge carriers (fig. 4.5). This suggests the presence of energy traps at 0.36 eV which are activated by the movements of ethylenic linkages.

This assumption does not necessarily indicate that the charge-trap is located at the ethylene group, but it can be activated with this relaxation process. The charge traps could be located at inert chemical impurities and/or amorphous-crystalline interfaces which can be stimulated with the movement of the polymer chain (sec. 2.1.3). On the other hand, at lower temperatures ($T < 0$ °C) thermally-stimulated currents are related to the motion of the molecular dipoles, which are also the origin of the TL-glow peak at -140 °C (sec. 4.1.2). Takai *et al.* (1978c) reported trap levels at $0.23-0.50$ eV with a detrapping process enhanced by the molecular motion of the ester groups $-COO-$. However, the molecular models indicate that no local dipole orientations are possible without the cooperative movement of the adjoining segments (Sachez, 1968).

At higher temperatures, the thermal conduction process is eased by the molecular movements of the polymer (α-relaxation). TL-thermograms at high temperatures (around T_g) show radiative charge recombination (fig. 4.6). This detrapping and recombination is eased by the movement of the polymer chains which are responsible of the α-relaxation around 120 °C. On the other hand, the dielectric spectra show a main α-relaxation peak with a shoulder around 75 °C (figs. 4.1 and 4.2). In sec. 4.1.1, this behavior was attributed to the effect of the amorphous and crystalline phases. In that sense, the charge detrapping and recombination detected in the TL-thermograms around and beyond the T_g are not only due to the movement of the chains in the amorphous region, but also due to the movement of the crystallites as a whole entity.

Additionally, the peaks located at 0 °C (273 K) and 110 °C (383 K) in the TL-thermograms of PETP (fig.4.6) have an apparent activation energy of ≈ 0.36 eV. One can speculate, that

the mechanism of detrapping could be the same. That means that the movements of the ethylenic linkages could be responsible of the charge detrapping in both cases.

Extrinsic photoelectrets based on COC-composites generate a peak in the TL- and TSC-thermograms at -23 °C (250 K) with apparent activation energies of ≈ 0.11 and 0.6 eV, respectively. Since the electret behavior comes from charge storage, it is possible to say that this complexes contain charge traps with energy levels from 0.11 to 0.6 eV. Since plane COC films did not show these peaks, it is probable that these trap levels are located at the interface polymer matrix and dye molecules. However, the distribution of the dyes in the matrix can lead to a change in the interaction between them. If the concentration is high enough to form agglomeration of dyes in the matrix, this leads to thermograms rising from the crystalline-chromophore regions instead of the matrix.

4.3.2 Photodetrapping

Photoeffect

Photocurrent peaks in PSD spectra can be related to the photoemission process. The external photo-effect is one of these processes. Mellinger *et al.* (2004a) showed that the external photo-effect is present in samples with pressed-on electrodes. PTFE films were corona charged and sandwiched between gold and aluminum electrodes. This arrangement generated gaps between the electrodes and the polymer film. The thresholds for the onset of the photocurrent depend on the work function of the metal electrodes. From that, it was concluded that the external photoeffect must be taken into consideration only when pressed-on electrodes are used.

Sapieha and Wintle (1977) measured photocurrents injected into PETP from evaporated aluminum electrodes (internal photoemission) in the wavelength range 475-300 nm. Internal photoemission has also been observed in PSD-spectra. Figure 4.29(a) shows the normalized PSD spectra of copper- and gold-coated samples. In contrast to copper-coated samples, the gold-coated samples present two PSD-peaks at 300 and 240 nm, 4.1 and 5.2 eV respectively. The peak at 240 nm not only coincides with the optical absorption-peak of PETP (tab. 4.2), but also with the work function of gold 243 nm (5.1 eV). In freshly charged PETP samples, the photo-injection effect is clearly present in the PSD-spectra, due to the charge density peak near the electrode at $z \approx 1$ µm (fig. 4.20). After the first PSD-decay, the charge at the near electrode decreases (sec. 4.1.8) and the photo-injection effect is strongly reduced in the PSD-spectra.

Photo-detrapping in the bulk

Cyclic Olefin Copolymers (COC) are highly transparent materials (sec. 3.3.2). The addition of chromophores in the COC matrices generates an extrinsic photoelectret (sec. 3.4). In these kinds of systems, the PSD-spectra show photocurrent peaks which coincide with the absorption peaks of the spectrum due to the dopants (sec. 4.2). PSD-decay experiments show the presence of a charge-trap level at 4 eV (310 nm). The low efficiency of
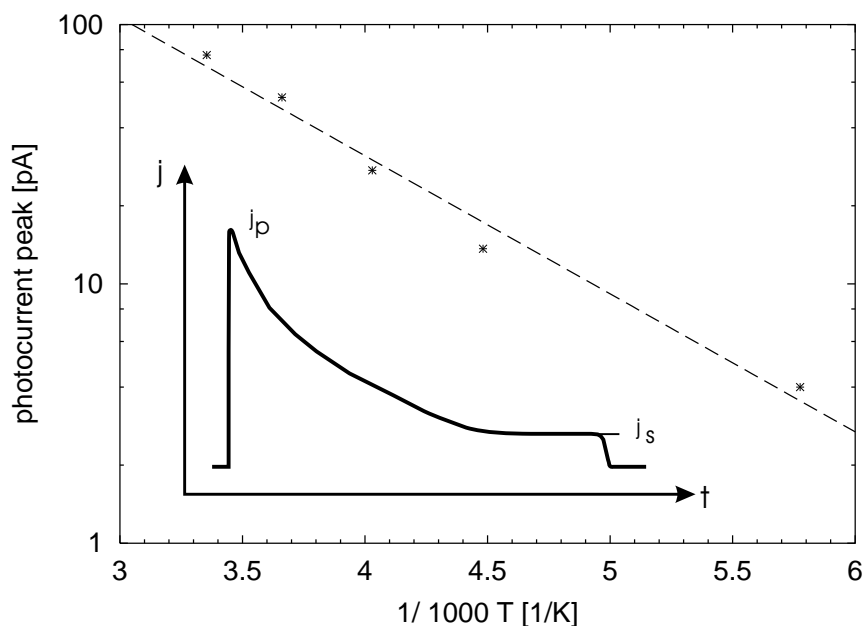
Figure 4.39: Temperature dependence of the transient photo-current peak (j_p) when PETP samples are charged with the contacting electrodes method. $E = 26$ μm, $\lambda = 305$ nm at $T_c = -100, -50, -25, 0, 25$ °C. *Inset,* scheme of the transient photo-current peak. j_p is the photo-current peak maximum when the UV-light is switched on. j_s is the stable photocurrent.

detrapping in the bulk after irradiation was explained by the fast retrapping (Mellinger *et al.*, 2004b). The electric field calculated from piezoelectrically pressure step generated method (PPS) is about 7 V/μm. The initial separation, to have a 70 % probability to escape geminate recombination, is ≈ 11 nm under the effect of this voltage (Onsager, 1938). A rough estimate of the number of molecules of Pyrene homogeneously distributed in the COC matrix yields a concentration of 3×10^{25} particles/m³. If it is considered that the particles are in the center of a spheric volume of radius r, the average distance between two pyrene particles is about 4 nm. This relatively high density of chromophores explains the fast retrapping phenomenon assumed by Mellinger *et al.* (2004b).

Photo-exciton generation is another probability of charge detrapping. Direct or indirect detrapping processes can happen. The charge generation in PETP has already been identified together with the photoconduction (chapter 1). It was shown that the photocurrent is also due to the photo-carrier generation in the benzene rings of PETP (Takai *et al.*, 1976; Ieda *et al.*, 1977; Takai *et al.*, 1977c,b).

Ieda *et al.* (1977) reported two photo-stimulated current peaks at 300 and 260 nm. Takai *et al.* (1976) associated these photocurrent peaks to the $\pi\pi^*$ benzene transitions. In our case, the presence of the peak at 300 nm was identified also by photo-stimulated current experiments, but the peak at shorter wavelengths was located at 240 nm instead of at 260 nm (sec. 4.1.8).

Batt *et al.* (1968) indicated that the intrinsic photogeneration of free carriers requires an experimental detectable activation energy. Photoconduction results from our experiments were employed to calculate this activation energy. The photoconduction experiments performed at 305 nm and 26 V/µm show a transient peak (inset fig. 4.39). These transient peaks have maxima J_p at approx. 8 to 12 s after starting the irradiation on the sample and a stable photocurrent J_s after 30 min. Contrary to the J_s, J_p depends on the temperature. Figure 4.39 shows that J_p follows the Arrhenius' law with an activation energy of 0.106 eV (1.698×10^{-20} J). Using this activation energy in the approximation proposed by Batt *et al.* (1968), it was possible to calculate a pair thermalization length for pair separation against the Coulomb field $r_o \approx 4$ nm (see appendix A for more details).

Additionally, simulations using Onsager's theory (Onsager, 1938) were performed to calculate the necessary distance to obtain a 70% probability for charge separation with an electric field $E = 26$ V/µm at temperatures from -100 to 25 °C. These simulations yield a distance of approx. 4.5 to 4.7 nm, which agrees with the one calculated using the activation energy. These results agree with the ones given by Takai *et al.* (1978b). They performed experiments on field quenching of thermoluminescence (TL) from photoexcited PETP films. Additionally, they calculated a mean separation r_o of 5 to 6 nm with an applied electric field of 23 V/µm. Also, jump distances of 8 to 20 nm were calculated by Seanor (1982) using a field-assisted ion migration concept.

Auriemma *et al.* (1995) calculated using Monte Carlo simulations that a repeat unit (r.u.) is approx. 1 to 1.1 nm. That means that the calculated r_o is approx. 4 repeat units of PETP. The charge separation and storage were confirmed with the help of the of LIMM technique. Charge profiles of freshly charged samples (fig. 4.22) show that PETP is an intrinsic photo-electret. During light irradiation (sec. 4.1.8), several processes can happen which could affect the stored charge. These processes could be

- direct photon-charge interaction generating charge detrapping,

- photo-exciton generation which can interact with the stored charges,

- light generation by radiative recombination of free carriers which is absorbed and builds charge up or has direct photon-charge interaction,

- retrapping of the free carriers.

The photo-luminescence spectrum (fig. 3.9) shows emission from fluorescence at 335 and 385 nm and phosphorescence in several bands in the region $420 - 480$ nm (Teyssèdre *et al.* (2001), see sec. 3.3.1). This spectrum, which can be quenched due to the internal electric field, may indicate that the photo-detrapping of charge carriers observed in sec. 4.1.8 is an indirect process. This process consist of several steps:

1. exciton generation due to photon-absorption;

2. free charge carriers generation due to the exciton dissociation by the internal electric field;

3. annihilation or detrapping of the stored charge by the interaction with the generated free carriers.

However, the observed photo-stimulated charge detrapping can be a direct process of interaction between photon and stored charge. The PSD-spectra (see sec. 4.1.8) show that the photocurrent peak at 300 nm is shifted to longer wavelengths after the first photo-stimulated charge decay. Additionally, the photocurrent peak at 240 nm was not affected after photo-charge detrapping at 300 nm. This indicates that the observed photo-charge detrapping is a state-selective process and supports the theory of direct photon-charge interaction.

In that sense, table 4.2 shows the position of the peaks in the photocurrent and absorption spectra. The position of the photocurrent peaks in the PSD-spectra coincides with the optical absorption of the PETP. The absorption peaks are derived from the $^1A_{1g} \rightarrow^1 B_{2u}(^1L_b)$ and $^1A_{1g} \rightarrow\ ^1B_{2u}(^1L_a)$ benzene transition (LaFemina and Arjavalingam (1991); Ouchi (1983), see sec. 3.3.1). This indicates that the charge traps at 4.1 and 5.2 eV are associated to the aromatic groups in the polymer film.

4.4   Identification of the trapping sites

At this point it is possible to summarize the characteristics observed in the charge trapping and detrapping, and dipole orientation from the materials employed in this work. This information provides with a piece of the picture to describe the charge storage and detrapping mechanisms and to identify of the trapping sites. Additionally, to give an explanation of the long-term charge retentention.

Cyclic olefin copolymer:

o Structural characteristics (sec. 3.3.2):

- Saturated polymer (σ-bonds).

- Highly transparent (λ <200 nm).

- Addition of dyes to probe the internal electric field.

o Dipole and charge carrier behavior (sec. 4.2):

- Dielectric spectroscopy: $\varepsilon' \approx 2.57$, $\varepsilon'' \approx 0.0025$.

- Combination of TSP, TSPC and TSC: current peak at 250 K ($-23\,°$C) due to charge carriers (Mellinger *et al.*, 2004b).

o Shallow traps: 0.11 and 0.6 eV (sec. 4.2):

- TL: activation energy of the glow peak at 250 K ($-23\,°$C) approx. 0.11 eV.

- TSD: activation energy of the current peak at 250 K (-23 °C) approx. 0.6 eV.

o Deep traps: 4 eV (Mellinger *et al.*, 2004b):

- Combination of PSD and TP: photo-charge detrapping at 300 nm (4 eV)

Polyethylene terephthalate:

o Structural characteristics (sec. 3.3.1):

- Molecular dipole: $\rangle C = O$

- Chemical resonance between the $\rangle C = O$ and the benzene rings (Takai *et al.*, 1977b).

- *Trans*-configuration of the chain in the crystalline phase (Daubeny *et al.*, 1954).

- Strong light absorption ($\lambda < 310$ nm).

o Dipole and charge carrier behaviors:

- Dielectric spectroscopy (sec. 4.1.1):
    - β-relaxation (Illers and Breuer, 1963):
        * β_1-relaxation due to carboxyl groups $\rangle C = O$. Activation energy approx. 0.74 ± 0.06 eV (Sachez, 1968).
        * β_2-ralaxation due to ethylenic linkage ($-(CH_2)_2-$). Activation energy approx. 0.34 ± 0.06 eV (Sachez, 1968).
    - α-relaxation (sec. 4.1.1):
        * Loss peak (ε'') around 120 °C.
        * Shoulder due to the amorphous phase of the loss peak around 75 °C ($T_g = 79$ °C).

- Combination of TSP, TSPC and TSC (sec. 4.1.2):
    - Two thermo-current peaks due to dipoles. First, between -160 and -50 °C. Second, around 127 °C.
    - One thermo-current peak due to charge carriers at 0 °C.

- Combination of TL and TSC (sec. 4.1.2):
    - Three TL-glow peak due to dipole processes: at -140 °C, 120 °C and 160 °C.
    - TL-glow peak charge carrier processes: at 0 °C.

- Quasi-static pyroelectric measurement (QPM, sec. 4.1.6): Quasi-static pyroelectric coefficient (QPC) from unpoled sample ~ 0.6 nC/(m^{2}K) and poled sample ~ 60 nC/(m^{2}K).

- Combination of QPM and TSD (sec. 4.1.6): Charge-dipole interaction. Charges induce a QPC.

- PSC (sec. 4.3.2): $r_o \approx 4$ nm.

- Combination of TL and emission spectra (Padhye and Tamhane, 1978; Takai *et al.*, 1978c): Spectra from the TL-glow peaks agree with the photo-luminescence spectrum which is composed of excimer and monomer fluorescence and structured phosphorescence at wavelengths longer than 400 nm.

○ Shallow traps:

- Combination of TL and TSC (Camacho González *et al.*, 2005): Charge traps at approx. 0.36 eV. From the activation energy of the glow peak at 0 °C

- Combination of TL and dielectric spectroscopy (Camacho González *et al.*, 2005): The trap level is activated by the ethylenic linkage $(-(CH_2)_2-)$.

- Combination of TL and TSC (Takai *et al.*, 1978c): Charge traps at $0.23-0.50$ eV activated by the ester groups $-COO-$.

○ Deep traps:

- Combination of PSD, LIMM and PPS (Camacho González *et al.*, 2004): Charge traps at 4.1 and 5.2 eV.

- Combination of PSD and absorption spectrum (table 4.2): Charge traps related to the optical benzene transitions (Camacho González *et al.*, 2004). $^1A_{1g} \rightarrow \, ^1B_{2u}(^1L_b)$ at 4.1 eV and $^1A_{1g} \rightarrow \, ^1B_{2u}(^1L_a)$ at 5.1 eV.

- PSD (Takai *et al.*, 1977a): 2.3 eV.

One of the main questions that arises from these results is the difference in energies obtained with thermal- and optical-methods. In order to answer such a question, one should remember that a polymeric electret is a dynamic system (chapter 1). This system is stabilized by two kinds of forces acting intra- and inter-chains. The secondary forces (inter-chains) can generate energies between 0.02 to 0.87 eV. The primary forces (intra-chains) can generate energies between 2 to 8.6 eV. The variation of external factors, such as temperature, do effect a change on the polymeric system. Since energy levels of the charge traps depend on their environment in the polymer matrix, a change in the matrix affects this charge trap and even releases the charge.

A temperature change can provoke changes in the polymer matrix due to a molecular rearrangement, which can be gained with the secondary forces. This kind of phenomenon is observed in thermal techniques (sec. 3.2.1). These molecular rearrangements lead to dipole orientation and charge detrapping. On the other hand, when temperature is low $(T < T_g)$ and is kept constant, these rearrangements decrease. The polymer is a kind of *quasi-frozen* system. Under this circumstance, the excitation of the polymeric electret

with a light source provides us with information on the energy levels which are still there by a direct interaction of the photon with the stored charge.

From this point of view, one can speculate that the difference in the energy of the trap levels obtained with thermal techniques and optical techniques is due to the processes which are involved in the charge detrapping. That is, processes involving secondary forces would yield shallow energy traps, while processes involving primary forces would yield deep energy traps. This assumption would also explain the long-term charge retention observed in the polymeric electrets. The deep traps would give the stability to the charge for a long period of time (even years). Since polymeric electrets are used at low temperatures ($T < T_g$), the polymeric matrix is *quasi-frozen* and the molecular relaxations are slowed.

According to the results obtained for doped COC matrixes, it is possible to say that the trapping sites are located at the chemical impurities. This hypothesis is reinforced due to the following facts: the lack of a TL-glow peak in plain COC matrixes and the coincidence of the deep traps with the absorption spectrum of the dye (sec. 4.2). The shallow traps may indicate a probable interaction between the polymer matrix and the dye.

In case for PETP, the analysis becomes more complex. From thermal-activated processes, dipole orientation plays an important role in charge trapping and detrapping at low temperatures due to the $\beta-$relaxation and a high temperatures due to the $\alpha-$relaxation. The carbonylic group $\rangle C = O$ has been identified as the molecular dipole in the polymer chain. These results may indicate that the charge are located in the $\rangle C = O$ dipoles. On the other hand, the photo-activated processes show that the $\pi - \pi^*$ benzene transitions are responsible for the charge trapping and detrapping. In this case, the results suggest that the charge would be located in the benzene rings.

Since a chemical resonance between the carbonylic groups $\rangle C = O$ and the benzene rings happens, this could mean that an extra charge could be stabilized by this chemical resonance. This assumption would explain the thermoluminescence spectra of the TL-experiments observed in previous works (Padhye and Tamhane, 1978; Takai *et al.*, 1978c). If the charge is stabilized by this chemical resonance, the charge detrapping would be stimulated by both the dipole relaxations together with their coperative motions from the neighboring atoms and the optical transitions from the benzene rings. In this case the trapping site would be located at the chemical resonance of the chemical group $-COO-$benzene$-COO-$.

Chapter 5

Conclusions and Outlook

5.1　Conclusions

Polymeric electrets are complex systems. The charge storage in polymer electrets play an important role for electromechanical-transducer application. Though chemical and physical characteristics of polymers have been identified to affect the dielectric properties of the polymeric electrets, microscopic mechanisms of charge retention are still poorly understood. In this work, the combination of thermal and optical techniques was employed in order to describe the charge trapping and detrapping behavior of a polymeric electret. The information provided from each of these techniques gives a piece of the picture to understand the charge-retention mechanisms. Moreover, this information helps to identify of the probable trapping sites and to explain how the long-term storage happens.

Charge detrapping processes were investigated in order to obtain a trace of the trapping centers in the polymeric electrets. The charge and dipole profiles in the thickness direction were monitored to evidence the charge trapping or detrapping. Unfortunately, the techniques employed present some limitations, e.g. in terms of resolution (2 μm for PPS) and accuracy of the distribution function coming from noisy data for LIMM. Still, useful charge profiles were obtained with the combination of both techniques and with the interpolation of experimental results.

The study was performed on polyethylene terephthalate (PETP) and cyclic olefin copolymer (COC). COC is not an internal photo-electret and does not have a net dipole moment. The electret behavior of COC is then given by the stored charges. This polymer shows a plane dielectric permittivity $\varepsilon' \approx 2.57$. Since COC does not show light absorption at wavelengths larger than 220 nm, charge detrapping could be investigated in the bulk. In order to probe the internal electric field, the COC matrices were doped with dyes such as Pyrene and DANS. The thermally stimulated processes of such systems activate energy traps of about 0.6 and 0.11 eV, in DANS doped films. On the other hand, optically stimulated processes activate an energy trap level of 4 eV, in pyrene doped films. These results indicate that the charge traps are located at the chemical impurities (the dye in this case) or at their interface with the polymer matrix. Thermally activated molecular movements of the COC matrix stimulate the dopant-polymer interface and along with that the charge

detrapping. On the other hand, light irradiation of the sample does not induce molecular movements in the COC matrix, but rather a direct or indirect photon-charge interaction. The photon-charge interaction induces the detrapping of the charge stored at the chemical impurity. This indicates that the observed energy of the charge traps is related to the process of detrapping and the chemical nature of the trapping centers. One could think, that the processes of charge detrapping from shallow traps are associated to the secondary forces, while the processes of charge detrapping from deep traps could be related to the primary forces.

In contrast to COC, PETP is known to be as an internal photo-electret with a dipole moment located at the carbonyl group ($>C = O$). Its electret behavior arises from the dipole orientation and charge storage. Dielectric spectroscopy in combination with other techniques have been widely employed to identify the molecular groups responsible of the dipolar behavior of the electret (McCrum *et al.*, 1991; Menczel *et al.*, 1981). Further information, such as degree of crystallinity, was obtained from the dielectric spectra (sec. 4.1.1). In our case, the samples which were employed showed a degree of crystallinity of approx. 0.55 ± 0.05.

Due to the need of performing PSD experiments under vacuum at low temperatures ($-160\ °C \leqslant T < 25\ °C$), LIMM was employed to determine *in situ* the internal electric field of the sample. In materials such as PETP, where the dipole moment is small, the unique determination of the electric field and the polarization becomes complex. However, it was possible to determine separate charge and dipole profiles together with the electric field and the polarization.

When PETP samples are charged, they exhibit a photocurrent transient response. This photocurrent transient has a maximum (j_p) at approx. 9 s after starting the light irradiation on the sample. The temperature dependence of the j_p is described by the Arrhenius' law and has an activation energy of 0.106 eV (1.698×10^{-20} J). From this result the pair thermalization length (r_c) for the photo-carrier generation in PETP was estimated to be approx. 4.5 nm, using the approximation proposed by Batt *et al.* (1968). This result agrees with the simulations performed using Onsager's law, where distances of 4.6 to 4.7 nm were calculated to obtain a 70% probability for charge generation (sec. 4.3.2). The generated photo-charge carriers can recombine, interact with the trapped charge, escape through the electrodes or occupy an empty trap.

The stored charge generates an internal electric field, which is affected by the molecular dipoles. Thus, to determine the internal electric field using the LIMM technique, the pyroelectric coefficient profile needs to be described. Two approaches were performed in this work in order to describe the internal electric field. The first approach is performed by approximating the pyroelectric coefficient to the quasi-static pyroelectric coefficient (QPC). Since the raw data of the QPC-experiments on PETP samples are noisy, a numerical Fourier-filtering procedure for a single frequency was applied. Simulations show that the data analysis is reliable when the noise level is up to 3 times larger than the calculated current for the QPC. Still, QPCs for unpoled samples were about 0.6 nC/(m^{2}K), while poled samples exhibit QPCs of about 60 nC/(m^{2}K). Furthermore, the charge-dipole interaction was confirmed from these experiments in combination with thermally stimulated discharge or depolarization (TSD).

Quasi-static pyroelectric measurements (QPM) with electric bias were performed to calculate an induced-QPC at different temperatures. The temperature dependance of the induced-QPC resembles that one of the dielectric losses ε''. This indicates that the volume effect is due to the same molecular motions. The induced QPC is approx. 60 nC/(m^{2}K) with an applied electric field of 10 V/µm. If the stored charges generate an electric field of approx. 10 V/µm, the induced QPC is approx. 60 nC/(m^{2}K). This QPC is comparable to that of samples with oriented dipoles. However, if the charge decays, the induced QPC decreases.

The second approach to calculate the internal electric field was performed using LIMM data of samples poled at 110 °C without photo-excitation. PPS measurements showed that the electret behavior of samples poled at the same temperature (110 °C) without irradiation is due to the dipole orientation. According to these data, the distribution profile ($g(z)$ from LIMM) of the sample without irradiation is mainly due to the polarization. If the injected charge is neglected ($E(z) \approx 0$), the distribution function $g(z)$ can be approximated by the pyroelectric coefficient profile $p(z)$. Using these data, the charge profile of samples charged with UV-light irradiation at high temperature (110 °C) could be determined. Then, the internal electric field ($E(z)$) was calculated from this charge distribution. Both approximations describe in good agreement with each other the internal electric field of samples charged and poled at 110 °C.

The calculated charge profile of a sample charged at 110 °C with light irradiation shows a similar shape to that charged at lower temperature (-100 °C). These similar shapes and the temperature dependance of the transient photo-current peaks suggest that the stored charge profile depends on the temperature and may follow the Arrhenius' law. In this sense, the charge profiles at intermediate temperatures were then determined by interpolating the calculated charge profile. The internal electric field due to the stored charges was afterwards calculated from these charge profiles. These profiles demonstrate the charge detrapping.

Optically activated measurements indicate the presence of charge traps at 4.1 eV in PETP. This trap level coincides with the optical absorption derived from the $^1A_{1g} \rightarrow^1 B_{2u}(^1L_b)$ benzene transition. This indicates that the trap level could be related to the benzene rings. The observed charge detrapping selectivity indicates that the charge detrapping via PSD-decay is from a direct photon-charge interaction. Additionally, the charge detrapping can be eased by the photo-exciton generation and the interaction of the photo-excitons with the trapped charge carriers.

Another photo stimulated current peak was observed at 240 nm (5.2 eV). Contrary to the peak at 300 nm, photo-stimulated charge decay was not detectable by light irradiation at this wavelength. This is due to the effect of the penetration length given by the strong light absorption of the sample. Nevertheless, this energy level coincides with the optical absorption derived from $^1A_{1g} \rightarrow ^1B_{2u}(^1L_a)$ benzene transition.

Additionally, at the electrode-polymer interface, the photoemission effect has been identified as one detrapping mechanism. In samples with gaps between electrode and polymer, the external photo-effect plays an important role in the charge detrapping. Internal photo-emission is also present in films with intimate contact with the electrode. In both cases, the photocurrent threshold energy depends on the work function of the electrode material.

On the other hand, our thermally activated measurements indicate the presence of charge traps at approx. 0.36 eV and were related to the motion of ethylenic linkages (β_2-relaxation) of PETP. Moreover, it has been observed that the charge detrapping is also eased by the molecular relaxation (β_1-relaxation). These facts indicate that the charge could be stabilized due to the dipolar groups, here the carbonylic groups $\rangle C = O$, and be released during a molecular relaxation.

Since a chemical resonance happens in PETP chains (sec. 3.3.1), one can speculate that the carbonyl groups and the benzene ring can stabilize and share an extra charge carrier. This charge carrier could be detrapped with both the photo-transitions of benzene and the carbonyl motions. From this point of view, the trapping sites would be located at the chemical resonance of the chemical group $-COO-benzene-COO-$ in the PETP. This assumption agrees with the hypothesis employed to explain the difference of the trap levels observed in the COC samples from thermal and optical techniques.

From these results, it can be said that the charge trapping and detrapping is not limited to one simple process. For that reason, different techniques are needed. The combination of these results lead to a better description of the charge storage mechanisms and trapping sites. Thermal- and optical-measurements yield different trap energy levels. This difference depends strongly on the detrapping process and the chemical nature of the trapping site. That is, secondary forces involves mechanisms which require less energy than the energy required for the mechanisms involved in the primary forces. In consequence, the processes involving secondary forces would yield shallow traps and the processes involving primary forces would yield deep traps. Moreover, the presence of the deep traps explains the stability of the charge for long periods of time.

5.2 Expected future work and open questions

Charge traps can be located in the $-OOC-C_6H_4-COO-$ groups of PETP in a chemical resonance as mentioned before. If that happens, the question which remains is: which chain configuration could stabilize the charge carrier, i.e. *trans*, *cis* or both. Charge/poled and uncharged/unpoled samples should be studied searching for changes in the polymer configuration.

Due to the effect of penetration depth and the presence of the second photocurrent peak in the PSD-spectra at 240 nm, the charge detrapping should be investigated at the surface of the samples. At the metal-polymer interface, the adhesion between a polymer and a metal layer depends on the chemical interactions occurring at the molecular level at the metal-polymer (Calderone *et al.*, 1994). It has yet been to be determined which chemical species are responsible of the charge detrapping at the electrode-polymer interface. The research at the interface can be performed using X-ray photo-electron spectroscopy of charged and uncharged samples coated with different metals.

The end groups are hydroxyl groups ($-OH$) and it was not possible to relate this group to the charge detrapping. These chemical components generate molecular dipoles due to the electro-negativity of the oxygen. Charges could also be stabilized by these chemical groups.

Another circumstance to consider is the possibility that the ethylenic groups could be a trapping center (Partridge, 1965). In order to discern the location of the trapping center at these groups, it is necessary to perform experiments at higher energy levels using vacuum ultra violet (VUV).

Each polymer has a different chemical constitution. Even those having similar constitution, may not have the same conformation. Molecular associations give another dimension of charge trapping and dipole orientation. In the same way, chemical impurities which are present in polymer films can introduce charge carriers, charge traps or dipole moment. Although it might not be possible to determine the universal trapping site in the polymer, a general behavior due to the chemical constitution and conformation can be proposed in future works.

There are polymeric electrets where the charge trapping cannot be suggested from the chemical constitution, but they are known to store charges for long periods of times. Some of these polymers are polytetrafluoroethylene (Fedosov *et al.*, 1987; Oda *et al.*, 1985; Camacho González *et al.*, 2002; Mellinger *et al.*, 2004a), polyethylene (Partridge, 1965; Comins and Wintle, 1972; Ieda *et al.*, 1977) and polypropylene (Ieda *et al.*, 1977). In order to learn more about deep charge traps, higher energy levels using VUV are needed to research such systems.

Another kind of polymeric electrets, which have recently gained more importance, are polymeric systems with macroscopic formations in the polymer matrix, such as voids. Cellular polypropylene is one of these interesting systems presenting a net dipole moment which rises from charges stored on the surface of the voids (Paajanen *et al.*, 2000, 2001). Photo-stimulated detrapping showed three energy trap levels at 4.6, 5.6 and 6.3 eV, which coincide with the absorption spectrum of the films before being voided (Mellinger *et al.*, 2004a). These kinds of systems present a new challenge in the quest for the explanation of long-term charge storage.

Appendix A

Temperature dependence of the photocurrent

The probability $f(r, \theta)$ that an isolated thermalized ion-pair with initial separation r and orientation θ relative to the applied field E will escape geminate recombination is given by (Onsager, 1938)

$$f(r, \theta) = \exp(-A)\exp(-B) \sum_{m=0}^{\infty}\sum_{n=0}^{\infty} \frac{A^m}{m!}\frac{B^{m+n}}{(m+n)!}, \qquad \text{(A.1)}$$

with $A = 2q/r$, $B = \beta r(1 + \cos\theta)$, $q \equiv e^2/(8\pi\varepsilon\varepsilon_0 k_B T)$, $\beta \equiv eE/(2k_B T)$.

By expanding the sums,

$$\sum_{m=0}^{\infty}\sum_{n=0}^{\infty} \frac{A^m}{m!}\frac{B^{m+n}}{(m+n)!} = \sum_{m=0}^{\infty} \frac{A^m}{m!} \sum_{n=0}^{\infty} \frac{B^{m+n}}{(m+n)!} \qquad \text{(A.2)}$$

$$= \sum_{m=0}^{\infty} \frac{A^m}{m!} \left(\frac{B^m}{m!} + \frac{B^{(m+1)}}{(m+1)!} + \frac{B^{(m+2)}}{(m+2)!} + \cdots \right) \qquad \text{(A.3)}$$

$$= 1 + B + AB + \frac{1}{2}B^2 + \frac{1}{2}AB^2 + \frac{1}{6}AB^3 + \frac{1}{4}A^2B^2 + \cdots, \text{(A.4)}$$

and applying the Taylor series to the exponential function

$$\exp(-B) = \sum_{r=0}^{\infty} \frac{(-B)^r}{r!} = 1 - B + \frac{B^2}{2} - \frac{B^3}{6}\cdots, \qquad \text{(A.5)}$$

it is possible to simplify the product to the first order term, in order to obtain as a first approximation:

$$\exp(-B) \sum_{m=0}^{\infty}\sum_{n=0}^{\infty} \frac{A^m}{m!}\frac{B^{m+n}}{(m+n)!} \approx 1 + AB. \qquad \text{(A.6)}$$

Employing the first aproximation given by eqn. (A.6), we obtain a simplified probability function $f(r, \theta)$

$$f(r, \theta) \approx \exp(-\frac{2q}{r})(1 + 2q\beta(1 + \cos\theta)) \approx \exp(-\frac{2q}{r})(1 + 4q\beta) \qquad (A.7)$$

On the other hand, the carrier quantum yield ϕ may be given (Batt *et al.*, 1968) by

$$\phi = \phi_0 \int g(r, \theta) f(r, \theta) dr \qquad (A.8)$$

where ϕ_0 ionization quantum yield and $g(r, \theta)$ the initial distribution of thermalized pair configurations.

Substituting eqn. (A.7) in eqn. (A.8), the quantum yield can be written as

$$\phi = \phi_0 \int g(r, \theta) \exp\left(-\frac{2q}{r}\right)(1 + 4\beta q) dr. \qquad (A.9)$$

For isotropic media $g(r, \theta)$ can be simplified to $g(r, \theta) = 4\pi r^2 g(r) dr$. Then, ϕ is given by:

$$\phi = \phi_0 4\pi(1 + 4\beta q) \int g(r) \exp\left(-\frac{2q}{r}\right) r^2 dr. \qquad (A.10)$$

Considering $g(r)$ a normalized delta function $\frac{\delta(r - r_0)}{4\pi r_0^2}$ and evaluating the integral term, eqn. (A.10) becomes

$$\phi = \phi_0(1 + 4\beta q) \exp\left(-\frac{2q}{r_0}\right). \qquad (A.11)$$

Setting the electric field as a parameter, it is possible to rewrite eqn. (A.11) as

$$B(E, T) = \frac{\phi}{\phi_0} \frac{1}{1 + 4\beta q} = \exp\left(-\frac{2q}{r_0}\right) \qquad (A.12)$$

and obtain a relation of ϕ versus temperature

$$B(E, T) = \exp\left(-\frac{e^2}{4\pi\varepsilon\varepsilon_0 r_0 k_B T}\right). \qquad (A.13)$$

This equation shows that the intrinsic photo-generation depends on the temperature following the Arrhenius law with an activation energy

$$E_A = \frac{e^2}{4\pi\varepsilon_0\varepsilon r_0}. \qquad (A.14)$$

Solving for r_0

$$r_0 = \frac{e^2}{4\pi\varepsilon_0\varepsilon E_A}. \tag{A.15}$$

Evaluating for PETP, the activation energy calculated from the peaks of the photo-current experiments (fig. 4.39) can be used to calculate r_0

$$r_0 \approx 4 \text{ nm}$$

Appendix B

Quasi–static pyroelectric coeffi cient

The pyroelectric effect is said to be the reversible change of the polarization ΔP from a dielectric under the effect of the temperature change.

$$\Delta P = p \cdot \Delta T \ , \tag{B.1}$$

where, p is the pyroelectric coefficient, ΔT is the temperature change. Using the time t as parameter and reducing the time interval, eqn. (B.1) can be written as follows:

$$\frac{d\,P}{dt} = p\frac{d\,T}{dt} \tag{B.2}$$

Assuming that the temperature is of sinusoidal form ($T = T_m \exp\{i(\omega t + \phi_1)\}$), the change of the polarization with respect to the time can be expressed as

$$\frac{d\,P}{dt} = \iota p\omega T_m \exp\{i(\omega t + \phi_1)\} \ , \tag{B.3}$$

where T_m is the amplitude of the temperature oscillation, ω is the angular frequency, ϕ_1 is the shift angle, and ι indicates the imaginary unit.

On the other hand, from Maxwell's equations in a dielectric media the generated current density ($J(t)$) is due to the variation of the displacement density $d\,D/dt$, that is

$$\nabla \times H = J(t) + \frac{\partial\,D}{\partial t} \Rightarrow J(t) = -\frac{\partial\,D}{\partial t}, \tag{B.4}$$

in the absence of a magnetic field.

If the electric field applied is constant, the current density measured is due to the dipolar changes.

$$J(t) = -\frac{\partial\,P}{\partial t} \tag{B.5}$$

The minus sign indicates that the image charges at the electrodes are of opposite sign to the polarization. Since we are not interested on the polarity of the current, the minus sign can be omitted and the equation can be written as follows:

$$J(t) = \frac{\partial\,P}{\partial t} \tag{B.6}$$

The comparison of the eqns. (B.3) and (B.6) indicates that the current is determined by

$$J(t) = \iota p \omega T_m \exp\{i(\omega t + \phi_1)\} \tag{B.7}$$

If the temperature change is of the sinusoidal form. The measured current is also expected to be of sinusoidal form, that is

$$J_m \exp\{i(\omega t + \phi_2)\} = \iota p \omega T_m \exp\{i(\omega t + \phi_1)\} , \tag{B.8}$$

where J_m is the amplitude of the current density, and ϕ_2 is the phase shift of the current signal. Solving for the pyroelectric coefficient

$$p = \frac{J_m}{\omega T_m} \left(\sin(\phi) + \iota \cos(\phi) \right) \tag{B.9}$$

where $\phi = \phi_2 - \phi_1$. Only the real part of the eqn. (B.9) has a physical meaning, so that the pyroelectric coefficient is given by

$$p = \frac{I_m}{A \omega T_m} \sin(\phi) \tag{B.10}$$

where $I_m = A J_m$ and A is the electrode area.

Bibliography

L. E. Amborski, *Structural dependence of the electrical conductivity of polyethylene terephthalate*. J. Polym. Sci. **62**, 331–46 (1962).

ANSI/IEEE Std. 100-1988, *IEEE Standard dictionary of electrical and electronics terms*. Fourth ed., Published by the Institute of Electrical and Electronics Engineers, New York (1988).

F. Auriemma, P. Corradini, G. Guerra and M. Vacatello, *Conformational analysis of highly extended poly(ethylene terephthalate) chains by Monte Carlo calculations*. Macromol. Theory Simul. **4**, 165–76 (1995).

R. H. Batt, C. L. Braun and J. F. Hornig, *Electric-field and temperature dependence of photoconductivity*. J. Chem. Phys. **49**, 1967–8 (1968).

S. Bauer and S. Bauer-Gogonea, *Current practice in space charge and polarization profile measurements using thermal techniques*. IEEE Trans. Diel. Electr. Insul. **10**, 883–902 (2003).

S. Bauer and B. Ploss, *A method for the measurement of the thermal, dielectric, and pyroelectric properties of thin pyroelectric films and their applications*. J. Appl. Phys. **68**, 6361–6367 (1990).

H. Bauser, *Ladungsspeicherung in Elektronenhaftstellen in organischen Isolatoren*. Kunststoffe **62**, 192 (1972).

A. Bergman and J. Jortner, *Photoconductivity of crystalline anthracene induced by tunable dye lasers*. Phys. Rev. B **9**, 4560–74 (1974).

I. B. Berlman, *Handbook of fluorescence spectra of aromatic molecules*. Acad. Pr., New York (1971).

J. Besold, R. Thielsch, C. Frenzel, R. Born and M. Möbius, *Surface and bulk properties of electron evaporated carbon films*. Thin Solid Films **293**, 96–102 (1997).

F. W. Billmeyer, Jr., *Textbook of polymer science*. John Wiley & Sons, New York (1984).

P. Bloss and H. Schäfer, *Investigations of polarization profiles in multilayer systems by using the laser intensity modulation method*. Rev. Sci. Instr. **65**, 1541–50 (1994).

P. Bloss, M. Steffen, H. Schäfer, G. M. Yang and G. M. Sessler, *A comparison of space charge distributions in electron-beam irradiated FEP obatained by using heat-wave and pressure-wave techniques*. J. Phys. D: Appl. Phys. **30**, 1668–75 (1997).

J. D. Brodribb, D. M. Hughes and D. O'Colmain, *The theory of photon-stimulated current spectroscopy*. J. Phys. D: Appl. Phys. **8**, 856–62 (1975).

D. Broemme, R. Gerhard-Multhaupt and G. M. Sessler, *Isothermal and thermally stimulated discharge of polyethylene terephthalate foils*. In: *Annual Report, Conference on Electrical Insulation and Dielectric Phenomena*, pp. 129–35, IEEE Electrical insulation society, IEEE Service center, Piscataway, New Jersey, USA (1981).

A. Calderone, R. Lazzaroni, J. L. Brédas, Q. T. Le and J. J. Pireaux, *A joint theoritical and experimental study of the aluminum/polyethylene terephthalate interface*. Synth. Met. **67**, 97–101 (1994).

F. Camacho González, *Photo-stimulated discharge of polymeric electrets*. Master's thesis, Deparment of Physics of the University of Potsdam, Potsdam, Brandenburg, Germany (2002).

F. Camacho González, A. Mellinger and R. Gerhard-Multhaupt, *Energy levels of charge tranps in polyethylene terephthalate films*. In: Teysedre (ed.), *ICSD2004*, pp. 123–123, IEEE, Toulouse, France (2004).

F. Camacho González, A. Mellinger, R. Gerhard-Multhaupt, L. F. Santos and R. M. Faria, *Photo-stimulated discharge of highly insulating polymers (PTFE and PETP)*. In: *2002 Annual Report Conference on Electrical Insulation and Dielectric Phenomena*, Cancun, Mexico (2002).

F. Camacho González, A. Mellinger, R. Gerhard-Multhaupt, Z. Szamel, I. Głowacki and J. Ulański, *Thermoluminescence of poled polyethylene terephthalate films*. In: J. A. Giacometti, O. N. Olveira Jr. and R. M. Faria (eds.), *12^{t}h International Symposium on Electrets*, pp. 288–291, IEEE Service Center, Piscataway, NJ, Salvador, Bahia-Brazil (2005).

J. C. Coburn and R. H. Boyd, *Dielectric relaxation in poly(ethylene terephthalate)*. Macromolecules **19**, 2238–45 (1986).

R. E. Collins, *Analysis of spatial distribution of charges and dipoles in electrets by a transient heating technique*. J. Appl. Phys. **47**, 4804–4808 (1976).

—, *Practical application of the thermal pulsing technique to the study of electrets*. J. Appl. Phys. **51**, 2973–2986 (1980).

J. D. Comins and H. J. Wintle, *Photoelectric effects in poly(ethylene terephthalate) and and polyethylene*. J. Polym. Sci.: Polym. Phys. Edi. **10**, 2259–80 (1972).

R. A. Creswell and M. M. Perlman, *Thermal currents from corona charged Mylar*. J. Appl. Phys. **41**, 2365–75 (1970).

D. K. Das–Gupta, *Molecular processes in polymer electrets*. J. Electrostat. **51-52**, 159–66 (2001).

R. P. Daubeny, C. W. Bunn and C. J. Brown, *The crystal structure of polyethylene terephthalate*. Proc. R. Soc. London, Ser. A **226**, 531 (1954).

P. Debye, *Polar Molecules*. Dover publications, New York (1945).

L. A. Dissado and J. C. Fothergill, *Electrical degradation and Breakdown in Polymers*. Peter Peregrinus Ltd., London (1992).

L. A. Dissado, G. Mazantti and G. C. Montanari, *The role of trapped space charges in the electrical aging of insulating materials*. IEEE Trans. Diel. Electr. Insul. **4**, 496–506 (1997).

E. Dobruchowska, L. Okrasa, I. Głowacki, J. Ulański and G. Boiteux, *The 'wet dog' effect in polymers as seen by thermoluminescence*. Polymer **45**, 6027–6035 (2004).

M. Doi and S. F. Edwards, *The theory of polymer dynamics*. Clarendon Press, Oxford (1988).

Du Pont Teijin, *Mylar*. Tech. rep., Du Pont de Nemours GmbH, Bad Homburg v.d.H., Germany (2000).

M. Eguchi, *On dielectric polarisation*. Proc. Phys. Math. Soc. Jpn., Series 3 pp. 326–31 (1919).

T. Ehara, H. Hirose, H. Kobayashi and M. Kotani, *Molecular alignment in organic thin films*. Synthetic Metals **109**, 43–6 (2000).

R. Emmerich, S. Bauer and B. Ploss, *Temperature distribution in a film heated with a laser spot: Theory and measurement*. Appl. Phys. A **54**, 334–9 (1992).

M. Faraday, *Experimental researches in electricity*. Richard and John Edward Taylor, London (1839).

S. N. Fedosov, A. E. Sergeeva and M. M. Motylinskaya, *Transient photocurrents accompanying irradiation of charged films of polytetrafluoroethylene*. Izvestiya Vysshikh Uchebnykh Zavedenii, Fizika pp. 734–737 (1987).

J. Fourny, M. Schott and G. Delacôte, *Singlet-triplet interactions in crystalline anthracene*. Phys. Rev. Lett. **21**, 1085–8 (1968).

R. H. Fowler, *The analysis of photoelectric sensitivity curves for clean metals at various temperatures*. Phys. Rev. **38**, 45–56 (1931).

H. Fröhlich, *Theory of dielectric. Dielectric constant and dielectric loss*. Oxford science publications, Oxford (1958).

P. Frübing, W. Neumann and H. Hänsel, *Thermisch stimulierte Depolarisationsströme in Polyethylenterephthalat nach Anregung mit UV–Licht*. Acta Polym. **31**, 767–70 (1980).

C. F. Gallo, *Corona– a brief status report*. IEEE Trans. Industry Applications **6**, 550–7 (1975).

A. Gemant, *Electrets*. Philos. Mag. p. 929 (1935).

R. Gerhard-Multhaupt, M. Haardt, W. Eisenmenger and G. M. Sessler, *Electric-field profiles in electron-beam-charged polymer electrets*. J. Phys. D **16**, 2247–2256 (1983).

R. Gerhard-Multhaupt, W. Künstler, G. Eberle, W. Eisenmenger and G. Yang, *High space-charge densities in the bulk of fluoropolymer electrets detected with piezoelectrically generated pressure steps*. In: J. C. Fothergill and L. A. Dissado (eds.), *Space Charge in Solid Dielectrics*, pp. 123–132, The Dielectrics Society (1997).

J. A. Giacometti and O. N. de Oliveira Jr., *Corona charging of polymers*. IEEE Trans. Electr. Insul. **27**, 924–43 (1992).

H. W. Gibson, *Linear free energy relationships. V. Triboelectric charging of organic solids*. J. Am. Chem. Soc. **97**, 3832–3 (1975).

H. W. Gibson and F. C. Bailey, *Linear free energy relationships. Triboelectric charging of poly(olefins)*. Chem. Phys. Lett. **51**, 352–5 (1977).

H. W. Gibson, F. C. Bailey, J. L. Mincer and W. H. H. Gunther, *Chemical modification of polymers. XII. Control of triboelectric charging properties of polymers by chemical modification*. J. Polym. Sci.: Polym. Chem. Ed. **17**, 2961–74 (1979).

S. Gray, *A letter from Mr. Stephen to Dr. Mortimer, Secr. R. S., containing a farther account of his experiments concerning electricity*. Phil. Trans. R. Soc. London, Ser. A pp. 285–91 (1732).

B. Gross, *Radiation-induced charge storage and polarization effects*. In: G. M. Sessler (ed.), *Electrets*, vol. 1, pp. 216–284, Laplacian Press (1999).

S. Havriliak and S. Negami, *A complex plane analysis of α-dispersion in some polymer systems*. J. Polym. Sci.: Part C **14**, 99–117 (1966).

K. Hayashi, K. Yoshino and Y. Inuishi, *Temperature dependence of carrier mobility in polyethylene terephthalate*. Jap. J. Appl. Phys. **12**, 1089–90 (1973).

O. Heaviside, *Electromagnetic induction and its propagation. Electrization and electrification. Natural electretets*. The Electrician pp. 230–1 (1885).

—, *Electromagnetic induction and its propagation. Electrization and electrification. Natural electrets*. In: O. Heaviside (ed.), *Electrical papers*, vol. 1, pp. 488–93, Chelsea, New York (1892).

J. Hesse, *Charges and dipoles in polyethylene terephthalate: pyro- and piezoelectrical and TSD investigations*. Diploma Thesis, Department of Physics of the University of Potsdam, Potsdam, Germany (1999).

J. R. Holum, *Organic and biological chemistry*. John Wiley & sons, Inc. (1996).

M. Ieda, Y. Takai and T. Mizutani, *Photoconduction processes in polymeres*. Memoirs of the Faculty of Engineering, Nagoya University **29**, 1–59 (1977).

K. H. Illers and H. Breuer, *Molecular motions in polyethylene terephthalate*. J. Colloid. Sci. **18**, 1–31 (1963).

Y. Ishida, K. Yamafuji, H. Ito and M. Takayanagi, *Effects of degree of crystallinity upon dielectric behaviors in some aromatic polyesters*. Kolloid. Z. **184**, 97–108 (1962).

D. Ito and T. Nakakita, *Thermally stimulated current and thermoluminescence due to electron detrapping by local molecular motions in polyethylene terephthalate*. J. Appl. Phys. **51**, 3273–3277 (1980).

A. Kaito, K. Nakayama and H. Kanetsuna, *Polarized reflection spectrum and molecular–orientation in uniaxially drawn poly(ethylene-terephthalate)*. J. Polym. Sci., Part B: Polym. Phys. **26**, 1439–55 (1988).

W. Kaminsky, *New polyolefins by metallocene catalysts*. Pure Appl. Chem. **70**, 1229–1233 (1998).

K. C. Kao and W. Hwang, *Electrical transport in solids. With a particular reference to organic semiconductors*. Pergamon Press (1981).

V. Kestelman, L. Pinchuk and V. Goldade, *Electrets in engineering. Fundamental applications*. Kluwer academic publishers, Norwell, Massachusetts (2000).

K. Kojima, A. Maeda, Y. Takai and M. Ieda, *Thermally stimulated currents from polyethylene terephthalate due to injected charges*. Jap. J. Appl. Phys. **17**, 1735–38 (1978).

F. Kremer, *Dielectric spectroscopy – yesterday, today and tomorrow*. J. of Non-Crys. Solids **305**, 1–9 (2002).

C. C. Ku and R. Leipins, *Electrical properties of polymers: chemical principles*. Hanser Publisher, Munich, Vienna, New York (1987).

J. P. LaFemina and G. Arjavalingam, *Photophysics of poly(ethylene terephthalate): Ultraviolet absorption and emission*. J. Phys. Chem. **95**, 984–988 (1991).

S. B. Lang, *Laser intensity modulation method (LIMM): experimental techniques, theory and solution of the integral equation*. Ferroelectrics **118**, 343–61 (1991).

—, *Two–dimensional thermal analysis of thin–film pyroelectric infrared detectors*. Ferroelectrics **258**, 297–302 (2001).

—, *Laser intensity modulation method (LIMM): Review of the fundamentals and new method for data analysis*. IEEE Trans. Diel. Electr. Insul. **11**, 3–12 (2004).

S. B. Lang and D. K. Das-Gupta, *A technique for determining the polarization distribution in thin polymer electrets using periodic heating*. Ferroelectrics **39**, 1249–1252 (1981).

S. Lazare, J. C. Soulignac and P. Fragnaud, *Direct and accurate measurement of etch rate of polymer-films under far-UV irradiation*. Appl. Phys. Lett. **50**, 624–5 (1987).

A. C. Lilly, Jr and R. McDowell, *High-field conduction in films of mylar and teflon*. J. Appl. Phys. **39**, 141–7 (1968).

L. M. Loew and E. Sacher, *Use of the molecular orbital theory potential energy surfaces in determining polymer conformations I. Poly(ethylene terephthalate)*. J. Macromol. Sci., B: Phys. **15**, 619 (1978).

T. Maeno, T. Futami, H. Kushibe, T. Takada and C. M. Cooke, *Measurement of spatial charge distribution in thick dielectrics using the pulsed electroacustic method*. IEEE Trans. Diel. Electr. Insul. **23**, 433–439 (1988).

E. H. Martin and J. Hirsch, *Electron-induced conduction in plastics. I. Determination of carrier mobility*. J. Appl. Phys. **43**, 1001–7 (1972).

N. G. McCrum, B. E. Read and G. Williams, *Anelastic and dielectric effects in polymeric solids*. Dover Publications, New York (1991).

S. W. S. McKeever, *Thermoluminescence of solids*. Cambridge Univ. Pr., Cambridge, U.K. (1988).

S. W. S. McKeever and D. M. Hughes, *Thermally stimulated currents in dielectrics*. J. Phys. D: Appl. Phys. **8**, 1520–1529 (1975).

A. Mellinger, *Charge storage in electret polymers: Mechanisms, characterization and application*. Habil. Report. Department of Physics of University of Potsdam, Potsdam, Brandenburg, Germany (2004a).

—, *Unbiased iterative reconstruction of polarization and space–charge profiles from thermal–wave experiments*. Meas. Sci. Technol. **15**, 1347–1353 (2004b).

A. Mellinger, F. Camacho González and R. Gerhard-Multhaupt, *Iterative Solution of the LIMM Equation and its application to the measurements of polarization and space charge distribuitions under UV–irradiation*. In: *4th Asian Meeting on Ferroelectrics*, Bangalore, India (2003).

—, *Photostimulated discharge in electret polymers: an alternative approach for investigating deep traps*. IEEE Trans. Diel. Electr. Insul. **11**, 218–26 (2004a).

A. Mellinger, F. Camacho González, R. Gerhard-Multhaupt, L. F. Santos and R. M. Faria, *Photo-stimulated discharge of corona and electron-beam charged polymers*. In: *$11^{t}h$ International Symposium on Electrets*, Melbourne, Australia (2002).

A. Mellinger, R. Singh, F. Camacho González, Z. Szamel and I. Głowacki, *In situ observation of optically and thermally induced charge depletion in chromophore-doped cyclic olefin copolymers*. In: *Annual Report, Conference on Electrical Insulation and Dielectric Phenomena (CEIDP)*, pp. 142–6, IEEE Service Center, Piscataway, NJ, USA (2004b).

A. Mellinger, R. Singh and R. Gerhard-Multhaupt, *Fast thermal-pulse measurements of space-charge distributions in electret polymers*. Rev. Sci. Instr. **76**, 013903 (2005).

K. P. Menard, *Dynamic mechanical analysis. A practical introduction*. CRC Press LLC, Boca Raton, Florida, USA (1999).

J. D. Menczel, M. Jaffe and W. E. Bessey, *Films*. In: E. A. Turi (ed.), *Thermal characterization of Polymeric materials. Second edition*, pp. 1955–2090, Academic Press (1981).

—, *Films*. In: E. A. Turi (ed.), *Thermal characterization of polymeric materials*, vol. 2, pp. 1955–2089, Academic Press (1997).

M. Meunier and N. Quirke, *Molecular modeling of electron trapping in polymer insulators*. J. chem. phys. **113**, 369–76 (2000).

M. Meunier, N. Quirke and A. Aslanides, *Molecular modeling of electron trapping in polymer insulators: Chemical defects and impurities*. J. chem. phys. **115**, 2876–81 (2001).

E. Nasser, *Fundamentals of gaseous ionization and plasma electronics*. Wiley Interscience, New York (1971).

S. Nespurek, V. Cimrová, J. Pfleger and I. Kmínek, *Free charge carrier formation in polymers under illumination*. Poly. for Adv. Tech. **7**, 459–70 (1996).

T. Oda, T. Utsumi, T. Kumano and M. Itami, *Observation of photo-stimulated detrapping currents of FEP teflon electrets*. In: G. M. Sessler and R. Gerhard-Multhaupt (eds.), *5th International symposium on electrets (ISE 5)*, pp. 288–293, IEEE Electrical insulation society, Castle of Heidelberg, Germany (1985).

L. Onsager, *Initial recombination of ions*. Phys. Rev. **54**, 554–7 (1938).

I. Ouchi, *Anisotropic absorption and reflection spectra of poly(ethylene terephthalate) films in ultraviolet region*. Polym. J. **15**, 225–43 (1983).

I. Ouchi, R. Miyamura, M. Sakaguchi, S. Hosaka and M. Kitagawa, *Excitation and emission spectra of polyethylene terephthalate and polyethylene 2,6–naphthalate films*. Polym. Adv. Technol. **1**, 195–8 (1999).

M. Paajanen, H. Välimäki and J. Lekkala, *Modelling the electromechanical film (EMFi)*. J. Electrostat. **48**, 193–204 (2000).

M. Paajanen, M. Wegener and R. Gerhard-Multhaupt, *Understanding the role of the gas in the voids during corona chargig of cellular electret films – a way to enhance their piezoelectricity*. J. Phys. D: Appl. Phys. **34**, 2482–2488 (2001).

M. R. Padhye and P. S. Tamhane, *Thermoluminescence of polyethylene terephthalate films*. Angew. Makromol. Chem. **67**, 78–89 (1978).

R. H. Partridge, *Electron traps in polyethylene*. J. Polym. Sci. part A: General Papers **3**, 2817–25 (1965).

—, *Near-ultraviolet absorption spectrum of polyethylene*. J. Chem. Phys. **45**, 1679–84 (1966).

B. Ploss, S. Bauer and C. Bon, *Measurement of thermal diffusivity of thin films with bolometers and with pyroelectric temperature sensors*. Ferroelectrics **118**, 435–50 (1991).

B. Ploss, R. Emmerich and S. Bauer, *Thermal wave probing of pyroelectric distributions in the surface region of ferroelectric materials: A new method for the analysis*. J. Appl. Phys. **72**, 5363–5370 (1992).

M. Pope and C. E. Swenberg, *Electronic processes in organic crystals and polymers*. Oxford University Press, New York (1999).

W. H. Press, S. A. Teukolsky, W. T. Vetterling and B. P. Flannery, *Numerical recipes in C*. Cambridge University Press, Cambridge (1992).

W. Reddish, *The dielectric properties of polyethylene terephthalate (terylene)*. Trans. Faraday Soc. **46**, 459 (1950).

—, *Chemical structure and dielectric properties of high polymers*. Pure Appl. Chem. **5**, 723–42 (1962).

T. Rische, A. J. Waddon, L. C. Dickinson and W. J. MacKnight, *Microstructure and morphology of cycloolefin copolymers*. Macromolecules **31**, 1871–4 (1998).

A. Rose, *Space-charge-limited currents in solids*. Phys. Rev. **97**, 1538–44 (1955).

E. Sachez, *Fine structure in the dielectric $\beta-$relaxation of polyethylene terephthalate*. J. Polym. Sci. Part A-2 **6**, 1935–7 (1968).

S. Sapieha and H. J. Wintle, *Photoinjection into polyethylene terephthalate*. Can. J. Phys. **55**, 646–53 (1977).

W. A. Schneider, J. H. Wendorff and R. Gerhard-Multhaupt, *Physical mechanisms for the electret behavior of PETP*. In: *Annual Report, Conference on Electrical Insulation and Dielectric Phenomena*, pp. 441–6, IEEE Electrical insulation society, IEEE Service center, Piscataway, New Jersey, USA (1983).

D. A. Seanor, *Electrical conduction in polymers*. In: D. A. Seanor (ed.), *Electrical properties of polymers*, pp. 1–58, Academic Press. (1982).

G. Sessler, *Physical principles of electrets*. In: G. M. Sessler (ed.), *Electrets*, vol. 1, pp. 13–80, Laplacian Press (1999a).

G. M. Sessler, *Polymeric electrets*. In: D. Seanor (ed.), *Electrical properties of polymers*, pp. 241–284, Academic Press. (1982).

—, *Introduction*. In: G. M. Sessler (ed.), *Electrets*, vol. 1, pp. 1–12, Laplacian Press (1999b).

—, *Physical principles of electrets*. In: G. M. Sessler (ed.), *Electrets*, vol. 1, pp. 13–80, Laplacian Press (1999c).

G. M. Sessler and R. Gerhard-Multhaupt, *Electrets*, vol. 1 and 2. Laplacian Press (1999).

G. M. Sessler, J. E. West and R. Gerhard-Multhaupt, *Measurement of charge distribution in polymer electrets by a new pressure-pulse method*. Polym. Bull. pp. 109–11 (1981).

G. M. Sessler, G. M. Yang and W. Hatke, *Electret properties of cycloolefin copolymers*. In: *Annual Report, Conference on Electrical Insulation and Dielectric Phenomena*, pp. 467–70, Mineapolis, USA (1997).

G. Strobl, *The Physics of polymers*. Springer-Verlag, Germany (1997).

Y. Takai, T. Mizutani and M. Ieda, *Photoluminescence study in polymers*. Jap. J. Appl. Phys. **17**, 651–8 (1978a).

Y. Takai, T. Mizutani, M. Ieda and T. Osawa, *Carrier generation in photoconduction in polymers*. Elect. Eng. in Jap. **96**, 19–25 (1976).

Y. Takai, K. Mori, T. Mizutani and M. Ieda, *Study on electron traps in polyethylene terephthalate by thermally stimulated current and photo-stimulated detrapping current analyses*. Jap. J. Appl. Phys. **16**, 1937–40 (1977a).

—, *Field quenching of thermoluminescence from photoexcited polyethylene terephthalate PET*. J. Phys. D: Appl. Phys. **11**, 991–7 (1978b).

—, *Thermoluminescence from photoexcited polyethylene terephthalate*. J. Polym. Sci. Polym. Phys. Ed. **16**, 1861–8 (1978c).

Y. Takai, T. Osawa, K. C. Kao, T. Mizutani and M. Ieda, *Effects of electrode materials on photocurrents in polyethylene terephthalate*. Jap. J. Appl. Phys. **14**, 473–79 (1975).

Y. Takai, T. Osawa, T. Mizutani and M. Ieda, *Photoconduction in poly(ethylene terephthalate). I. Mechanisms of carrier generation*. J. of Polym. Sci.: Polym. Phys. Ed. **15**, 945–54 (1977b).

—, *Photoconduction in polyethylene terephthalate. Mechanisms of photo-carrier-transport*. Jap. J. Appl. Phys. **16**, 1933–36 (1977c).

G. Teyssedre, C. Laurent, A. Aslanides, N. Quirk, L. A. Dissado, G. C. Montanari, A. Campus and L. Martinotto, *Deep trapping centers in crosslinked polyethylene investigated by molecular modelling and luminescence techniques*. IEEE Trans. on Diel. Electr. Insul. **8**, 744–752 (2001).

G. Teyssèdre, J. Menegotto and C. Laurent, *Temperature dependence of photoluminescence in polyethylene terephthalate films*. Polymer **42**, 8207–16 (2001).

A. Thielen, J. Cerfontaine, J. Niezette, G. Feyder and J. Vanderschueren, *Characterization of polyester films used in capacitors. II. Effects of heat treatments on transient and steady–state charging currents in polyethylene terephthalate thin films*. J. Appl. Phys. **76**, 4696–704 (1994).

A. Thielen, J. Niezette, G. Feyder and J. Vanderschueren, *Thermally stimulated current study of space charge formation and contact effects in metal–polyethylene terephthalate film– metal systems. I. Generalities and theoritical model*. J. Phys. Chem. Solids **57**, 1567–80 (1996a).

—, *Thermally stimulated current study of space charge formation and contact effects in metal–polyethylene terephthalate film– metal systems. II. Influence of polarization conditions*. J. Phys. Chem. Solids **57**, 1581–91 (1996b).

A. Thielen, J. Niezette, J. Vanderschueren, G. Feyder, Q. T. Le and R. Caudano, *Thermally stimulated current study of space–charge formation and contact effects in metal– polyethylene terephthalate films–metal systems. III. Influence of heat treatments*. J. Phys. Chem. Solids **58**, 607–22 (1997).

A. N. Tikhonov, A. V. Goncharskii, V. V. Stepanov and I. V. Kochikov, *Ill–posed image processing problems*. Sov. Phys.–Dokl. **32**, 456–8 (1987).

P. H. van Cittert, *Zum Einfluß der Spaltbreite auf die Intensitätsverteilung in Spektrallinien. II*. Z. Phys. **65**, 298–308 (1931).

J. van Turnhout, *Thermally stimulated discharge of electrets*. In: G. M. Sessler (ed.), *Electrets*, vol. 1, pp. 81–215, Laplacian Press (1999).

H. von Seggern, *Detection of surface and bulk traps*. J. Appl. Phys. pp. 4086–9 (1981).

J. Weese, *A reliable and fast method for solution of Fredholm integral equations of the first kind based on the Tikhonov regularization*. Comput. Phys. Commun. **69**, 99–111 (1992).

J. E. West, H. von Seggern, G. M. Sessler and R. Gerhard-Multhaupt, *The laser-induced-pressure-pulse method: A direct method of measuring charge distribuitons in thin dielectric films*. In: *Conference Record, IEEE Industry Applications Society, Annual Meeting*, pp. 1159–61, IEEE Industry Applications, IEEE Service center, Piscataway, New Jersey, USA (1982).

D. H. Williams and I. Fleming, *Spectroscopic methods in organic chemestry*. McGraw Hill, London, U. K. (1995).

R. Williams, *Física de aislantes*. Trillas, México (1974).

H. J. Wintle and S. Sapieha, *Anomalous photodepolarisation in plastic insulators*. J. Electrostat. **3**, 195–202 (1977).

Publications:

F. Camacho González, A. Mellinger, R. Gerhard-Multhaupt, L. F. Santos and R. M. Faria, Photo-stimulated discharge of highly insulating polymers (PTFE and PETP), IEEE-CEIDP 2002, Cancún, México, 2002

A. Mellinger, F. Camacho González, R. Gerhard-Multhaupt, L. F. Santos and R. M. Faria, Photo-stimulated discharge of corona and electron-beam charged electret Polymers, ISE **11**, Melbourne, Australia, 2002

A. Mellinger, F. Camacho González and R. Gerhard-Multhaupt, Ultraviolet-induced discharge currents and reduction of the piezoelectric coefficient in cellular polypropylene films, *Applied Physics Letters*, **82** (2): $254-256$, 2003

A. Mellinger, F. Camacho González and R. Gerhard-Multhaupt, Photostimulated discharge in electret polymers: an alternative approach for investigating deep traps, *IEEE Transactions on Dielectrics and Electrical Insulation*, **11** (2): $218-226$, 2004

F. Camacho González, A. Mellinger and R. Gerhard-Multhaupt, Energy levels of charge traps in polyethylene terephthalate films, IEEE-ISCD 2004, Toulouse, France, 2004

A. Mellinger, R. Singh, F. Camacho González, Z. Szamel and I. Głowacki, *In situ* observation of optically and thermal induced charge depletion in chromophore-doped cyclic olefin copolymers, IEEE-CEIDP 2004, Boulder, Colorado, USA, 2004

F. Camacho González, A. Mellinger, R. Gerhard-Multhaupt, Z. Szamel, I. Głowacki and J. Ulański, Thermoluminescence of poled polyethylene terephthalate films, IEEE-ISE 12, Salvador, Bahia, Brazil, 2005